OBSERVATIONS ON $MsTh_2$ USING A DOUBLE β-RAY SPECTROMETER.

A

THESIS

submitted by

C. GRAHAM CAMPBELL, M.A., B.Sc.,

for the degree of

DOCTOR OF PHILOSOPHY.

University of Edinburgh.

November 1952.

CONTENTS.

Introduction.

The technique of using a double β-ray spectrometer for the study of the modes of disintegration of β-active bodies, which also emit γ-rays, was proposed, in the first place, by Feather[1]. As its name implies, a double β-ray spectrometer consists essentially of two conventional spectrometers each of which is capable of focusing, independently, electrons of a wide range of momenta which are emitted by a single source centrally situated to be common to both instruments. Application of the technique of coincidence counting to the two β-particle detectors of the double spectrometer therefore enables a detailed study to be made of time correlations between either particles and quanta, or between quanta of different energies, emitted by an unstable nucleus. Selection of a particular γ-radiation is achieved by focusing an internal conversion electron "line" belonging to the γ-radiation on to one β-detector; this then leaves the β-detector of the other half of the spectrometer free to accept either β-particles of the continuous spectrum, of any desired momentum within the range of focus of the instrument, or to accept the internal conversion electrons of a line caused by the emission of a second γ-radiation. Thus both β-γ and γ-γ coincidences may be studied. Study

of β-γ coincidences leads to the determination of the so-called "partial" β -particle spectra of an unstable nucleus*, and therefore to the energies of those excited states of the daughter nucleus which involve directly the β -decay of the parent body. Study of γ-γ coincidences is of further assistance in the determination of disintegration schemes, since those γ -radiations which are emitted in cascade will produce coincidence counts whereas competitive γ -radiations will not*.

A double β -ray spectrometer is therefore capable of providing detailed information regarding the modes of disintegration of β -active bodies possessing complex spectra. Certain essential features however exist which the instrument must possess before it becomes of practical use. It is essential that the solid angles for collection of the electrons by both halves of the spectrometer should be large, otherwise the time taken for coincidence counting to achieve the necessary standard of statistical accuracy will be impracticably long. In this connection it is equally important that the resolving time of the coincidence set should be as short as possible.

---

* It is essential that the γ -radiations involved originate from an excited state of the daughter body which has a half-life for γ emission which is not greater than the resolving time of the coincidence set.

The first experiments made with an instrument of this type were completed in 1948, by Feather, Kyles, and Pringle[2] on the active deposit of thorium. A double semi-circular focusing spectrometer was used with Geiger counters as the β-particle detectors. A coincidence set having a resolving time $\sim 2.5 \times 10^{-7}$ sec. was employed. Due to the statistical time-lag between the entry of the ionizing particle and the appearance of the voltage pulse across a Geiger counter, attempts to reduce the resolving time below $\sim 5 \times 10^{-7}$ sec. result in the loss of genuine coincidences, unless specially designed electronic equipment is used to detect the voltage pulse at the instant of its initiation.

After the completion of the investigation of thorium active deposit, the writer joined the group engaged on work with the double spectrometer, and a few months later Dr. Pringle left the group.

It is well known that a semi-circular focusing β-ray spectrometer does not possess a large solid angle for collection of electrons. The success of the work with thorium active deposit was due to the particularly high intensity of the F line of ThB $\rightarrow$ C. To avoid excessively long counting periods in less favourable cases, either an increase in the solid angle of the spectrometers or a reduction in the resolving time of the coincidence set was necessary. Little improvement

was expected in solid angle without a major redesign of the spectrometer butareduction of the resolving time by a factor of ~25 was feasible.

In this connection, attention was given to the replacement of the Geiger counters by scintillation counters.

An integrated pulse possessing a rise time $\sim 10^{-8}$ sec. is produced at the anode of a multi-stage photo-electron multiplier by the incidence of a rapid series of light quanta on the photo-cathode, due to the passage of an electron through an organic phosphor. Scintillation counters may therefore be used with a coincidence set having a resolving time of $\sim 10^{-8}$ sec., without loss of genuine coincidences. In addition to the pulses due to the β-particles, noise pulses are produced by the scintillation counters, and in consequence rather elaborate electronic circuits are necessary to discriminate against coincidences produced by noise pulses, and at the same time to preserve the fast leading edge possessed by pulses at the anode of the multipliers. Moreover, in addition to recording the coincidence counting rate, it is essential that the coincidence set should provide the β-particle counting rate appropriate to each input channel of the set, to make possible the assessment of the number of accidental coincidences included in the total number of coincidences

recorded.

These requirements were reported to the Electronics Division of the A.E.R.E. at Harwell, and in January 1951 an early model of a high speed coincidence set, possessing a resolving time $\sim 10^{-8}$ sec. was delivered.

Whilst this high speed coincidence set was being developed at Harwell, an investigation of the design of the semi-circular focusing spectrometer was made to ensure that the geometry of the instrument gave the largest solid angle possible without serious loss in resolution. Preliminary experiments with scintillation counters were also made, and the necessary modifications to the spectrometer were carried out to accommodate the new detectors.

In addition to the improvement in the resolving time, scintillation counters possess a second important advantage in that they may be operated as proportional γ-counters, when connected to differential pulse height analyzing circuits. Although such circuits were not incorporated in the coincidence set, only those γ-rays possessing energies above a certain minimum value could be selected. Thus the γ-radiations were to some extent, resolved. Used in this way the solid angle for counting the γ-radiation was made many times greater than for the solid angle subtended by

the counter window when set on an internal conversion electron line. Moreover, especially with energetic γ -radiations, the number of γ -quanta leaving the atom is usually much greater than the number of electrons arising from the internal convertion of γ quanta in a particular shell of the atom. The efficiency of scintillation counters for the detection of γ -radiations is on the other hand only a few percent, whereas all but the low energy β -particles, which arise from internal conversion, may be detected with 100% efficiency. Even with this limitation, the observation of coincidences between γ -radiations counted directly from the source, with very limited resolution, and β -particles of the continuous spectrum proved to be most valuable in the determination of partial β -ray spectra. The method moreover has an added advantage in that for coincidence studies, the range of β -particle momenta which may be focused by one half of the spectrometer is no longer dependent on the energy of the γ -radiation.

A return was therefore made to a technique similar to that of Bothe and Maier-Leibnitz[3], who in 1937 studied coincidences between γ -rays recorded directly from the source with a Geiger counter and the β -particles dispersed by a fixed radius semi-circular focusing spectrometer, but now with the great advantage offered by a limited degree of resolution for the γ -

radiations.

The apparatus in this form was used to investigate the modes of disintegration of $MsTh_2$.

A detailed magnetic analysis of the β -particle spectrum of this body had not been made since the investigations by Black[4] (1924) using a semi-circular focusing photographic spectrograph, and by Yovanovitch and d'Espine[5] (1927) using the direct deviation method. These measurements established the presence of a large number of γ -radiations, some of which were strongly internally converted.

Cloud chamber studies by Lecoin, Perey, and Teillac[6] (1949) and Lecoin, Perey and Riou[7] (1949) shewed that 1.1 secondary electrons were emitted per disintegration. There was, moreover, evidence of a time delay[6] between the emission of a primary β -particle and a conversion electron of less than 60 keV energy. The estimated half-life of the delayed emission was greater than 0.01 sec. Measurements of the maximum energy of the primary β -particle spectrum, made by Yovanovitch and d'Espine[5] (1927) by direct deviation, by Lecoin [8, 9] (1935 and 1938) with a cloud chamber, by Lee and Libby[10] (1939) with a screen cathode spectrometer, and by Feather[11,12] (1930, 1938) using absorption methods gave values of 1.59, 1.63, 1.6, 1.55 $\pm$ 0.07, 2.05, 2.04 MeV respectively.

In the following chapters a study of the spectrometer is made, and the results of the new investigation of the disintegration modes of $MsTh_2$, employing, to a large extent, coincidence techniques are presented. A possible energy level scheme for the daughter radiothorium nucleus is suggested.

CHAPTER 1.

The Double β-ray Spectrometer.

§1. Description of the Spectrometer.

The features of the spectrometer are illustrated by Figure 1.1. The vacuum box, which is evacuated to a pressure of 10^{-4} mm. Hg. by a two-stage oil diffusion pump, is constructed of brass, lined internally with aluminium, and is locked in position in the 5.5 cm. gap between the poles of a large permanent magnet, described in Chapter 4. The lines of force of the magnetic field are perpendicular to the plane of the diagram.

Into a port-hole, of square cross-section, situated centrally in the top edge of the box, the aluminium frame, F, fits. Grooves cut in the sides of the box are used to locate the position of this frame accurately. A ribbon of aluminium foil, of width 2 mm., upon which the source of $MsTh_2$ is evaporated, is mounted centrally on a rectangular aluminium holder, petroleum jelly being used as the adhesive. This source holder, A, which is illustrated by Figure 1.2, fits into grooves cut in the frame so that the ribbon is parallel to the magnetic field and the source is set at an emission angle of 45°. This effectively reduces the width of the source in a manner discussed in §7 of Chapter 2.

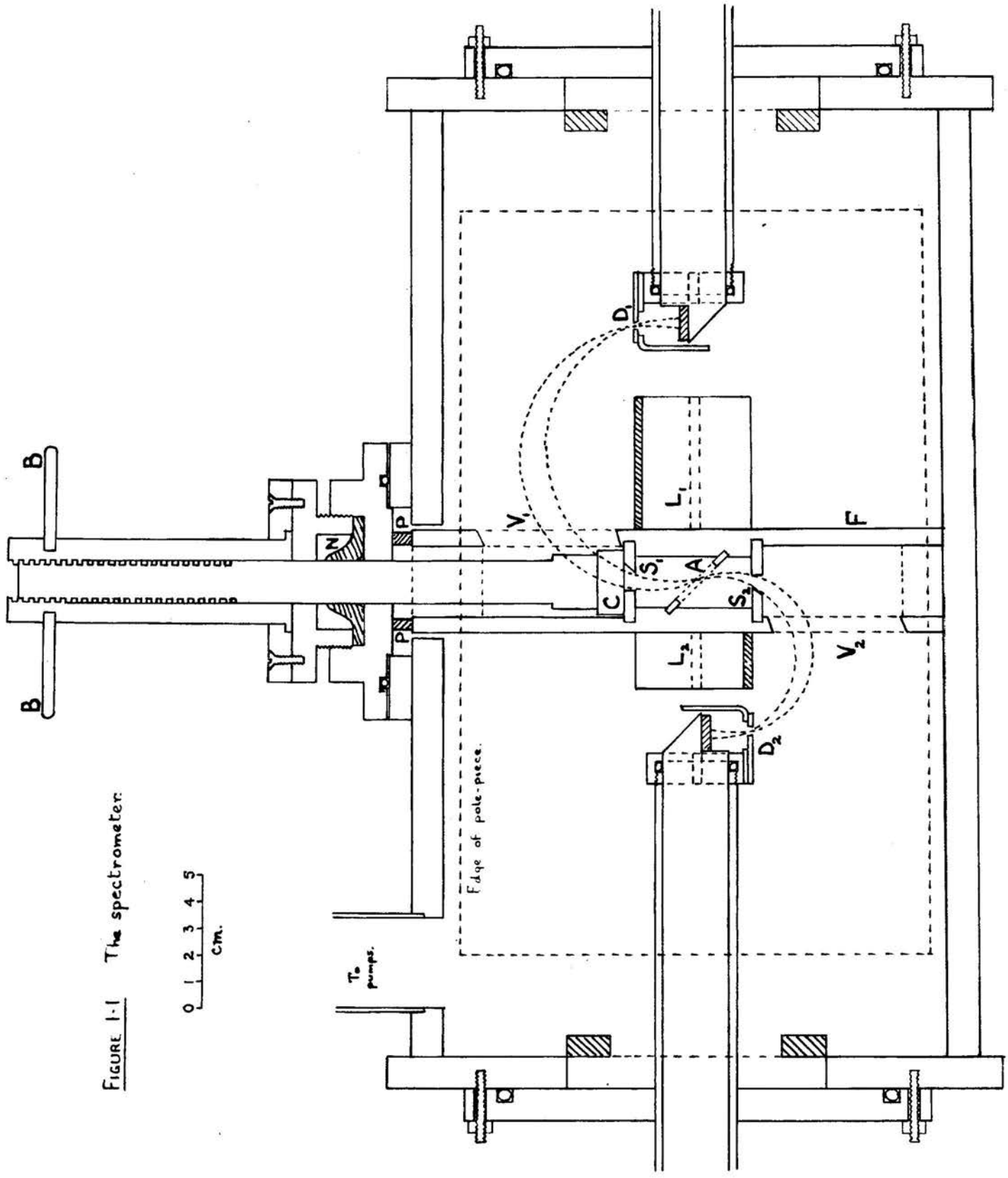

FIGURE 1-1 The spectrometer

Slits, S_1 and S_2, select two sheaves of oppositely moving β-particles which are focused by the magnetic field in the horizontal planes containing the slits of the detectors D_1 and D_2 and the source slits. The source slits, which are constructed of aluminium, fit into grooves in the frame, so that they are situated equidistantly from the source. The vertical slits, V_1 and V_2, which are cut in the sides of the frame, do not impose a further limitation on the sheaves of electrons defined by the slits S_1 and S_2, for trajectories of radii between 2.5 and 6 cm. The port in the top of the box is sealed with a neoprene ring which fits into a circular groove cut in a brass disc. This disc carries a shutter; rotation of the arms, B, causes the aluminium block, C, of square section, to be moved down to cover the slit S_1, and so to cut off electrons from D_1. Phosphor bronze spring strips, P, prevent upward movement of the frame which carries the source, when the shutter is raised. Vacuum sealing of the aperture, through which the rod to operate the shutter moves, is achieved by the neoprene packing, N.

Lead blocks, L_1 and L_2, of suitable thickness, screen the detectors from the γ-radiations emitted by the source. The blocks, which are covered with perspex to reduce scattering of electrons, are held in position by lugs which fit into horizontal grooves cut

in the sides of the box. These grooves also serve to support the detectors, each of which may be moved horizontally by the rotation of arms, situated outside the box. A description of this mechanism is given in Chapter 3, in which the detectors are discussed. Entry of each detector into the box is made through a rectangular port hole in each end of the box, which is again sealed by a neoprene ring fitting into a groove cut into a brass plate. These plates are bolted to the ends of the box. The circular aperture in each plate, through which the detector moves, is sealed by a neoprene packing, similar to that used with the shutter.

§ 2. Calculation of the bevelling of the Source Slits.

For those electron trajectories which lie in a plane perpendicular to the lines of force of the magnetic field, (i.e. lying in the "medial" plane), it is clear that the angle θ made by the tangent to a trajectory, of a particular radius ρ, at one edge of the source slit, with the normal to the plane of the source slit, will vary with the particular point of the source from which the electron is emitted, and with the width of the source slit. This angle will, moreover, depend on the radius of the electron trajectory.

Let the edge of the source slit nearer to the plane of focusing be considered. In this case the angle θ_B will be greatest, for given widths of source

and source slit, when the radius of curvature is a minimum, and the trajectory starts from the edge of the source remote from the image.

Reference to Figure 1.3 shews that

$$\theta_B = \pi - (\phi + \psi) \qquad (1.1)$$

where $$\phi = \arctan \frac{d}{e+s} \qquad (1.2)$$

and $$\psi = \arccos \frac{\sqrt{d^2 + (e+s)^2}}{2\rho} \qquad (1.3)$$

in which:-

d represents the distance between the centre line of the source and that of the source slit,

e is the effective half width of the source. (Tilted sources of width 2b are replaced by horizontal sources of width 2e where e is given by equation 2.48 of § 7, Chapter 2).

s is the half width of the source slit.

Now the mass of aluminium required to stop β -particles of energy ~2MeV is 1.03 gm. per square cm.;[13] the source slits are therefore required to possess a thickness of ~4 mm. when β -particles of this energy are focused.

It is then necessary to know the effective position of the slit cut in this thickness of material, since the distance between the source and the source slit enters into calculations of the radius of curvature. If the aperture defining the slit width were cut in the surface of the material remote from the

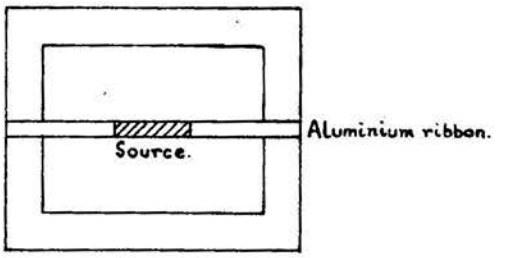

FIGURE 1·2 The source holder. (Actual size).

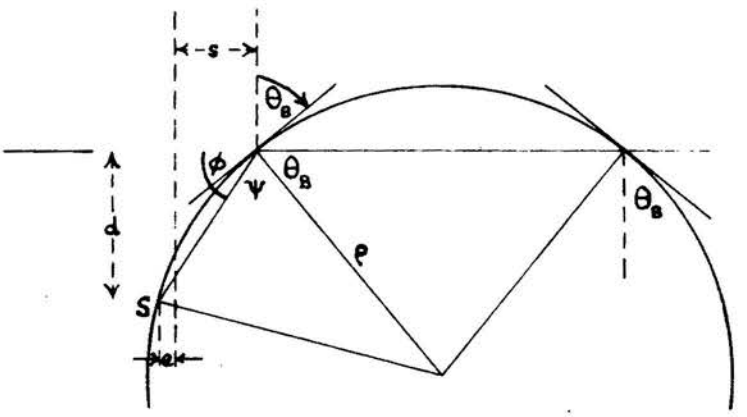

FIGURE 1·3 See text.

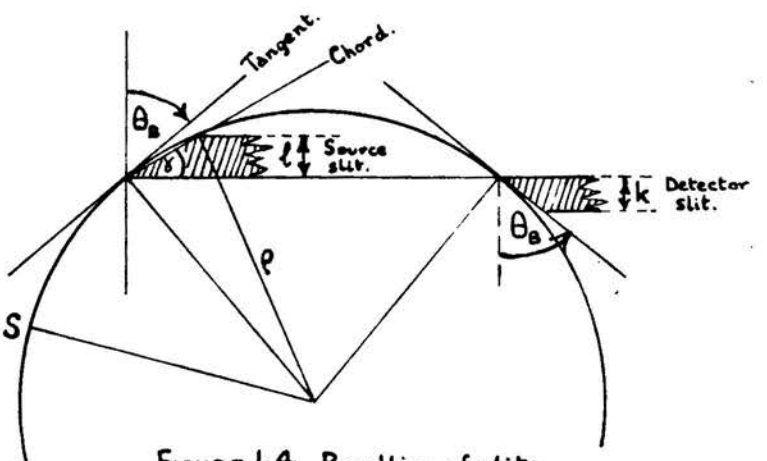

FIGURE 1·4 Bevelling of slits.

source and if the walls of the slit were bevelled to avoid restriction of the trajectories passing through the aperture, scattering of electrons from the walls would occur, due to the entry into the portions of the slit nearer to the source of a sheaf of electrons broader than that finally defined. The defining aperture was therefore cut in the surface of the material nearer to the source and the slit was bevelled so that electrons of the defined sheaf do not again strike the walls.

Inspection of Figure 1.4 shews that the angle of bevel for the edge of the slit nearer to the image will not be θ_B, but the angle between the chord and the normal to the plane of the slit, given by $\frac{\pi}{2} - \gamma$ where γ is given by the expression

$$2\gamma = \arcsin\left(\frac{l}{\rho} + \sin\theta_B\right) - \theta_B \qquad (1.4)$$

in which the thickness of the material of the slit is l. The value of the arcsin term of this expression has to be taken in the second quadrant. The minimum value for ρ is used.

For the edge of the slit remote from the image, the angle θ_A (measured in an anticlockwise direction for Figure 1.5) will be greatest when the electron is emitted from the edge of the source nearer to the image, and follows a trajectory of the maximum radius focused.

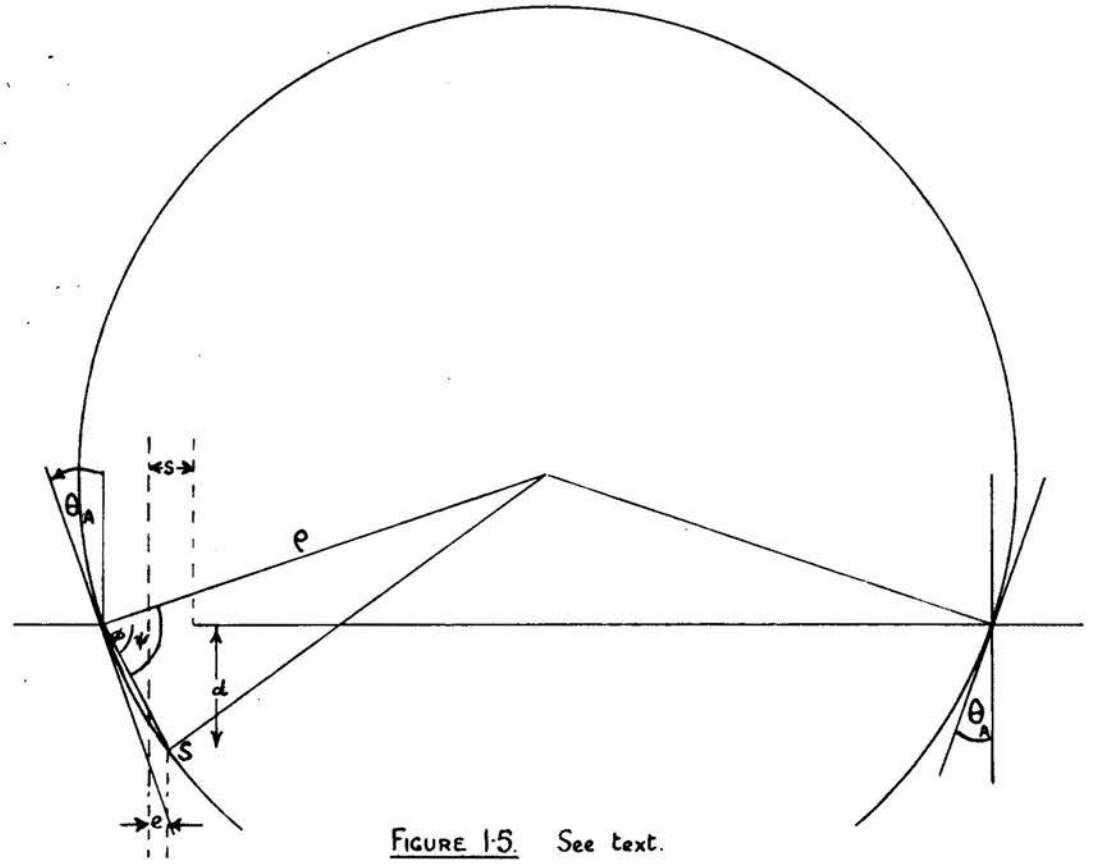

FIGURE 1·5. See text.

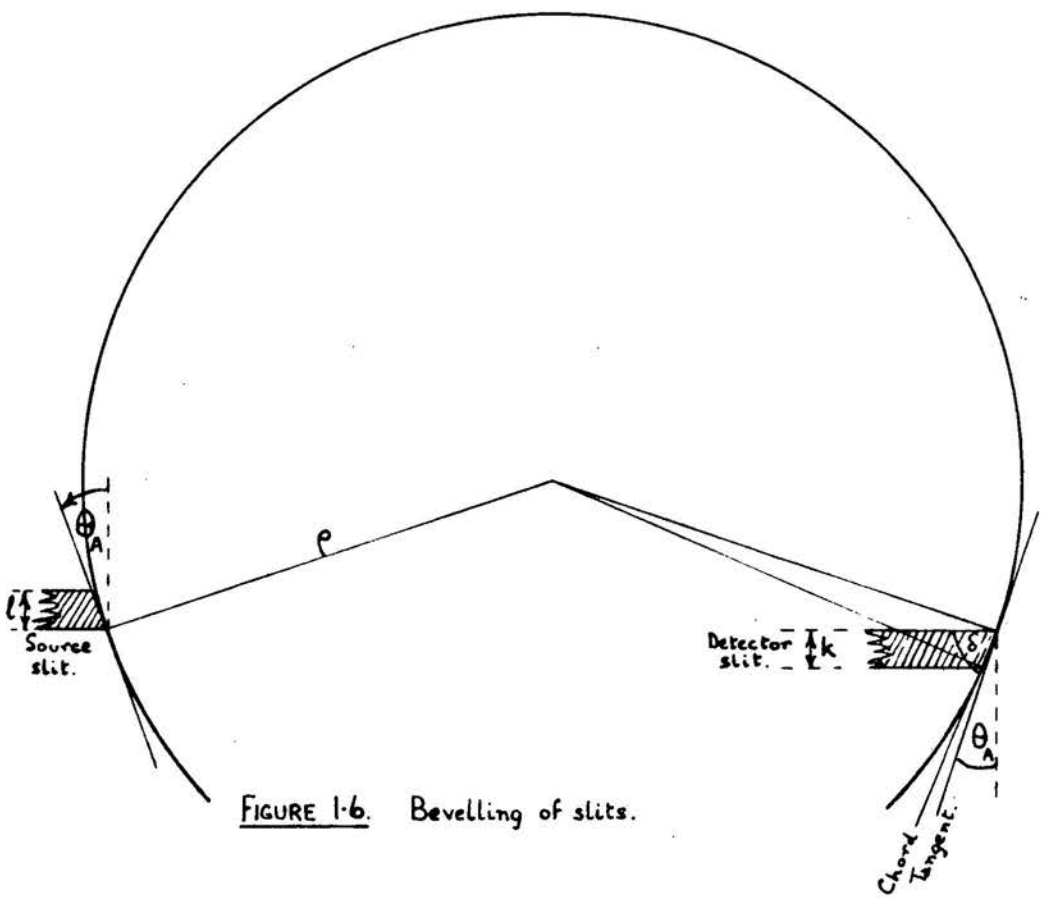

FIGURE 1·6. Bevelling of slits.

In this case

$$\theta_A = \psi - \phi \qquad (1.5)$$

where ψ and ϕ have the meanings given by equations (1.2) and (1.3).

The required angle of bevel for this edge is then given by the value for θ_A at the maximum radius of curvature.

The slight modifications to this bevelling required by electron trajectories lying in planes inclined to the medial plane is neglected.

§ 3. Calculation of the Bevelling of the Counter Slits.

The aperture in the surface of the counter slit upon which electrons are incident is used to define the width of the counter slit, for the reasons given in § 2. For the edge of the slit nearer to the source, Figure 1.5 shews that the angle made by the tangent to the electron trajectory with the normal to the plane of the slit is given by equation 1.5. If the thickness of the brass of the counter slit is k, the angle made by the chord, of Figure 1.6, and the normal to the surface of the slit is given by $\frac{\pi}{2} - \delta$ where

$$2\delta = \arcsin\left(\frac{k}{\rho} + \sin\theta_A\right) - \theta_A \qquad (1.6)$$

when the arcsin term is again taken in the second quadrant.

Reference to Figure 1.4 shews that the angle of bevel for the edge of the counter slit remote from

the source is θ_s, given by equation 1.1.

θ_s is calculated at the smallest radius to be used, whereas δ is found at the largest radius.

The effect of trajectories inclined to the medial plane is again neglected.

CHAPTER 2.

The Theory and the Design of the Spectrometer.

§ 1. Introduction.

The profile of a β-ray line produced by the internal conversion of a γ-ray depends on the exact dimensions and position of the source, on the width of the source slit and on the width and length of the detector slit. This profile extends over an appreciable range of ρ, the radius of curvature of the electron trajectory; the range increases with the source width and with the width of the slits. The minimum width of the source was usually set by practical limitations which are discussed in Chapter 6. The choice of the slit sizes for a given size of source presents difficulties since a compromise has usually to be made between obtaining a large solid angle for collection of the electrons and yet achieving a sufficiently high degree of resolution of the electron momenta. The complexity of the problem is further increased by the dependence of the line profile on the radius of curvature of the electron trajectory. This has the effect of increasing the solid angle at small radii, and increasing the resolution at larger radii. The particular experiment to be performed governed the final choice of slit widths. For example, when searching for lines using one half of the

double spectrometer, the slits were chosen to give a high degree of resolution, with, in consequence, a large reduction in the solid angle. The statistical accuracy in the number of particles counted in a given time interval set the limit to the resolving power which could be used. The search for coincidences between internal conversion lines, on the other hand, demanded both a fairly high degree of resolution and a large solid angle, the emphasis usually being on the latter requirement. Coincidence experiments involving the β-ray continuous spectrum were not so exacting, since the need for a large solid angle became predominantly important.

The study of the variation in the line profile with various changes in the geometry of the spectrometer is therefore of considerable importance.

It has been mentioned that the line profile extends over an appreciable range of ρ. The particular ρ-value within this range to be used in finding the $H\rho$ value of the line is only found from a knowledge of the theoretical line shape. The observed continuous spectrum may be regarded as the integration of elementary line profiles, each of appropriate intensity. For any counter setting, electrons of a certain momentum range may enter the counter, due to the finite width of the counter slits. A "representative" ρ-value for a given setting of the counter on the continuous spectrum which differs from the "representative" ρ in the case of internal

conversion lines, therefore exists, and is found from the theoretical line shape. The numerical value for the solid angle is often of considerable importance and this is only given by the theoretical line shape. The resolving power may be obtained by observing the shape of a single line experimentally, and this provides a useful check on the theory.

In the following paragraphs, the method for determining the theoretical shape of a β -ray line, based to a large extent on the theory due to Li[14], will be given, together with an example of the line shape for slit widths giving high resolution. A more rapid approximate method for studying the manner in which the line shape changes with various changes of the geometry of the spectrometer will then be outlined. Problems relating to the continuous spectrum will be discussed, and finally the most suitable geometrical conditions for various types of experiment will be considered.

§ 2. Li's analytical method for relating points in the source and source slit to image points.

The fundamental equations used by Li to relate points in the source and points in the source slit, with image points will, for the sake of completeness, be re-established in rather more detail.

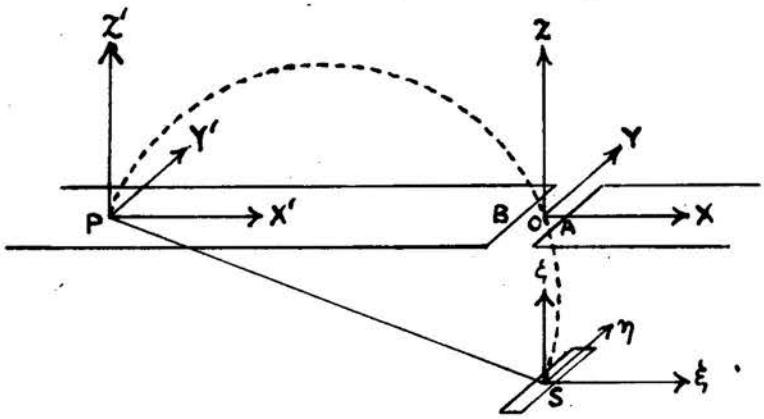

Figure 2.1

Referring to figure 2.1, let ξ, η, ζ be the co-ordinates of the source space, with the centre of the source as origin, S. Let x, y, z be the co-ordinates of the source slit space, with the centre of the slit as origin, O, and let x', y', z' be the co-ordinates of the image space, with origin P determined by making SP the diameter of the circle, radius ρ, passing through O. XOY and X'PY' are coplanar and

OZ and $S\xi$ are collinear. Let PO = a, OS = d, AB = 2s.

The equation of motion of an electron of charge e in a uniform magnetic field of intensity $\underline{H}$ parallel to the y axis is

$$\frac{e}{c}(\underline{v} \wedge \underline{H}) = m\underline{f} \qquad (2.1)$$

where m is the mass of the electron of velocity $\underline{v}$, and acceleration $\underline{f}$.

Letting $\underline{v}$ have components $(\dot{x}, \dot{y}, \dot{z})$ and $\underline{f}$ have components $(\ddot{x}, \ddot{y}, \ddot{z})$ when the electron is at (x, y, z) the following equations are obtained:

$$\left.\begin{aligned} \ddot{x} + \lambda\dot{z} &= 0 \\ \ddot{z} - \lambda\dot{x} &= 0 \end{aligned}\right\} \qquad (2.2a)$$

and

$$\ddot{y} = 0 \qquad (2.2b)$$

where

$$\lambda = \frac{eH}{mc} \qquad (2.3)$$

Integration of the simultaneous differential equations 2.2a gives, for the complementary functions,

$$x = \frac{u_z}{\lambda}\cos\lambda t + \frac{u_x}{\lambda}\sin\lambda t$$

$$y = -\frac{u_x}{\lambda}\cos\lambda t + \frac{u_z}{\lambda}\sin\lambda t$$

where the constants of integration are determined in terms of the components of the initial velocity (u_x, u_y, u_z).

The particular integrals involve two further constants of integration given by the initial co-ordinates of the electron in the (x, y, z) frame, viz.

$(\xi, \eta, -d)$, where, for the moment, attention is confined to sources set at an emission angle of 0° (i,e. sources lying in the (ξ, η) plane).

The complete solution of equations 2.2a is

$$\left.\begin{aligned} x &= \frac{1}{\lambda}\left[u_x \cos\lambda t + u_z \sin\lambda t - (u_z - \lambda\xi)\right] \\ z &= \frac{1}{\lambda}\left[-u_x \cos\lambda t + u_z \sin\lambda t + (u_x - \lambda d)\right] \end{aligned}\right\} \qquad (2.4a)$$

Equation 2.2b may be integrated directly to give

$$y = \eta + u_y t \qquad (2.4b)$$

where the y co-ordinate possesses this value at a time t.

The space co-ordinates $(\frac{u_x}{\lambda}, \frac{u_y}{\lambda}, \frac{u_z}{\lambda})$ may now be related to spherical polar co-ordinates (ρ, Ψ, ϕ) according to the equations

$$\left.\begin{aligned} u_x &= \lambda\rho \sin\Psi \sin\phi \\ u_y &= \lambda\rho \cos\Psi \\ u_z &= \lambda\rho \sin\Psi \cos\phi \end{aligned}\right\} \qquad (2.5)$$

and the equations 2.4a and 2.4b then become

$$\left.\begin{aligned} x - \xi &= -(\rho\sin\Psi)(\cos\phi - \cos\chi) \\ z + d &= (\rho\sin\Psi)(\sin\phi + \sin\chi) \\ y - \eta &= (\rho\cos\Psi)(\chi + \phi) \end{aligned}\right\} \qquad (2.6)$$

where $$\chi = \lambda t - \phi \qquad (2.7)$$

The co-ordinates of the points of intersection of an electron with the slit plane and with the image plane are required, and z is therefore set equal to zero giving

$$d = (\rho\sin\Psi)(\sin\phi + \sin\chi_1) \qquad (2.8)$$

The parameters (ρ, ψ, ϕ) are independent of time, but χ depends on time in accordance with equation 2.7.

With z = 0, equation 2.8 is satisfied when $\chi_1 = \lambda t_1 - \phi$. This is the smallest value of t which gives a solution and therefore corresponds to the case in which the electron cuts the source slit plane. Hence the point of intersection of the electron with the source slit plane is given by the equations

$$\left.\begin{aligned} x - \xi &= -(\rho \sin\psi)(\cos\phi - \cos\chi_1) \\ y - \eta &= (\rho\cos\psi)(\chi_1 + \phi) \\ z &= 0 \end{aligned}\right\} \qquad (2.9)$$

in agreement with Li's equations 2.

The next value of χ which satisfies equation 2.8 is

$$\chi_2 = \pi - \chi_1 = \lambda t_2 - \phi \qquad (2.10)$$

Substituting this value for χ_2 in equations 2.6, the point of intersection of the electron with the image plane is given by

$$\left.\begin{aligned} x - \xi &= -(\rho \sin\psi)(\cos\phi + \cos\chi_1) \\ y - \eta &= (\rho\cos\psi)(\pi - \chi_1 + \phi) \\ z &= 0 \end{aligned}\right\} \qquad (2.11)$$

Transferring the origin of co-ordinates to the point P, equations 2.11 become

$$\left.\begin{aligned} x' - \xi &= a - (\rho \sin\psi)(\cos\phi + \cos\chi_1) \\ y' - \eta &= (\rho\cos\psi)(\pi - \chi_1 + \phi) \\ z' &= 0 \end{aligned}\right\} \qquad (2.12)$$

in agreement with Li's equations (3).

By eliminating Ψ, ϕ, χ from the two sets of equations 2.9 and 2.12 a relation between (x, y, z) and (x', y', z') may be derived.

This elimination is facilitated by setting

$$A = \frac{\phi + \chi}{2} \qquad \text{and} \qquad B = \frac{\phi - \chi}{2}$$

to give the equations in the form

$$d = 2(\rho \sin\Psi) \sin A \cos B \tag{2.13a}$$

$$x - \xi = 2(\rho \sin\Psi) \sin A \sin B \tag{2.13b}$$

$$y - \eta = (\rho \cos\Psi)(2A) \tag{2.13c}$$

$$x' - \xi - a = -2(\rho \sin\Psi) \cos A \cos B \tag{2.13d}$$

$$y' - \eta = (\rho \cos\Psi)(\pi + 2B) \tag{2.13e}$$

Equations (a) and (b) give

$$\frac{x - \xi}{d} = \tan B$$

Equations (d) and (a), give

$$(x' - \xi - a)^2 + d^2 = 4\rho^2 \sin^2\Psi \cos^2 B$$

and equation (e) yields

$$\frac{(y' - \eta)^2}{(\pi + 2B)^2} = \rho^2 \cos^2\Psi$$

Hence

$$\rho^2 = \frac{(y' - \eta)^2}{(\pi + 2B)^2} + \frac{(x' - \xi - a)^2 + d^2}{4\cos^2 B} \tag{2.14}$$

This equation reduces to

$$(x' - \xi)\left(1 - \frac{x' - \xi}{2a}\right)\left[1 - \frac{(x - \xi)^2}{d^2}\right] = \frac{2(y' - \eta)^2}{\pi^2 a}\left(1 + \frac{2B}{\pi}\right)^{-2} + \frac{2\rho^2}{ad^2}(x - \xi)^2$$

and with obvious approximations becomes

$$x' - \xi \simeq \frac{2(y' - \eta)^2}{\pi^2 a} + \frac{2\rho^2}{ad^2}(x - \xi)^2 \tag{2.15}$$

Equations 2.13(c) and (e) together with equations (a) and (d) yield

$$\frac{y-\eta}{y'-\eta} = \frac{2\arctan\frac{d}{a+\xi-x'}}{\pi + 2\arctan\frac{x-\xi}{d}} \qquad (2.16)$$

$$= \frac{2\left[\frac{d}{a+\xi-x'} - \frac{d^3}{3(a+\xi-x')^3} + \cdots\right]}{\pi + 2\left[\frac{x-\xi}{d} - \frac{(x-\xi)^3}{3d^3} + \cdots\cdots\right]}$$

$$= \frac{2d\left[\frac{1}{1-\frac{x'-\xi}{a}} - \cdots\cdots\right]}{\pi a\left[1 + \frac{2(x-\xi)}{\pi d} - \cdots\right]}$$

$$\simeq \frac{2d}{\pi a} \qquad (2.17)$$

In this approximation terms of the same sign and similar order of magnitude are neglected in the numerator and in the denominator.

Equations 2.14 and 2.16 are exact, whereas equations 2.15 and 2.17 are Li's approximations to the exact solution; these equations relate source points, source slit points, and image points, and form the basis of Li's method for the determination of line shapes.

The approximations made in deriving equations 2.15 and 2.17 are necessary to obtain the Jacobian of the transformation

$$dx\,dy = J\,dx'\,dy'$$

in a form which may be handled in the later analysis.

§ 3. Geometrical method for establishing the basic equations 2.15 and 2.17.

The nature of the approximations made in establishing equations 2.15 and 2.17 is more easily seen when the equations are derived geometrically.

Figure 2.1 shews that the electron trajectory of radius ρ, starting from the centre of the source, S, and passing through the centre of the source-slit, O, strikes the image plane at the point P. A similar electron trajectory, again in a plane perpendicular to the field, but this time passing through the point A of the source-slit possesses the equation (referred to O as origin),

$$\left(x + \frac{s}{2} + \frac{d}{2}\sqrt{\frac{a^2-s^2}{d^2+s^2}}\right)^2 + \left(z + \frac{d}{2} + \frac{s}{2}\sqrt{\frac{a^2-s^2}{d^2+s^2}}\right)^2 = \rho^2 \qquad (2.18)$$

and hence it strikes the image plane at a point, distance ϵ_1, from P, measured along the positive X' axis where

$$\epsilon_1 = a - d\sqrt{\frac{a^2-s^2}{d^2+s^2}} \qquad (2.19)$$

Neglecting terms of the order of $\frac{s^4}{a^4}$ and $\frac{s^4}{d^4}$, this becomes

$$\epsilon_1 = \frac{2s^2\rho^2}{ad^2} \qquad (2.20)$$

Proceeding now to the three-dimensional case, an electron with the same momentum, starting from the source point S, but passing now through the point $(0, \ell, 0)$ of the source-slit, will arrive in the image plane at the point whose co-ordinates are $(\epsilon_1, \epsilon_3, 0)$;

ϵ_2 and ϵ_3 are found as follows.

The trajectory of the electron is that of a helix on a cylinder of radius $\rho\cos\theta$ where $(\pi/2 - \theta)$ is the zenith angle of the trajectory at S, as shewn in figure 2.2.

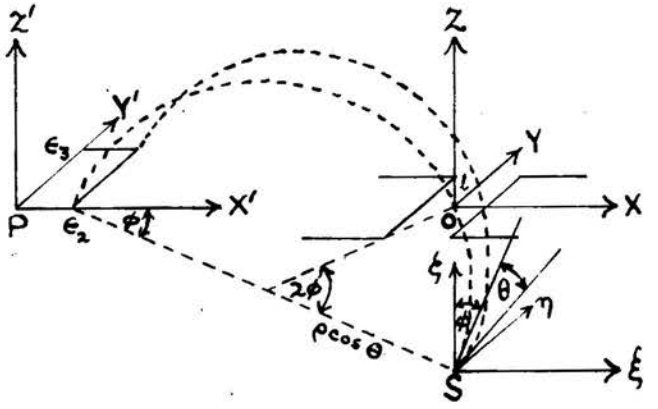

Figure 2.2

Reference to the figure shews that

$$\tan\theta = \frac{\ell}{\text{arc SO}} = \frac{\ell}{2\phi\rho\cos\theta}$$

where ϕ is the azimuth of the trajectory at S.

Hence

$$\sin\theta = \frac{\ell}{2\phi\rho}$$

A little consideration will shew that

$$\epsilon_2 = \frac{\ell^2}{2\phi^2 a}$$

and

$$\epsilon_3 = \frac{\pi\ell}{2\phi}$$

in which terms like $\frac{\ell^4}{\phi^4 a^4}$ have been taken as being negligibly small compared with unity.

If ϕ is now replaced by d/a, these equations become:-

$$\epsilon_2 = \frac{\ell^2 a}{2d^2} \qquad (2.21)$$

and

$$\epsilon_3 = \frac{\pi a \ell}{2d} \qquad (2.22)$$

An electron which leaves the point $(\xi, \eta, 0)$ of the source, and passes through the point (x, y, 0) of the source-slit will therefore arrive at the image at the point (x', y', 0) where

$$x' = \epsilon_1 + \epsilon_2 + \xi$$

$$y' = \epsilon_3 + \eta$$

The appropriate expressions for ϵ_1, ϵ_2 and ϵ_3, obtained by substituting $(\xi - x)$ for s, and $(y - \eta)$ for ℓ in equations 2.20, 2.21 and 2.22, give:-

$$x' - \xi = \frac{2\rho^2}{ad^2}(x-\xi)^2 + \frac{a}{2d^2}(y-\eta)^2$$

$$\frac{y-\eta}{y'-\eta} = \frac{2d}{\pi a}$$

again in agreement with Li's equations 2.15 and 2.17.

§4. Errors in the approximations.

To test the extent of the approximations made in adopting these equations, various values for x, y', ξ and η may be substituted into equation 2.14 and the corresponding (exact) values for x' found. The values of x' obtained from the approximate equation 2.15 may then be compared with the corresponding exact values for x'. The greatest error occurs when a particle leaves a corner of the source remote from the image, and passing through the source slit touching the edge nearer to the image, falls in the image space after travelling the maximum distance in the direction parallel to the magnetic field; that is half the source length, plus half the length of the counter window.

For a source of area 2 mm. by 1 cm. set at an emission angle of 45°,* a source slit of 4 mm. and a detector slit of length 1.5 cm. the comparative figures when ρ = 3 cm., are as follows:-

Exact value for x' = 0.1474 mm.

Approximate value for x' = 0.1437 mm.

The error in y' produced by using equation 2.17 is obtained by substituting the value of y from equation 2.16 for the chosen values of x, y', ξ, and η into equation 2.17 and solving for y'.

For the worst case the values are:-

* See §7.

Exact value for y' = -.750 mm.

Approximate value for y' = -.802 mm.

The errors involved for trajectories with planes more nearly perpendicular to the magnetic field are considerably smaller. The method of approximation does not always over-estimate the magnitude of y', for in most cases changing the sign of x produces an error of opposite sign in the approximate y'. The errors in x' are similarly compensated.

§ 5. Domains in the source plane which contribute to the intensity at an image point.

§ 5.1 Introduction.

A method will now be discussed for establishing domains in the source plane which are capable of making a contribution to the intensity at a particular image point, chosen for convenience on the X' axis. Only electrons of momentum p will be considered; hence, for the medial plane, (that is the plane through the centre of the source and source slit at right angles to the magnetic field), only those trajectories of radius $\rho = \frac{pc}{He}$ will be discussed. In practical cases the source occupies only a narrow strip of the source plane, but all points of the source plane capable of contributing to the image intensity of a chosen point in the image will at first be examined.

§ 5.2 The effect of variation of the image point x'.

Reference to figure 2.3 shews that, through the image point x', which has co-ordinates (x', 0, 0) two circles of radius ρ may be drawn in the medial plane to touch the edge of B of the source slit.* Let these circles cut the source plane (in the neighbourhood of the source slit) at points B_R and B_L respectively,

---

* The edge of the source slit near to the image will always be referred to as edge "B". The edge remote from the image will be called edge "A".

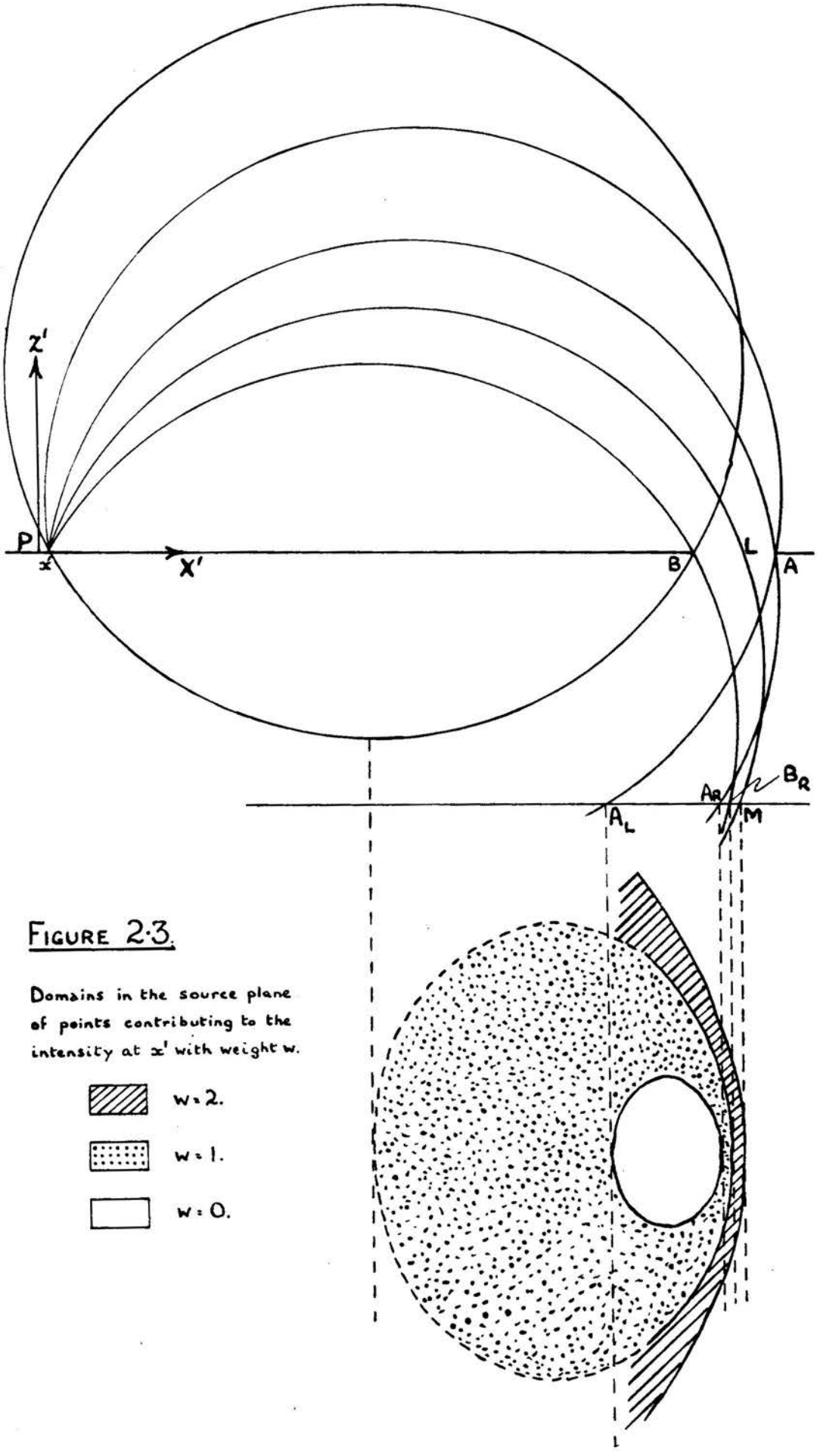

FIGURE 2.3.

Domains in the source plane of points contributing to the intensity at x' with weight w.

w = 2.

w = 1.

w = 0.

where B_R is always to the right of B_L in the diagram. In the particular case chosen a real point B_L does not exist. Similarly, two circles of radius ρ may be drawn through the edge A of the slit; these cut the source plane at points A_R and A_L.

The remaining circle shewn cuts the plane of the slit at L and the source plane at M where L lies perpendicularly above M.

Let x' be chosen so that L lies in the slit. Then through every point lying between A_R and M a circle (of radius ρ) may be drawn to pass through the image point x'; every member of this set of circles (referred to as set 1) will cut the slit at a point between A and L. A second, and quite distinct, set of circles (set 2) may be drawn through the point x' and all points lying between B_R and M. Members of this set of circles are distinguished from those of the first set by their intersections with the slit, which now occur between B and L. No circle of radius ρ may be drawn through the point x' to pass through the slit and to cut the source plane between A_L and A_R. Circles may, however, be drawn through the right hand region of the slit to cut the source plane at points to the left of A_L; this set of circles (set 3) is finally limited in the case chosen by the member which is tangential to the source plane.

Let the point x' now move to the right; the points L and M will move with x'. When L lies to the right of A as shewn in figure 2.4 the distinction between the first two sets of circles disappears, and a single set of circles of radius ρ may be drawn through the new x' to pass through points lying between B_R and A_R ; members of this set of circles cut the slit at points between B and A. The circles of set 3 no longer exist since A_L is not a real point.

When the image point x' takes positions to the left of that originally considered, a point is reached (when $x'A = 2\rho$) beyond which circles may no longer be drawn through the edge "A" of the slit. Such a case is illustrated in figure 2.5, in which $x'C = 2\rho$; the trajectory through C cuts the source plane at C_{RL} . The sets of circles 1 and 3 now merge; members of the set originating at points to the left of C_{RL} (limited again by the circle tangential to the source plane which cuts the slit at D) pass through points lying between D and C of the slit; those circles originating at points between C_{RL} and M may only pass through the slit at points between C and L. Set 1, given by points between B_R and M have corresponding slit points between B and L as previously discussed.

§ 5.3 Extension to three dimensions.

The discussion above has been limited to

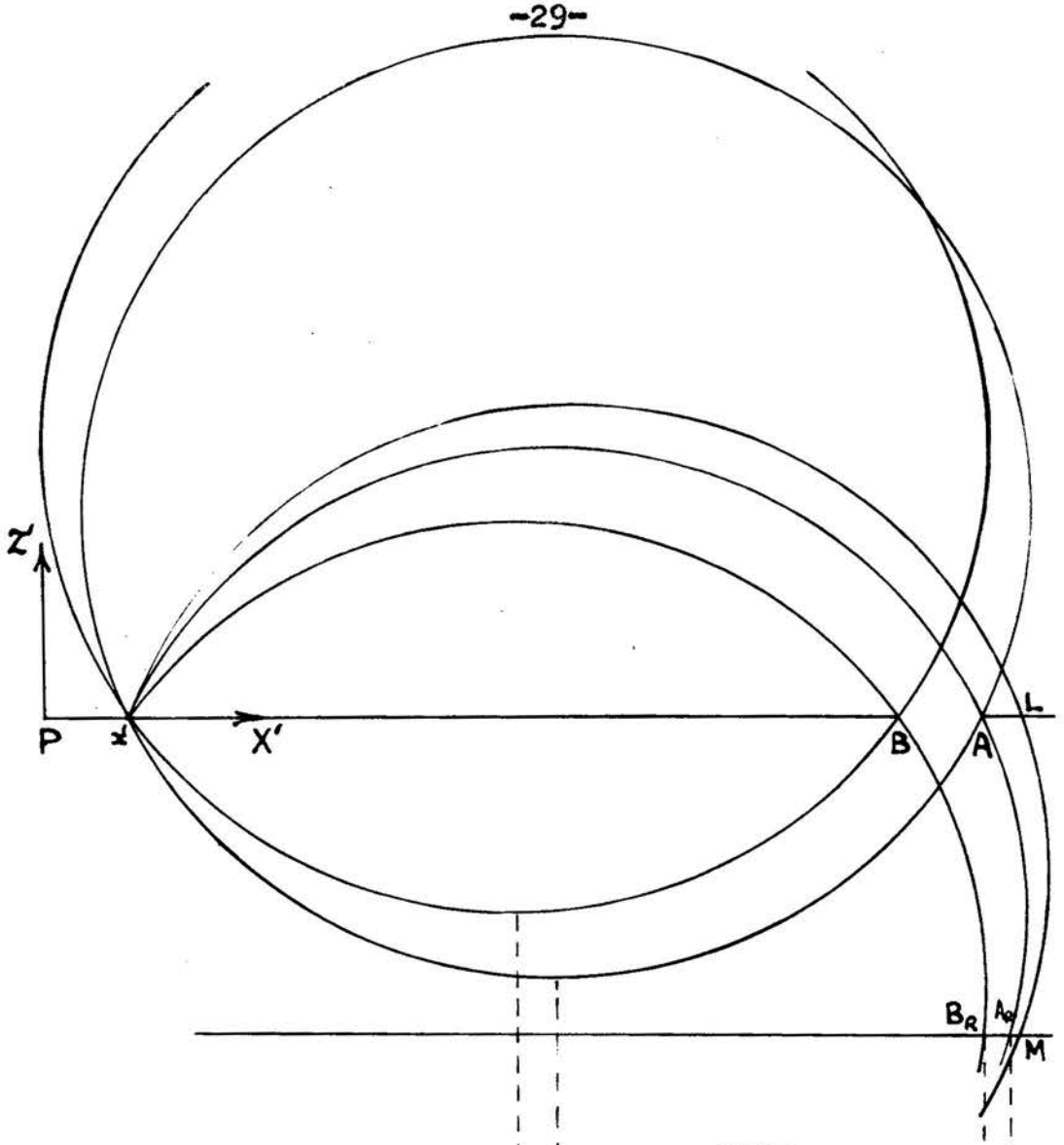

FIGURE 2·4.

Domains in the source plane of points contributing to the intensity at x' with weight w.

w=2.

w=1.

w=0.

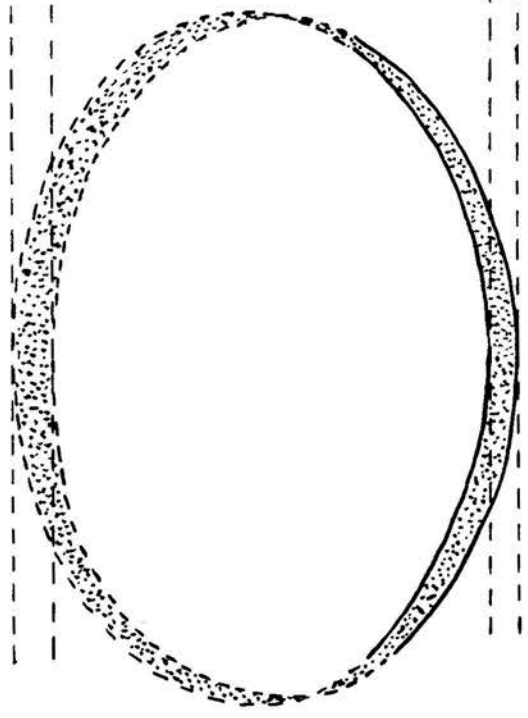

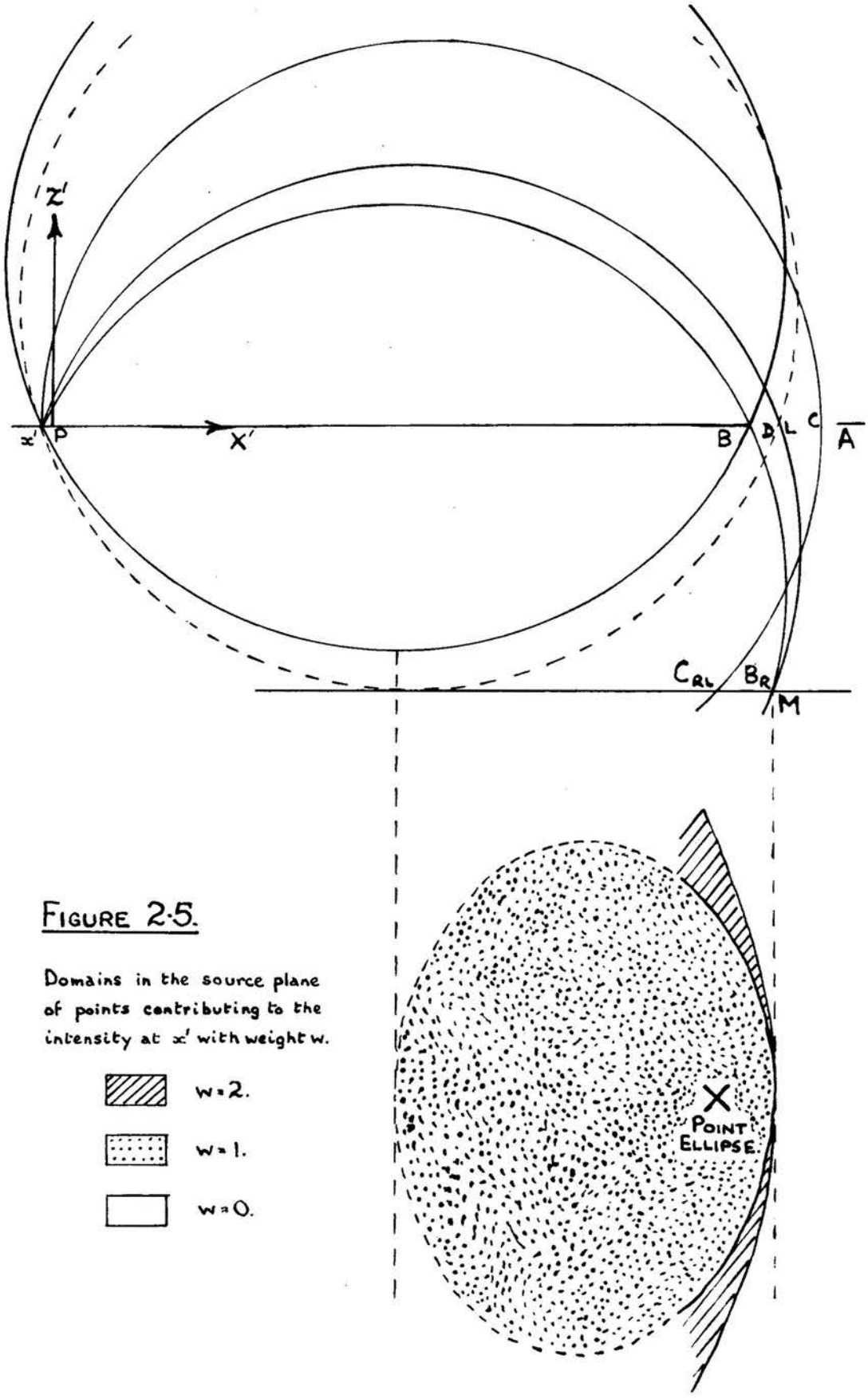

FIGURE 2·5.

Domains in the source plane of points contributing to the intensity at x' with weight w.

w = 2.

w = 1.

w = 0.

electron trajectories lying in the medial plane. In the three dimensional case it is necessary to find the domains of the source plane which contribute to the image point x' chosen. The boundaries of the domains are found by substituting the appropriate slit and image co-ordinates into equation 2.15. The results are:

(1) Boundary set by the edge "A" of the slit.

When x = s and y' = 0 equation 2.15 becomes

$$x' - \xi = \frac{2\eta^2}{\pi^2 a} + \frac{2\rho^2}{ad^2}(s-\xi)^2 \qquad (2.23)$$

This is the equation to an ellipse, referred to as the "A" ellipse.

Some features of the ellipse are:-

Centre of symmetry:-

$$\xi_{A_1} = -\frac{ad^2 - 4s\rho^2}{4\rho^2} \quad ; \quad \eta_{A_1} = 0 \qquad (2.24)$$

Minor axis:-

$$a_A = \frac{d}{4\rho^2}\sqrt{a\left\{ad^2 - 8\rho^2(s-x')\right\}} \qquad (2.25)$$

Major axis:-

$$b_A = \frac{\pi}{4\rho}\sqrt{a\left\{ad^2 - 8\rho^2(s-x')\right\}} \qquad (2.26)$$

The source points A_L and A_R, given by the co-ordinates of the extremities of the minor axis are:-

$$\xi_{A_L} = \frac{1}{4\rho^2}\left[-\sqrt{ad^2\left\{ad^2 - 8\rho^2(s-x')\right\}} - ad^2 + 4s\rho^2\right] \quad * \quad (2.27)$$

$$\xi_{A_R} = \frac{1}{4\rho^2}\left[\sqrt{ad^2\left\{ad^2 - 8\rho^2(s-x')\right\}} - ad^2 + 4s\rho^2\right] \quad * \quad (2.28)$$

(2) Boundary set by the edge "B" of the slit.

This is obtained by putting $x = -s$ and $y' = 0$ into equation 2.15.

The equation becomes

$$x' - \xi = \frac{2\eta^2}{\pi^2 a} + \frac{2\rho^2}{ad^2}(s+\xi)^2 \quad (2.29)$$

This gives a second ellipse, referred to as the "B" ellipse; this has features similar to those of ellipse "A" with s replaced by -s.

(3) Boundary set by trajectory passing through the slit immediately above the source point.

This is given by putting $x = \xi$ and $y' = 0$ into equation 2.15:-

$$x' - \xi = \frac{2\eta^2}{\pi^2 a} \quad (2.30)$$

This is the equation to a parabola. The co-ordinate of the apex M, is:-

$$\xi_M = x' \quad (2.31)$$

The shape of the domains of the source plane which contribute to the various image points already discussed are shewn in figures 2.3, 2.4 and 2.5. The

* These equations are only applicable to cases in which ξ is small, because of the approximations of § 2.

following comments apply to the cases considered.

Figure 2.3.

The approximate equations give satisfactory values for ξ_{A_R} , ξ_{B_R} and ξ_M , but the value for ξ_{A_L} is unreliable, since ξ is large. Moreover, the approximate equations give a real value for ξ_{B_L} . The exact shape of the domains when ξ is large is therefore uncertain. Those regions of the source contributing doubly and singly to the image point are distinguished by shading.

Figure 2.4.

The same general remarks apply to this case.

Figure 2.5.

Equations 2.25 and 2.26 shew that the ellipse "A" shrinks to a point when x' takes the value x'_A given by:-

$$x'_A = \frac{8\rho^2 s - ad^2}{8\rho^2} \qquad (2.32)$$

Hence electrons of momentum ρ with trajectories touching the edge A of the slit contribute only to those image points for which $x' > x'_A$.

For the case illustrated by figure 2.5, let $CA = q$; then, when $x' = \frac{8\rho^2 s - ad^2}{8\rho^2} - q$ and $x = s - q$, the ellipse again shrinks to a point.

§ 5.4 Exact equations corresponding to equations 2.27, 2.28 and 2.32.

It is interesting to digress now to consider

the exact equations corresponding to approximate equations 2.27, 2.28 and 2.32.

With y' and η set equal to zero, equation 2.14 is a quartic in ξ .

For the edge "A" of the source, x is set equal to s.

The solutions of the equation are more easily written by putting:-

$$M = \frac{x' - a + s}{2}$$

and

$$N = \frac{x' - a - s}{2}$$

The solutions then take the form:-

$$\left.\begin{aligned} \xi_{A_R} &= M + \sqrt{N^2 - d^2 + 2d(\rho^2 - N^2)^{1/2}} \\ \xi_{A_L} &= M + \sqrt{N^2 - d^2 - 2d(\rho^2 - N^2)^{1/2}} \end{aligned}\right\} \qquad (2.33)$$

(The other two solutions correspond to the second intersections of the circles with the source plane in the neighbourhood of the image).

The corresponding points for edge B of the slit are found by interchanging M and N.

Equation 2.32, in its exact form, is

$$x'_A = s + a - 2\rho \qquad (2.34)$$

which is obtained from the condition that $\xi_{A_R} = \xi_{A_L}$.

§ 5.5 Typical source domains in practical cases.

In practice the source occupies only a narrow region of the source plane (parallel to the η axis) and is situated either symmetrically about the origin of

source co-ordinates or just to the left or to the right of the origin. The effect of off-setting the source is discussed in § 10·3.

For suitable positions of the point x', traversing the X' axis of the image space, boundaries will exist in the limited region of the source plane occupied by the source.

These boundaries select those domains in the source capable of making either zero, single or double intensity contributions to the image point in question. The manner in which they do so depends on the position of the centre of symmetry of the ellipse "A" relative to the centre of the source.

The case which has been discussed is one of small radius of curvature, so that the centre of symmetry of the ellipse "A" lies to the left of the source. Equation 2.24 shews that, as ρ increases, this centre of symmetry moves to the right until when

$$\rho^2 = \frac{ad^2}{4s} \qquad (2.35)$$

it occupies a position at the origin of the source plane co-ordinates.

Thus three distinct cases have to be examined, with ρ^2 less than, equal to, and greater than $\frac{ad^2}{4s}$ respectively.

Let the source, of width 2b and of length 2k, be situated symmetrically about the origin of the source

plane co-ordinates.

Case 1. $\rho^2 < \frac{ad^2}{4s}$.

The diagrams of figure 2.6 shew the general character of the source domains as x' traverses the X' axis of the image.

As x' increases, the axes of the ellipses increase, their centres remaining at rest; hence the region lying to the left of A_L of figure 2.3, which is capable of making a contribution of single intensity to the image, can never lie in the source.

Case 2. $\rho^2 = \frac{ad^2}{4s}$.

The A ellipse is now situated symmetrically about the origin of the source plane co-ordinates.

When $\rho^2 = \frac{ad^2}{4s}$ is substituted into equation 2.32, it is found that the A ellipse cannot exist for $x' < \frac{s}{2}$. This ellipse has shrunk to a point when $x' = \frac{s}{2}$ and assumes its usual form when $x' > \frac{s}{2}$.

The centre of symmetry of ellipse B is situated at $\xi_{B_1} = -2s$, and the ellipse shrinks to a point for $x' = -\frac{3s}{2}$.

When the point C of figure 2.5 has a co-ordinate x in the slit, $x' = \frac{2x-s}{2}$ and C_{RL} has a ξ co-ordinate in the source plane of $-(s-x)$. C_{RL} and the centre of symmetry of ellipse B (which has shrunk to a point) are coincident when $x = -s$; and C_{RL}, the centre of symmetry of the "A" ellipse, and the point B_R (of figure

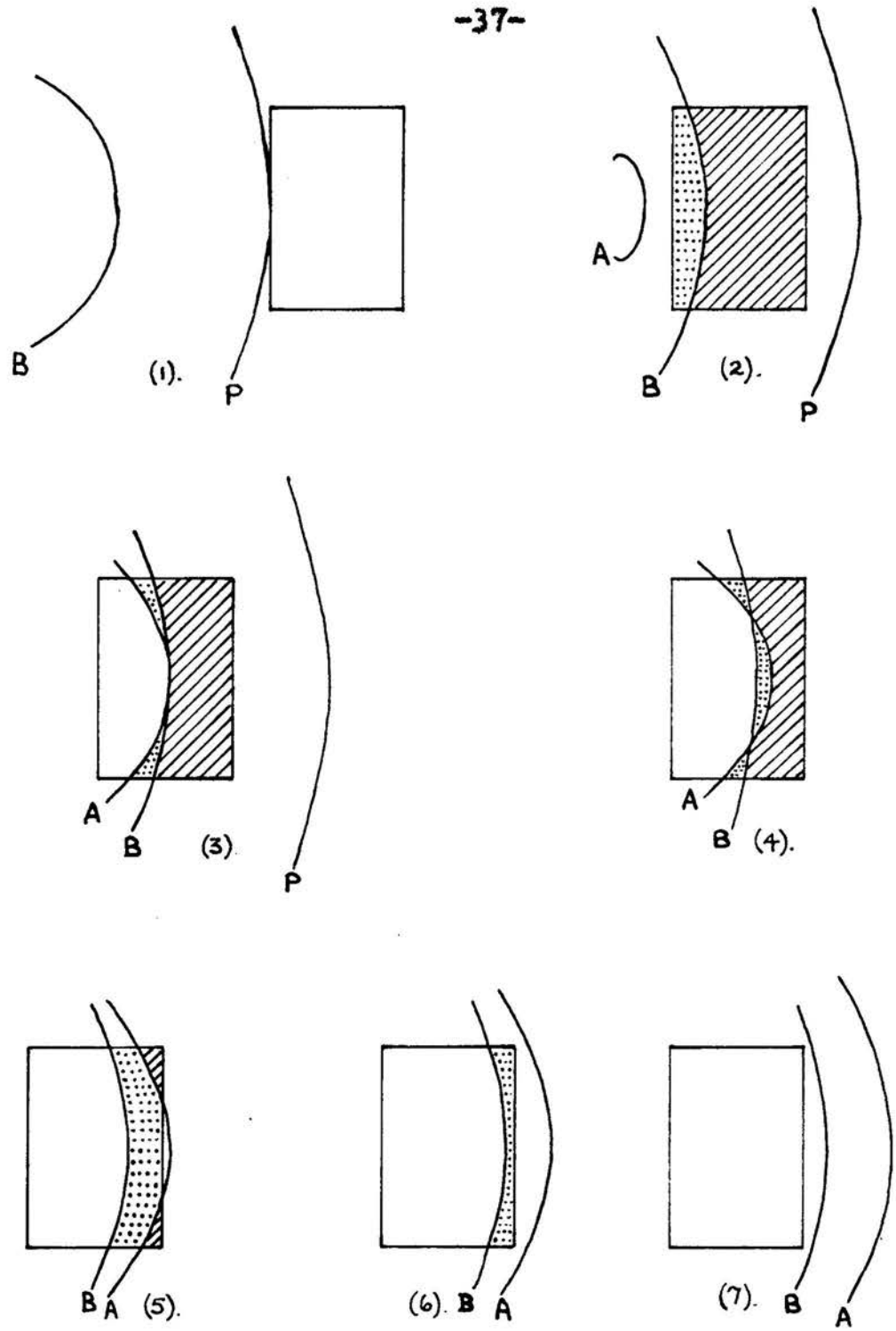

A ≡ Ellipse A.
B ≡ Ellipse B.
P ≡ Parabola.

Source domain of weight 2.
" " " " 1.
" " " " 0.

FIGURE 2·6. Typical source domains, when $\rho^2 < \frac{ad^2}{4s}$, for various image points (see text).
Not drawn to scale.

2.5) are coincident when x = s.

For values of x between -s and + s, C_{RL} lies to the left of B_R.

Figure 2.7 illustrates the types of domain encountered with this radius of curvature.

Case 3. $\rho^2 > \frac{ad^2}{4s}$.

Let $\rho^2 = \frac{+ad^2}{4s}$ where r > 1.

The centre of symmetry of the "A" ellipse is situated at $\xi_{A_1} = \frac{+-1}{+} s$, and the ellipse is real when $x' > \frac{2+-1}{2+} s$.

The centre of symmetry of ellipse B is at $\xi_{B_1} = -\frac{+-1}{+} s$. This ellipse is real when $x' > -\frac{2++1}{2+} s$.

For values of x' between these limits, the point C (of figure 2.5) lies between the slit points B and A. When C has a slit co-ordinate = x, $x' = \frac{2+x-s}{2+}$, and C_{RL} has a ξ co-ordinate of $-\left(\frac{s}{+} - x\right)$. C_{RL} lies to the right of B_R in the source.

Figure 2.8 illustrates the types of domain encountered in this case

General case.

In all cases source domains lying between the following limits contribute to the intensity of the particular image point:-

(1) From the left hand side of the "A" ellipse to the left hand side of ellipse "B".

(2) From the right hand side of ellipse "B" to the

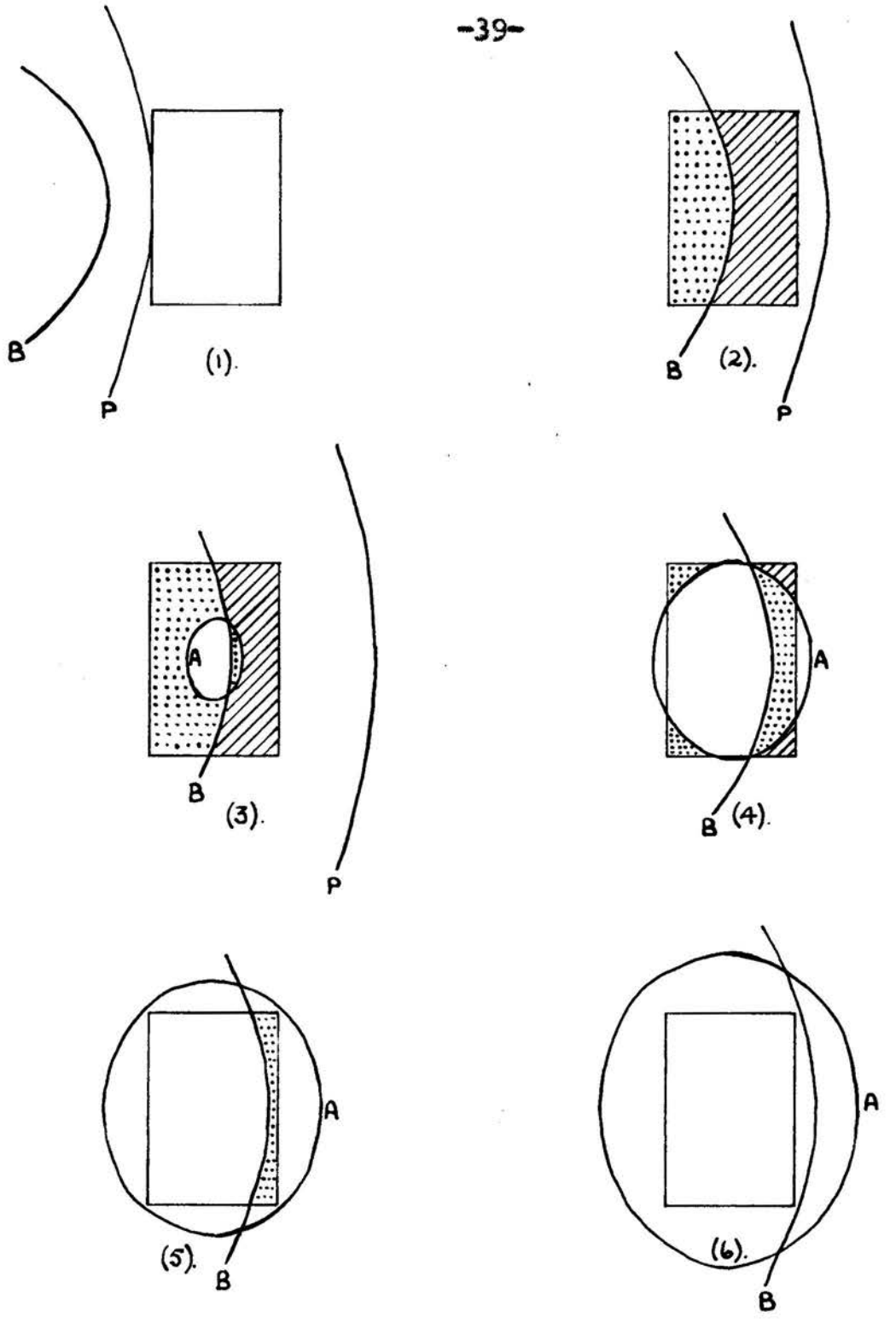

A ≡ Ellipse A.
B ≡ Ellipse B.
P ≡ Parabola.

Source domain of weight 2.
" " " " 1.
" " " " 0.

FIGURE 2·7. Typical source domains, when $\rho^2 = \frac{ad^2}{4s}$, for various image points (see text).
Not drawn to scale.

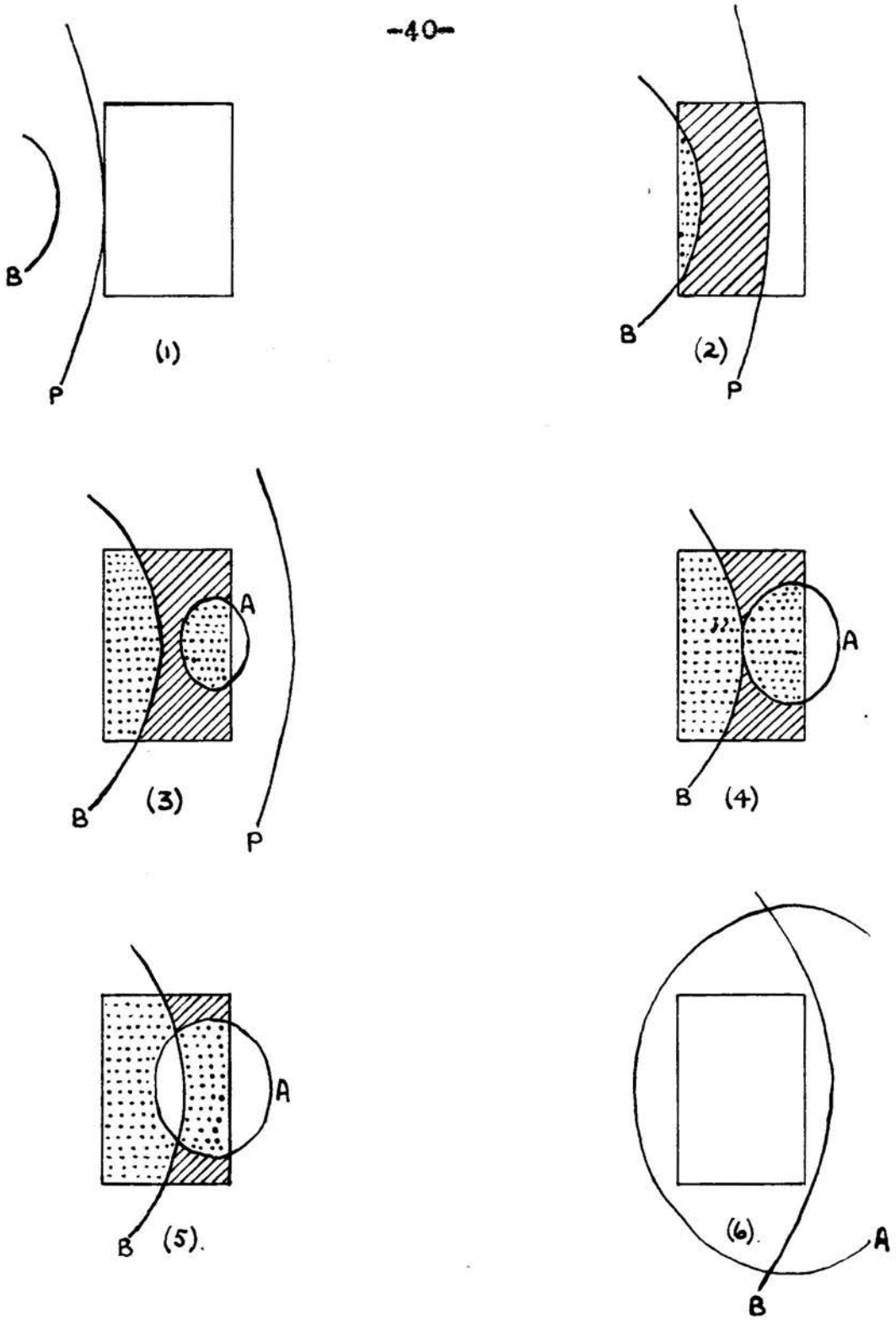

FIGURE 2·8. Typical source domains, when $\rho^2 > \frac{ad^2}{4s}$, for various image points (see text).
Not drawn to scale.

parabola.*

(3) From the right hand side of ellipse "A" to the parabola.*

§ 5.6 <u>The source domains which contribute to the intensity along the lines $y' = \pm c$ of the image.</u>

Only those domains which contribute to the intensity of image points along the X' axis have so far been discussed. To extend the discussion to points along the image lines $y' = \pm c$, where c is a constant, it is convenient to move the source a distance $\mp c$ along the η axis and again to consider boundaries of the source domains appropriate to points along the X' axis of the image.

Such a case is illustrated in § 8.

---

* If the parabola cuts the slit plane to the right of the slit, then the right hand side of ellipse "A" replaces the parabola in (2), and (3) does not contribute.

§ 6. Analytical expression for the intensity at an image point.

§ 6.1 General case.

The source domains which are capable of contributing at a single or double strength to the intensity of an image point have been established, and now the particular function which has to be integrated over these domains to give the intensity at the image point has to be found.

The argument differs from that of Li, in minor detail only.

Let n be the number of electrons leaving the source, per unit area of the source, per second. Of these electrons, a fraction $\frac{n.2s.2h}{4\pi d^2}$ pass through the slit and finally fall in the image space; 2s and 2h are the width and length of the source-slit respectively. It is assumed that the intensity of the beam is uniform over the slit, and this is true if $s \ll d$. Now

$$\frac{n.2s.2h}{4\pi d^2} = \frac{n}{4\pi d^2}\iint_{\text{Over slit.}} dx\,dy = \frac{n}{4\pi d^2}\iint_{\substack{\text{Over image}\\ \text{Space.}}} J\,dx'dy' \qquad (2.36)$$

When a detector slit is used in the image space, the length of this slit, rather than that of the source slit, defines in practice the limits of the y' co-ordinate, and then 2h, (which is always greater than the length of the source and/or the detector slit)

assumes an appropriately restricted value.

Using equations 2.15 and 2.17, the Jacobian J of equation 2.36 is found to be:-

$$J = -\frac{d^2}{\pi\rho\sqrt{2a}} \cdot \frac{1}{\sqrt{x'-\xi-\frac{2(y'-\eta)^2}{\pi^2 a}}} \qquad (2.37)$$

The negative sign comes from the root; this is because equation 2.15, when solved for $(x-\xi)$, is only satisfied when a negative sign is given to the radical.

Equation 2.36 shews that the number of electrons per unit area of the image space per second originating from each unit area of the source is $\frac{nJ}{4\pi d^2}$. Restricting the discussion to the line $y' = 0$ of the image, this becomes

$$-\frac{n}{4\pi^2\rho\sqrt{2a}} \cdot \frac{1}{\sqrt{x'-\xi-\frac{2\eta^2}{\pi^2 a}}} = K \text{ (say)}. \qquad (2.38)$$

The intensity at the point $(x',0)$ of the image plane is therefore obtained by integrating 2.38 over the whole source, and by applying weights of 0, 1, and 2 respectively to those domains contributing with zero, single and double strength. The intensity Φ at the image point $(x_1, 0)$ then becomes:-

$$\Phi = 2\underset{\text{Domain of double strength.}}{\iint} K\,d\xi\,d\eta + \underset{\text{Domain of Single strength.}}{\iint} K\,d\xi\,d\eta \qquad (2.39)$$

§ 6.2 Special case of the integral $\iint K\,d\xi\,d\eta$.

The integral $\iint K\,d\xi\,d\eta$ may be evaluated exactly only when the domain in the source is bounded on one side by a straight line, say $\xi = \xi'$, and on the other by the parabola as shewn in Figure 2.9.

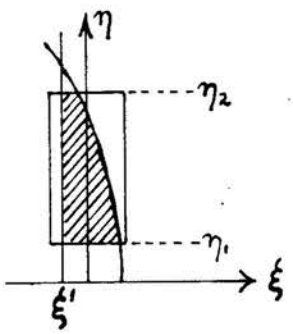

Figure 2.9.

In this special case, the integral assumes the form:-

$$I = \frac{n}{4\pi^2\rho\sqrt{2a}} \int_{\eta_1}^{\eta_2} \int_{\xi'}^{x' - \frac{2\eta^2}{\pi^2 a}} \frac{1}{\sqrt{x' - \xi - \frac{2\eta^2}{\pi^2 a}}}\, d\xi\, d\eta$$

$$= \frac{n}{2\pi^2\rho\sqrt{2a}} \int_{\eta_1}^{\eta_2} \sqrt{x' - \xi - \frac{2\eta^2}{\pi^2 a}}\, d\eta \qquad (2.40)$$

When

$$\left.\begin{aligned} v^2 &= x' - \xi' \\ p^2 &= \frac{2}{\pi^2 a} \\ H &= \frac{n}{4\pi^2\rho\sqrt{2a}} \end{aligned}\right\} \qquad (2.41)$$

the integral obtained becomes

$$I = \frac{Hv^2}{P}\left[\arcsin\frac{P\eta_2}{v} - \arcsin\frac{P\eta_1}{v} + \frac{P\eta_2}{v}\sqrt{1-\frac{P^2\eta_2^2}{v^2}} - \frac{P\eta_1}{v}\sqrt{1-\frac{P^2\eta_1^2}{v^2}}\right] \tag{2.42}$$

It is convenient, for numerical work, to set the lower limit of integration of η equal to zero. Hence with $\eta_1 = 0$ and $\eta_2 = \eta$, equation 2.42 becomes

$$I = \frac{Hv^2}{P}\left[\arcsin\frac{P\eta}{v} + \frac{P\eta}{v}\sqrt{1-\frac{P^2\eta^2}{v^2}}\right] \tag{2.43}$$

which may now be written as $F(v,\eta)$.

Equation 2.42 then takes the form

$$I = F(v,\eta_2) - F(v,\eta_1) \tag{2.44}$$

It has been presumed that the integrand of equation 2.40 remains real at the upper limit of integration. This will not be the case if the line $\xi = \xi'$ cuts the parabola within the source as shewn in Figure 2.10.

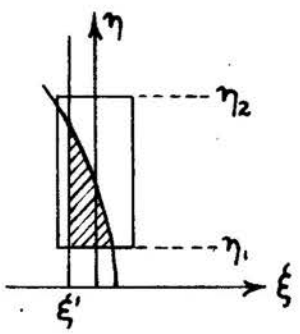

FIGURE 2·10

In such a case equation 2.40 must be replaced by:-

$$I = 2H \int_{\eta_1}^{v/\rho} \sqrt{v^2 - \rho^2\eta^2}\, d\eta$$

$$= F(v, v/\rho) - F(v, \eta_1) \qquad (2.45)$$

where $F(v, v/\rho)$ reduces to $\frac{Hv^2}{\rho} \cdot \frac{\pi}{2}$.

§ 6.3 Method for evaluating $\iint K\, d\xi\, d\eta$ in the general case.

The domain of integration does not usually extend from a straight line to a parabola. In all cases however, the correct domain may be obtained by appropriate sums or differences of integrals extending from suitably chosen straight lines, or from one or both of the ellipses, to the parabola, an appropriate choice for the limits for η being made for the various integrals. Examples of such cases are given in § 8.

It remains therefore to establish a method for integrating K over a region extending from an ellipse to the parabola. The integration with respect to ξ may be performed analytically, but an approximate method is required to integrate with respect to η . Simpson's Rule is suitable for this numerical integration, since it is accurate for functions with constant third differences, and the integrand here, in all cases, possesses almost constant second differences. The evaluation of three ordinates only is required to give

accuracy to four significant figures.

To find the new value of ξ to replace the constant value ξ' (used when integrating from the straight line $\xi = \xi'$) either equation 2.23 or 2.29 is solved for ξ , according to whether integration to the parabola is required from ellipse "A" or ellipse "B".

Substituting this ξ in place of ξ' into equation 2.40 gives, for integration from ellipse "A",

$$\bar{I} = 2H \int_{\eta_1}^{\eta_2} \sqrt{x' + \frac{Q^2}{2P^2} - s - P^2\eta^2 \mp (a_A^2 - Q^2\eta^2)^{1/2}}\, d\eta \qquad (2.46)$$

in which:

$$P^2 = \frac{2}{\pi^2 a}$$

$$Q = \frac{d}{\pi \rho}$$

$$H = \frac{n}{4\pi^2 \rho \sqrt{2a}}$$

and a_A is given by equation 2.25.

The negative and positive signs to the root of $a_A^2 - Q^2\eta^2$ apply to integrations from the right hand edge and the left hand edge of the ellipse respectively.

Equation 2.46 may, for ease of reference, be contr acted to

$$\left.\begin{aligned} \bar{I} &= \int_{\eta_1}^{\eta_2} A_R\, d\eta \\ \text{or} \\ \bar{I} &= \int_{\eta_1}^{\eta_2} A_L\, d\eta \end{aligned}\right\} \qquad (2.47)$$

"B" replaces "A" for integration from ellipse "B" to the parabola.

§ 7. Tilted sources.

Only the case in which the source lies in the source plane has so far been considered. It will be shewn in § 10.4 that it is desirable to use a source which is as narrow as possible, (consistent with the source being sufficiently thin), in order to achieve high resolution. In the preparation of sources of $MsTh_2$ a minimum width of 2 mm. is set by practical limitations. In order to reduce the effective width of the source, it may be tilted to an emission angle, α, as shewn in Figure 2.11. The exact effect of

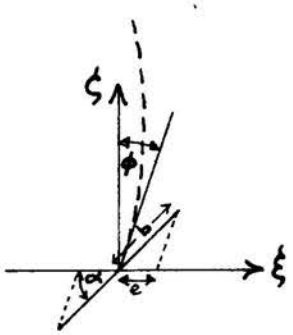

Figure 2.11

such tilting on the line shape is complicated by the variation of the source to source-slit distance, d, as the source is scanned. It was considered that a

sufficiently good approximation to the line shape would however be given by projecting all points of the tilted source on to the (ξ , η) plane, the projection being in the direction of the tangent at the source to that trajectory from the centre of the source which passes through the centre of the source slit.

Let b = actual half width of the source.

e = effective " " " " "

α = emission angle.

ϕ = azimuth of the electron trajectory from the centre of the source, through the centre of the source slit.

Figure 2.11 shews that:-

$$e = b(\cos\alpha - \sin\alpha \tan\phi)$$

Substituting $\tan\phi = \frac{d}{a}$ (which is obtained from Figure 2.2) the effective width of a tilted source becomes:-

$$e = b\left(\cos\alpha - \frac{d}{a}\sin\alpha\right) \qquad (2.48)$$

Tilted sources of width $2b$ may then be regarded as equivalent to sources of width $2e$ lying in the (ξ , η) plane, and of intensity:-

$$\frac{nb}{e} \qquad (2.49)$$

where n is the number of electrons leaving the actual source per cm.^{2} per second.

Equation 2.48 shews that the effective width of a tilted source increases with the radius of

curvature of the electron trajectories.

§ 8. Example of the method for obtaining the shape of a β-ray line.

To clarify the method for calculating the line shape, (which is similar to that adopted by Feather, Kyles and Pringle[2] for the same purpose) a specific example will be considered, in which the values of the various parameters are as follows:-

(1) Source. Width 2 mm.; length 1 cm. Set at an emission angle of 45° and placed symmetrically about the origin of source co-ordinates. The effective half-width of the source then becomes, by equation 2.48, 0.04284 cm.

(2) Source slit. Width 4 mm.; length greater than that of the source and of the counter slit.

(3) Radius of curvature. ρ = 3 cm.

(4) Source to source slit distance d = 2.2 cm.

(5) Counter slit. Length 1.5 cm. Width 0.8 mm.

The intensity at points along the X' axis of the image is evaluated at intervals of x' of 0.01 cm.

This is repeated for points along the image lines y' = 0.5 cm., and y' = 0.75 cm. by off-setting the source as discussed in § 5.7. The counter slit (the effect of which will be discussed later) is of length 1.5 cm., so that the image points beyond y' =

0.75 cm. do not contribute to the final intensity.

The various distinct types of domain in the source encountered when, for example, $y' = 0.75$ cm. and the corresponding expression for evaluating the intensity Φ at the image point are shewn in the diagrams of Figure 2.12.

The notation set out below has been adopted.

The source extends from e^- to e^+ in the ξ direction and from η_1 to η_2 in the η direction.

$F(v,\eta)$ and $F(v,\frac{v}{p})$ have the meanings indicated by equations 2.43 and 2.45 and $\int_{\eta_1}^{\eta_2} A_R\, d\eta$ and $\int_{\eta_1}^{\eta_2} B_R\, d\eta$ are explained by equations 2.46 and 2.47. The letters P, A, and B against the curves refer to the parabola, and the ellipses "A" and "B" respectively.

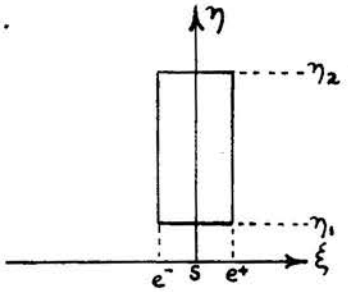

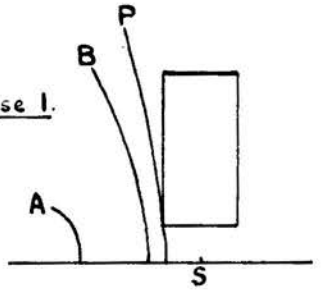

Case 1.

$$\Phi = 0$$

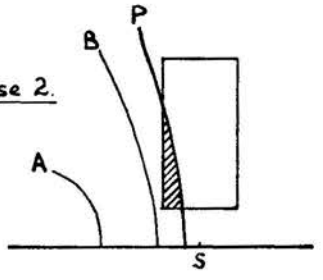

Case 2.

$$\Phi = 2\left[F\left(v, \tfrac{v}{p}\right) - F(v, \eta_1)\right]$$

$$\left(v^2 = x' - e^-\right).$$

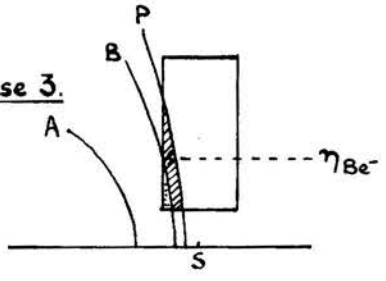

Case 3.

$$\left.\begin{aligned}\Phi = 2F\left(v, \tfrac{v}{p}\right) - F(v, \eta_{Be^-}) - F(v, \eta_1) \\ + \int_{\eta_1}^{\eta_{Be^-}} B_R \, d\eta.\end{aligned}\right\}$$

$$\left(v^2 = x' - e^-\right).$$

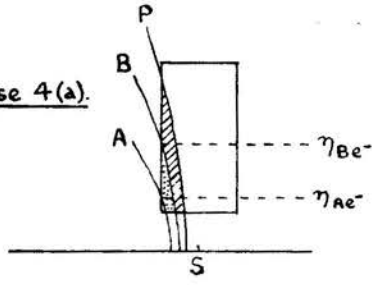

Case 4(a).

$$\left.\begin{aligned}\Phi = 2F\left(v, \tfrac{v}{p}\right) - F(v, \eta_{Be^-}) - F(v, \eta_{Ae^-}) \\ + \int_{\eta_1}^{\eta_{Be^-}} B_R \, d\eta \;+ \int_{\eta_1}^{\eta_{Ae^-}} A_R \, d\eta.\end{aligned}\right\}$$

$$\left(v^2 = x' - e^-\right).$$

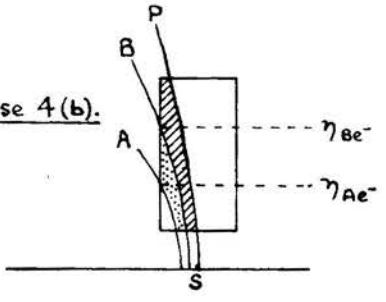

Case 4(b).

$$\left.\begin{aligned}\Phi = 2F(v, \eta_2) - F(v, \eta_{Be^-}) - F(v, \eta_{Ae^-}) \\ + \int_{\eta_1}^{\eta_{Be^-}} B_R \, d\eta \;+ \int_{\eta_1}^{\eta_{Ae^-}} A_R \, d\eta.\end{aligned}\right\}$$

$$\left(v^2 = x' - e^-\right).$$

FIGURE 2·12
(See text).

Continued.

Case 5.

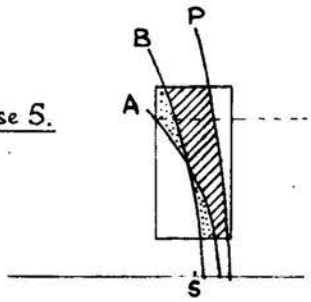

$$\Phi = F(v,\eta_2) - F(v,\eta_{Ae^-}) + \int_{\eta_1}^{\eta_2} B_R\,d\eta + \int_{\eta_1}^{\eta_{Ae^-}} A_R\,d\eta$$

$(v^2 = x' - e^-)$

Case 6.

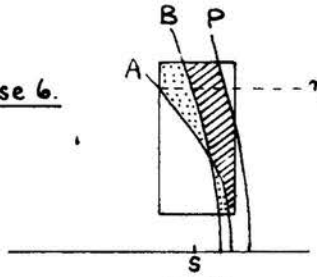

$$\Phi = F(v_1,\eta_2) - F(v_1,\eta_{Ae^-}) + \int_{\eta_1}^{\eta_2} B_R\,d\eta + \int_{\eta_1}^{\eta_{Ae^-}} A_R\,d\eta - 2F\left(v_2,\frac{v_2}{P}\right) + 2F(v_2,\eta_1)$$

$(v_1^2 = x' - e^- \quad ; \quad v_2^2 = x' - e^+)$.

Case 7.

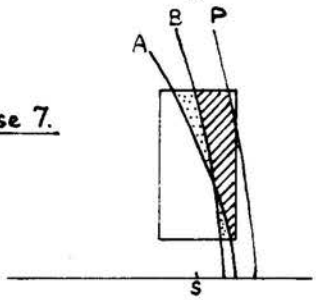

$$\Phi = \int_{\eta_1}^{\eta_2} A_R\,d\eta + \int_{\eta_1}^{\eta_2} B_R\,d\eta - 2F\left(v,\frac{v}{P}\right) + 2F(v,\eta_1)$$

$(v^2 = x' - e^+)$.

Case 8.

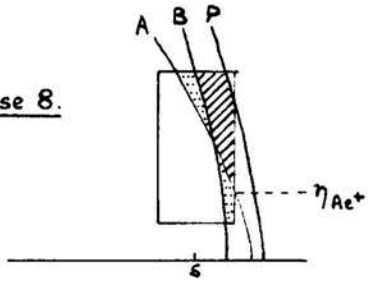

$$\Phi = \int_{\eta_{Ae^+}}^{\eta_2} A_R\,d\eta + \int_{\eta_1}^{\eta_2} B_R\,d\eta - 2F\left(v,\frac{v}{P}\right) + F(v,\eta_{Ae^+}) + F(v,\eta_1).$$

$(v^2 = x' - e^+)$.

Case 9.

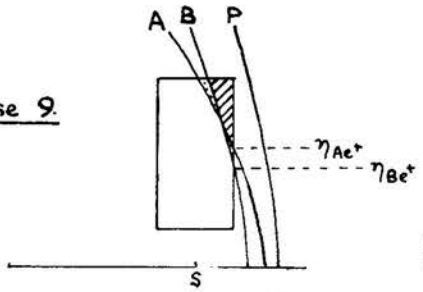

$$\Phi = \int_{\eta_{Ae^+}}^{\eta_2} A_R\,d\eta + \int_{\eta_{Be^+}}^{\eta_2} B_R\,d\eta - 2F(v,\eta_2) + F(v,\eta_{Ae^+}) + F(v,\eta_{Be^+}).$$

$(v^2 = x' - e^+)$.

Case 10.

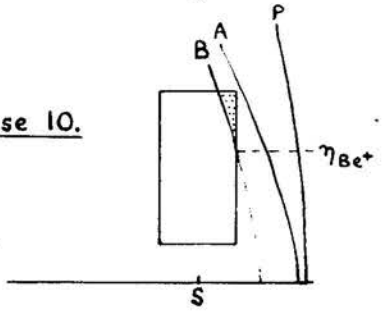

$$\Phi = \int_{\eta_{Be^+}}^{\eta_2} B_R\,d\eta - F(v,\eta_2) + F(v,\eta_{Be^+}).$$

$(v^2 = x' - e^+)$.

FIGURE 2·12.
(See text).

It is essential to recognize which of the above cases is applicable to the particular value of x', the image co-ordinate, under consideration, and to decide this the positions of the parabola and the two ellipses relative to the source are required.

Taking the parabola first, if

(i) $x' - e^- < \frac{2\eta_1^2}{\pi^2 a}$, the parabola does not yet enter the source.

(ii) $\frac{2\eta_2^2}{\pi^2 a} > x' - e^- > \frac{2\eta_1^2}{\pi^2 a}$, the parabola cuts the left hand edge of the source (vide cases 2, 3, and 4(a)).

(iii) $x' - e^+ < \frac{2\eta_1^2}{\pi^2 a}$, the parabola does not yet cut the right hand edge of the source (vide cases 4(b) and 5).

(iv) $\frac{2\eta_2^2}{\pi^2 a} > x' - e^+ > \frac{2\eta_1^2}{\pi^2 a}$, the parabola cuts the right hand edge of the source between η_1 and η_2 (vide cases 6, 7, and 8).

(v) $x' - e^+ > \frac{2\eta_2^2}{\pi^2 a}$, the parabola has left the source altogether (vide cases 9 and 10).

Turning now to the "A" ellipse, equation 2.25 is solved for η^2 , when $\xi = e^-$, giving:-

$$\eta_{Ae^-}^2 = \frac{1}{P^2}(x' - e^-) - \frac{1}{Q^2}(s - e^-)^2$$

where $P^2 = \frac{2}{\pi^2 a}$ and $Q = \frac{d}{\pi P}$ as before. A table may then be constructed of $\eta_{Ae^-}^2$ for the various values of x' employed; the entries, having constant

first differences for equal intervals of the argument, are easily evaluated.*

The following cases then arise:-

(i) $\eta_1^2 > \eta_{Ae^-}^2$ The ellipse has not yet entered the source (vide cases 2 and 3).

(ii) $\eta_1^2 < \eta_{Ae^-}^2 < \eta_2^2$ The ellipse cuts the left hand edge of the source (vide cases 4(a) and (b), 5 and 6).

(iii) $\eta_{Ae^-}^2 > \eta_2^2$ The ellipse no longer cuts the left hand edge of the source.

In a similar way the tables for $\eta_{Ae^+}^2$, $\eta_{Be^-}^2$ and $\eta_{Be^+}^2$ may be constructed to determine

(i) whether or not the A ellipse cuts the right hand edge of the source,

(ii) whether or not the B ellipse cuts the left hand edge of the source,

(iii) whether or not the B ellipse cuts the right hand edge of the source,

respectively.

---

* The table need not give entries for $\eta_{Ae^-}^2 < \eta_1^2$ or $> \eta_2^2$. The actual values of the intermediate entries are used in the integrations, and so it is more convenient to complete these entries than simply to calculate the range of x' for which $\eta_1^2 < \eta_{Ae^-}^2 < \eta_2^2$.

It is not necessary to know whether the ellipses intersect within the source, because their intersection does not alter the expressions for the intensity Φ .

The particular form of the domain of integration having been recognized, the intensity Φ may be evaluated using the appropriate expression indicated against that domain in Figure 2.12.

The results giving the intensity Φ * along the line $y' = 0.75$ cm. of the image are plotted in Figure 2.13. The calculations for the image lines $y' = 0$ and $y' = 0.5$ cm. may be performed in a similar way and the results are shewn on the same diagram.

The physical interpretation of these curves is that, if an ideal photographic plate were placed in the image space, Φ would be proportional to the blackening of the plate at the various points considered.

From the curves of Figure 2.13, the variation in intensity Φ with y' at each value of x' used may be plotted, as shewn in Figure 2.14. These curves are symmetrical about the line $y' = 0$; therefore only one half is plotted.

---

* Φ is the number of electrons per cm.^{2} of the image arriving per second at the point (x',y') from the whole source which emits a single electron per cm.^{2} per second.

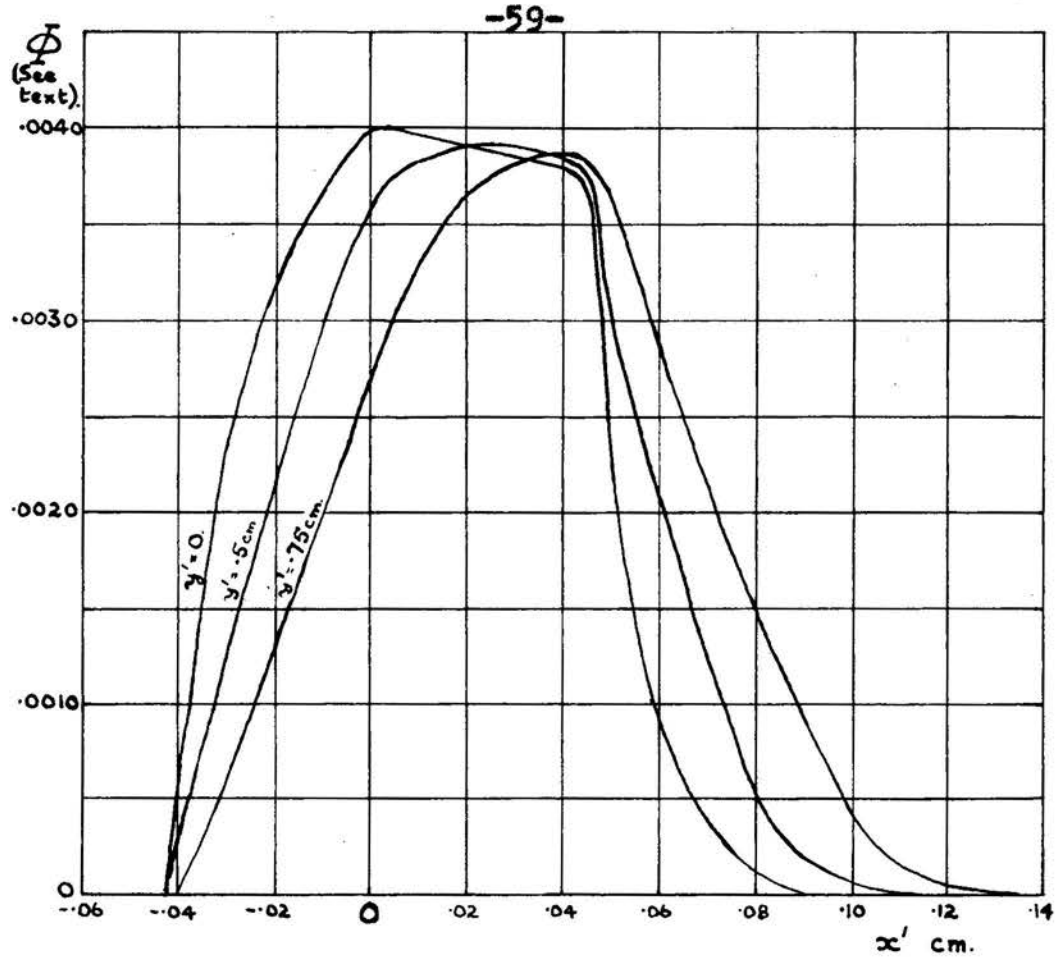

FIGURE 2·13. (See text).

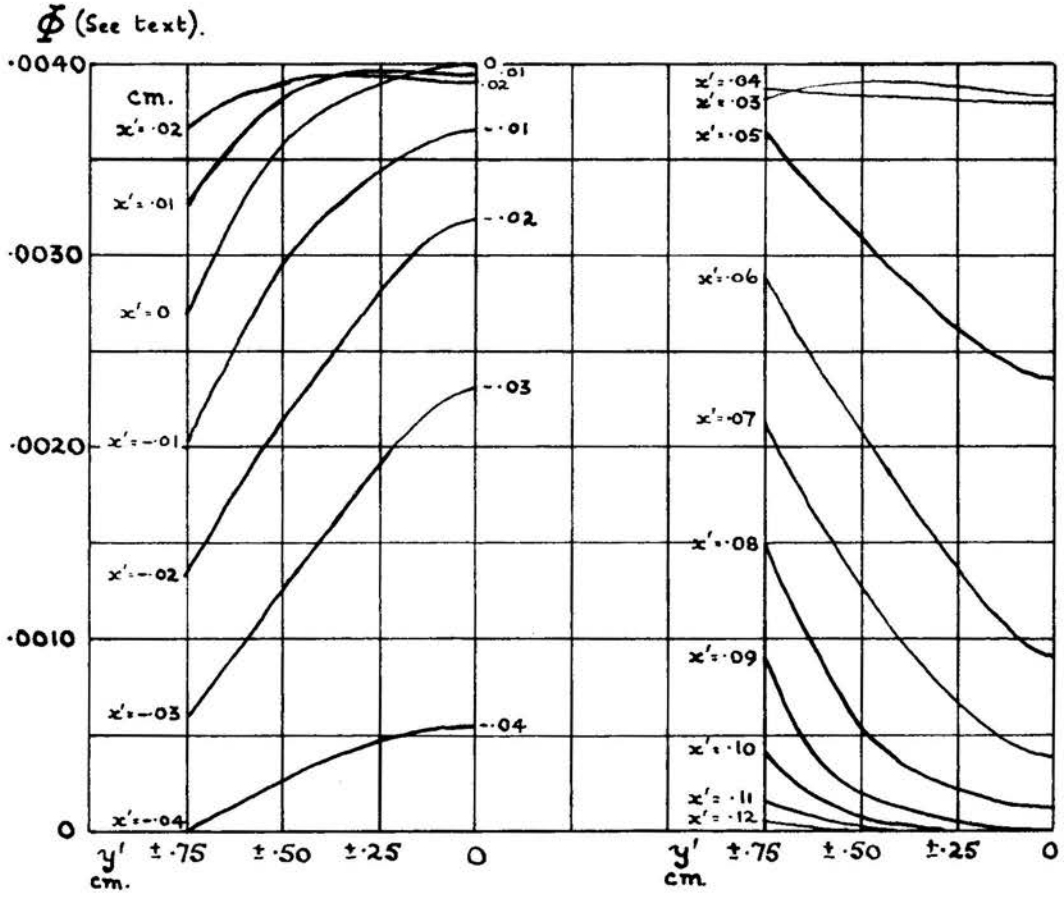

FIGURE 2·14 (See text).

If one of these curves is integrated with respect to y', between the limits $+\ell$ and $-\ell$ (where 2ℓ is the length of the counter window), the intensity over a narrow strip of width dx' and length 2ℓ, for a fixed value of x', is obtained. This is, in effect, the solid angle Ω', expressed as a fraction of 4π, subtended by the narrow strip $2\ell dx$ at the source, for electrons of momentum p where $\rho = \frac{pc}{He}$ (ρ being the radius of the trajectory from the centre of the source through the centre of the source slit). The variation of this solid angle with x' is shewn in Figure 2.15. (This curve would be expected if the blackening of a photographic plate, as observed through a very narrow slit of length 2ℓ, were plotted against the position of the slit).

An adaptation of Hardy's "37" numerical integration formula may be used for this integration. Denoting the calculated ordinates by u_o, $u_{0.5}$ and $u_{0.75}$, the formula becomes

$$\int_{-0.75}^{+0.75} u_x dx = 0.55\,u_o + 0.81\,u_{0.5} + 0.14\,u_{0.75}$$

where the counter slit is of length 1.5 cm.

If the width of the counter slit is 2w, the solid angle subtended by the entire window at the source (the transmission factor T(x')) when the centre of the window is at x', may now be obtained by integrating the curve of Figure 2.15 between the limits

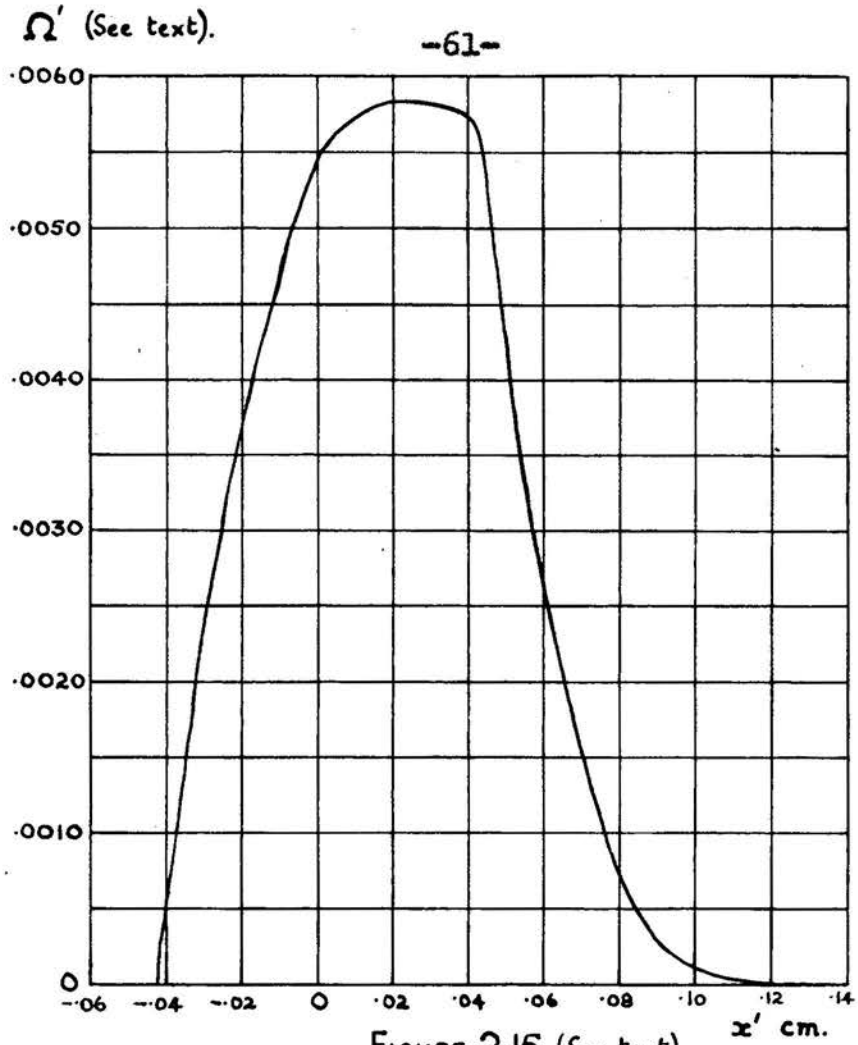

FIGURE 2·15. (See text).

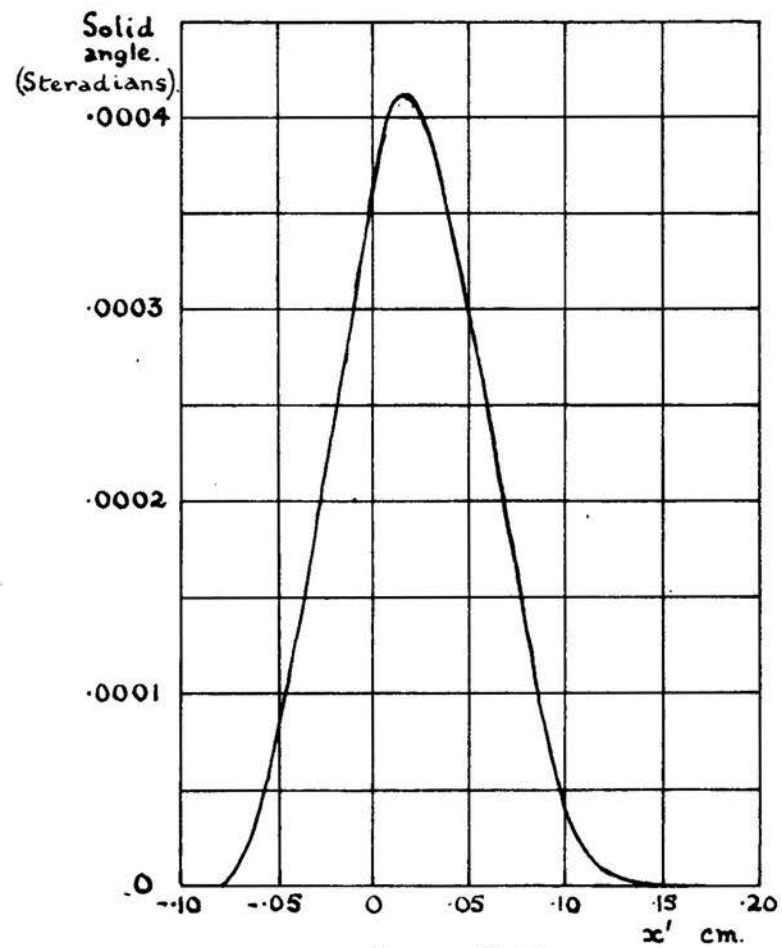

FIGURE 2·16

$x' + w$ and $x' - w$. The results of this integration (performed by counting squares) is shewn in Figure 2.16 for a counter slit of width .8 mm. which is the width of the curve of Figure 2.15 at half the maximum height. Figure 2.16 then shews the variation of the transmission factor with x', or in other words, the variation of the counting rate for electrons of momentum p as the counter slit is moved in the plane of focusing in a constant magnetic field. This is then the shape of a β -ray line of momentum $p = \frac{He\rho}{c}$.

The solid angle, for the particular conditions of this example, is 4.1×10^{-4} of 4π; the resolving power, defined as $\frac{H\rho}{\delta(H\rho)}$, where $\delta(H\rho)$ is the change in the $H\rho$ value corresponding to the width of a β -ray line at half the maximum height, is $\frac{\rho}{\delta\rho}$ for a constant field spectrometer, and is 72 in the case chosen.

The "representative" ρ value of a β -ray line is obtained when $x' = 0$.

Feather, Kyles and Pringle[2] have calculated the line shape for broader slits and a larger radius of curvature, by a similar method, and have shewn that the analytical line shape agrees well with that found experimentally.

§9. An Approximate Method for Finding Line Shapes.

The arithmetical work involved in the calculation of the shape of a β-ray line by the method outlined in § 8 is lengthy, and for many purposes a less exact but more rapid method is desirable. The effect on both solid angle and resolving power of variations in the spectrometer geometry at various radii may then be assessed.

The change in shape of a single member of the family of curves of figure 2.13 is sufficient to indicate the effect on solid angle and resolution produced by such a change in geometry.

To reduce the arithmetical work the following simplifications will be made.

(1) It will be assumed that the function K (which when integrated over the appropriate domains of the source, suitably weighted, gives the intensity at the image point x' chosen) remains sensibly constant over all source domains.

(2) The curvature of the ellipses and the parabola in the source will be neglected.

The first assumption implies that the intensity at an image point x' is now determined simply by the area of the domains of the sources, suitably weighted. The second assumption means that, since the source is rectangular in shape, the area of the domains

is proportional to the distance between the straight lines in the source which now replace the parabola and the ellipses.

As an example, let the curve of figure 2.13 for $y' = 0$ now be obtained, making these assumptions.

Plotting ξ against x', a diagram as shewn in figure 2.17(a) is given.

The lines $\xi = \pm e$ indicate the extent of the source.

The movement of the apex of the parabola through the source, resulting from motion of the point x' in the image, is obtained by setting $\eta = 0$ in equation 2.30 giving

$$x' = \xi. \qquad (2.50)$$

This line is marked as PP'.

The movement of the extremity of the minor axis of ellipse A is given similarly by putting $\eta = 0$ in equation 2.23 which becomes:-

$$x' - \xi = \frac{2\rho^2}{ad^2}(s - \xi)^2. \qquad (2.51)$$

On the (x', ξ) diagram this is a parabola.

The B ellipse gives a second parabola intersecting the first on the x' axis at $x' = \frac{2\rho^2 s^2}{ad^2}$.

These parabolae are marked AA' and BB' respectively. Their curvature is small, and they may be replaced by straight lines.

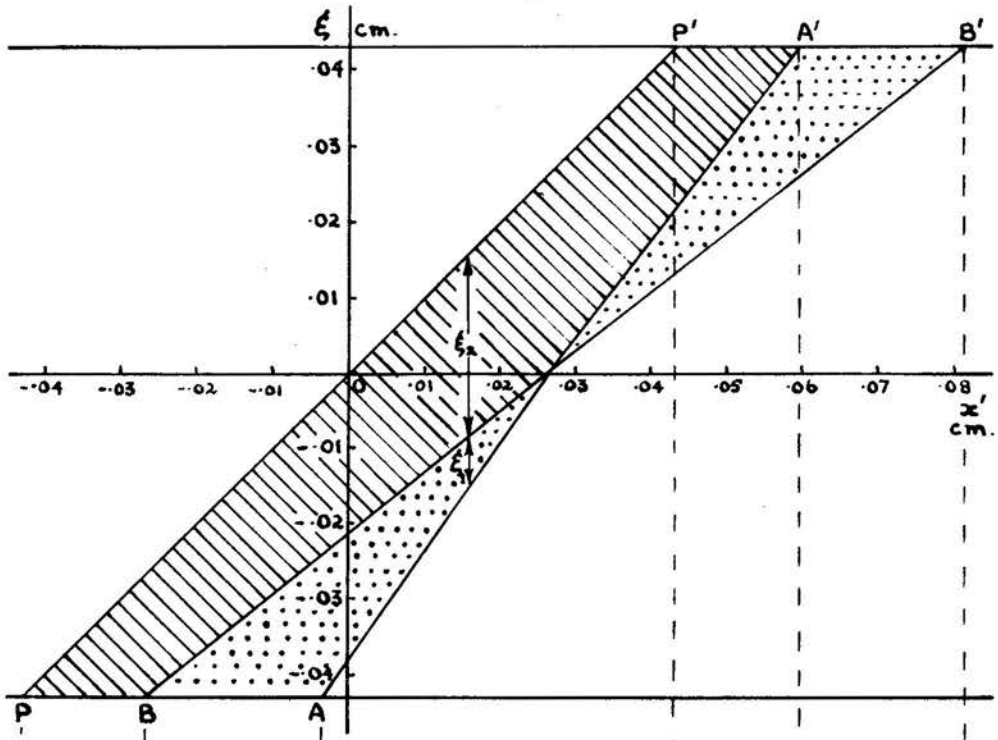

FIGURE 2·17(a).

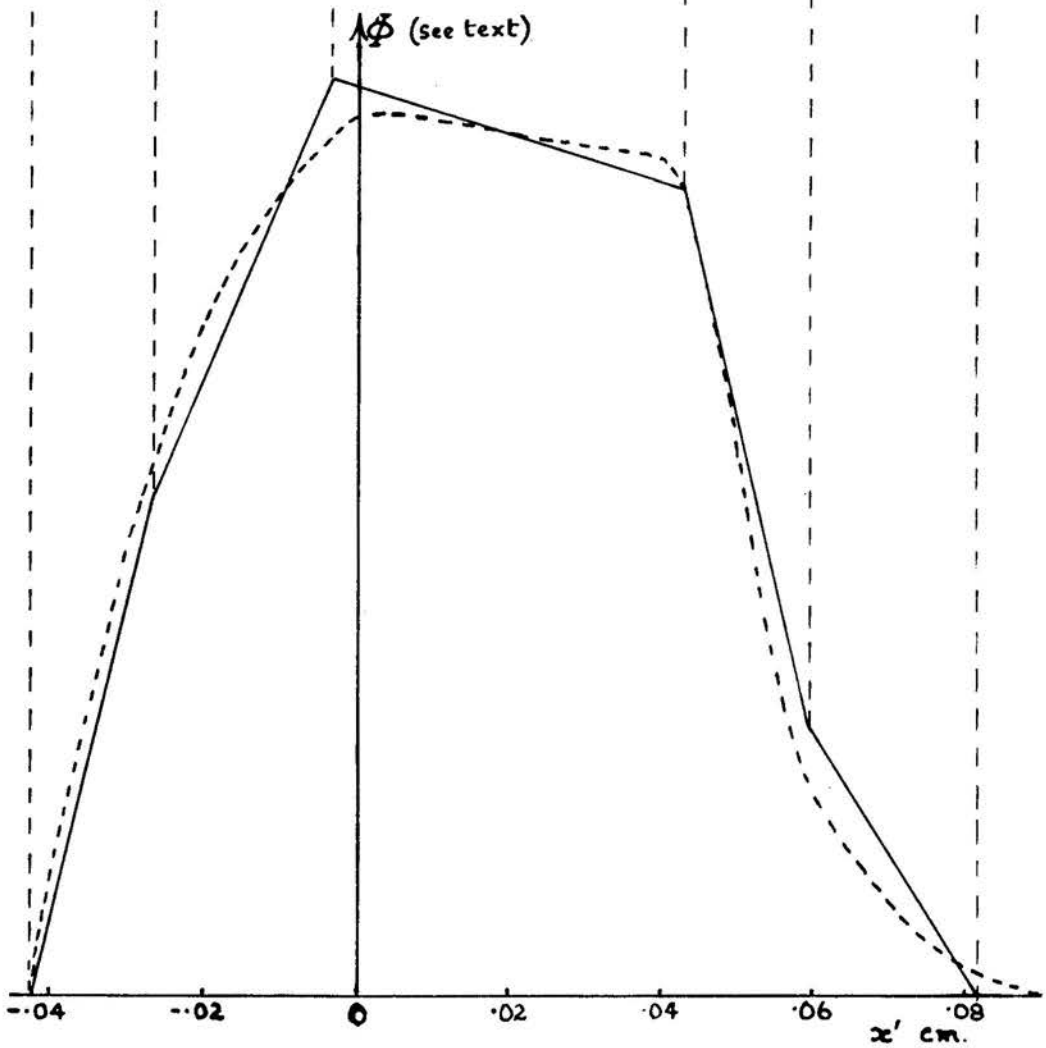

FIGURE 2·17(b).

From this diagram the desired variation in intensity with x' may be obtained immediately. The shading indicates the regions of double and of single weight. Hence the intensity at the point x', say, is given by $(\xi_1 + 2\xi_2)$.

Figure 2.17(b) shews the approximate variation in intensity with x' obtained this way. The corresponding curve of figure 2.13 obtained from the more detailed analysis is shewn for comparison (by a broken line). The more exact curve has been normalized to the height of the approximate curve. The agreement between the two is satisfactory, shewing that the approximations are justified.

The approximate method gives an absolute value for the spread of intensity along the X' axis but the intensity is not given absolutely. Relative intensities at various radii may, however, be obtained approximately by multiplying the ordinates by $\frac{1}{e\rho}$ where e is the effective width of the source. Equation 2.40 explains the introduction of the factor $\frac{1}{\rho}$ * and the factor $\frac{1}{e}$ is explained by equation 2.49.

* Alternatively this factor may be explained by the variation of the solid angle subtended at a point source with $1/\rho$ or with $1/a$, since a/ρ is nearly constant for small values of d, (cf. § 10.1).

§ 10. General remarks on the dependence of the line profile on the spectrometer design.

§10.1 Variation of the solid angle and resolution with ρ

It is pointed out by Feather[1] that, to a first approximation, the solid angle subtended at a point source by the counter slit is given by $\frac{2sl}{R^2 ad}$. Since ρ increases with a, the solid angle diminishes as ρ increases. A more detailed investigation of the dependence of the solid angle upon the width of the source slit will be made in § 10.2, in which extended sources are considered.

The resolving power, defined for a constant field spectrometer as $\frac{\rho}{\Delta\rho}$ (cf. § 8) will, on the other hand, increase with ρ.

§ 10.2 The dependence of the resolution and solid angle on the width of the source slit.

It is clear from figure 2.17 that, for the particular width of source slit employed, the whole source is not occupied by a domain of double weight for any image point. This condition is characterized by the flat top to the curve shewing the intensity at various image points along the X' axis which is caused by the movement, through a relatively broad source, of a narrow domain of double weight. An immediate improvement in the solid angle could therefore be effected by increasing the source slit width to make the x' coordinate of B (which is denoted by x'_B) coincide with

that of P' (denoted by $x'_{p'}$). The source slit width, given by solving equation 2.29 for s, with $\eta = 0$, $x' = e$ (the effective half-width of the source) and $\xi = -e$ is:-

$$s = \frac{d}{\rho}\sqrt{ae} + e$$

The whole source would then contribute doubly to the image point $x'_{p'}$.

If the diagram corresponding to figure 2.17 were drawn for a radius of curvature of 6 cm. (which is the maximum radius focused), using this increased source slit width, and bearing in mind that the effective width of tilted sources increases with ρ , it would be found that $x'_B \gg x'_P$. The intensity curve, although indicating a large solid angle, will again possess a flat top, which is due now to the movement of a broad domain of double weight across a relatively narrow source. This results in a loss of resolution at larger radii with no compensating improvement in solid angle.

Such a loss in resolution would be avoided by reducing the slit width to make $x'_B = x'_P$ at $\rho = 6$ cm. This would then cause $x'_B < x'_P < x'_A$ at $\rho = 3$ cm., indicating a small reduction in solid angle, which is compensated by an increase in resolving power. This is advantageous, since the solid angle at small radii is greater than at large radii, whereas the resolution is

lower.

Any further increase in resolution, by reduction of the source slit width, is accompanied by a loss in solid angle.

§ 10.3 <u>The dependence of the resolution and the solid angle on the position of the source, and on the width of the counter slit.</u>

To investigate the manner in which resolution and solid angle depend on the source position, the curves of figure 2.18(b) are plotted by the approximate method. The radius of curvature chosen is 6 cm.; curves N, C and F refer to sources of width 2 mm. set at an emission angle of 45°, which are displaced in the plane of the cource respectively nearer to the image by half the effective width, centrally, and farther from the image by half the effective source width. In each case the source slit width is calculated so that a domain of double weight just occupies the whole source, in order to obtain the largest solid angle without loss of resolution at this radius. Thus, for source position "N", equation 2.29 is solved for s, with $x' = 0$, $\xi = -2e$ and $\eta = 0$. This gives

$$s = \frac{d}{\rho}\sqrt{ae} + 2e \qquad (2.52)$$

For the central source position, $x' = e$, $\xi = -e$, and $\eta = 0$ to give:-

$$s = \frac{d}{\rho}\sqrt{ae} + e \qquad (2.53)$$

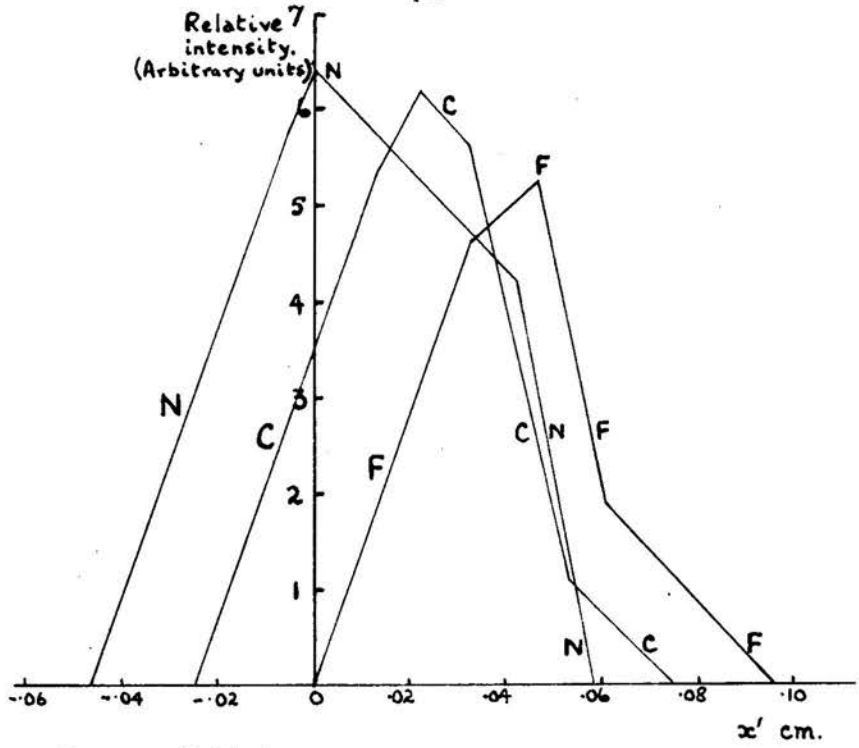

FIGURE 2·18 (a). Approximate variation in intensity when $y' = 0$ for different source positions. $\rho = 3$ cm. (See text).

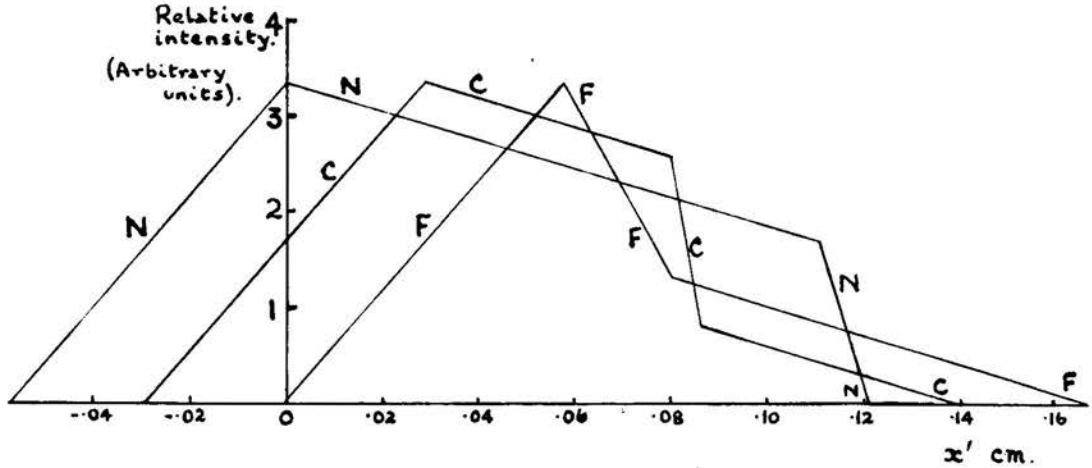

FIGURE 2·18 (b). Approximate variation in intensity when $y' = 0$ for different source positions. $\rho = 6$ cm. (See text).

For source position "F", $x' = 2e$, $\xi = 0$ and $\eta = 0$, and s is given by:-

$$s = \frac{d}{\rho}\sqrt{ae} \qquad (2.54)$$

It is assumed that off-setting the source does not significantly alter $2e$, the effective source width.

The curves of figure 2.18(a) shew the intensities along the X' axis of the image in these three cases, when the radius of curvature is reduced to 3 cm. The ordinates are normalized to give the correct heights relative to the curves at $\rho = 6$ cm., as discussed in § 9.

Neglecting any further spreading due to similar curves relating to the intensities along image lines parallel to the X' axis, an idea of the line shape would be given by scanning each of these curves with a counter slit. Taking the 6 cm. cases, and choosing a counter slit of width equal to that of each curve, in turn, at half the maximum height, it is clear that the case N will produce a line shape possessing the largest solid angle but with the smallest resolution. Case F, on the other hand, gives a high degree of resolution, but the solid angle is smaller; moreover this line shape possesses an undesirable "tail" on the low energy side. Case C possesses intermediate features.

Turning now to the smaller radius a difficulty becomes apparent. The optimum counter slit width is,

in all cases, smaller than the corresponding value at 6 cm., but the ratio of the optimum width at 6 cm. to that at 3 cm. is ~ 1.22 for source position F as against ~ 1.80 for position C and ~ 2.03 for N.

For experiments in which both a large solid angle and the best resolution are essential, the counter slit width appropriate to the particular radius at which the line is focused may be chosen.

For experiments in which a fixed width of counter slit is required a compromise between solid angle and resolution is necessary.

The effect of the choice of counter slit width on the ratio of the height of a β-ray line to that of the background will be discussed in § 12.

§ 10.4 <u>The effect of the source size and of the length of the counter slit on solid angle and resolution.</u>

In considering the most suitable choice of source size the thickness of the source has always to be borne in mind.

For narrow sources, a narrow source slit is sufficient to allow a domain of double weight completely to occupy the source. This in turn implies that a relatively small movement of the image point is sufficient to move the domain of double weight off the source. A narrow counter slit may then be used and high resolution is obtained. The solid angle, however, is correspondingly

small.

Treated analytically, the total spread of intensity for electrons of momentum p in the image plane, may be obtained as follows.

The source (which is assumed to be placed centrally) will begin to contribute to the image intensity at the point x_1', for which the parabola enters the left hand edge. From equation 2.31 it is found that:-

$$x_1' = -e$$

Provided $\rho^2 < \frac{ad^2}{4s}$ (cf. § 5.5) the source will cease to contribute when the B ellipse leaves; the image point x_2' in this case is given by equation 2.29, and is

$$x_2' = e + \frac{2(\ell+k)^2}{\pi^2 a} + \frac{2\rho^2}{ad^2}(s+e)^2$$

in which:-

2ℓ is the length of the counter window

and $2k$ is the length of the source.

Putting into this equation the value of s, the half width of the source slit, for which the source just doubly contributes, given by equation 2.53, the total spread of curves similar to that of Figure 2.16 becomes:-

$$x_2' - x_1' = 8\left\{\frac{e}{2} + \frac{\rho e}{d}\sqrt{\frac{e}{a}} + \frac{\rho^2 e^2}{ad^2} + \frac{(\ell+k)^2}{4\pi^2 a}\right\} + 2w \qquad (2.55)$$

in which the term 2w (which is the width of the counter

window) accounts for a further increase in spread.

For sources off-set from the central position, equation 2.55 remains unaltered, save for the variation in the term $2w$ discussed in § 10.3, provided that the appropriately modified value for s, given by equation 2.52 or 2.54, is used.

It is clear that narrow sources reduce the image spread very considerably.

The resolution will also be increased, but only by a small amount, by reducing 2ℓ , the length of the counter window. Such a reduction however causes an almost proportionate reduction in solid angle (cf. § 10.1) so that in actual fact the counter window is always made as long as possible.

For high resolution, equation 2.55 shews that the source should be made short, (consistent with it being sufficiently strong and thin) but this again is of secondary importance to keeping the source narrow.

§ 10.5 <u>The effect of variation of the distance, d, between the source and the source slit.</u>

The image spread $(x_2' - x_1')$, of equation 2.55 may be written as Δa , where a is given by:-

$$4\rho^2 = a^2 + d^2$$

Using this equation, the resolving power may be written as:-

$$\frac{\rho}{\Delta\rho} = \frac{4\rho^2}{\sqrt{4\rho^2 - d^2}\,.\,f.\,\Delta a.} \qquad (2.56)$$

for a given value of d, in which the fraction f relates the image spread at half its maximum height to the total image spread, $\Delta\alpha$.

Examination of equation 2.55 shews that $\Delta\alpha$ is reduced by increasing d. A further small increase in resolution is produced by increasing d, since $\frac{4\rho^2}{\sqrt{4\rho^2-d^2}}$ increases with d.

To a first approximation, the solid angle is proportional to $\frac{s}{d}$ (cf. § 10.1). For sources displaced from the central position towards the image by half their effective width, s is given by equation 2.52 and:-

$$\frac{s}{d} = \frac{1}{\rho}\left\{e\sqrt{4\rho^2-d^2}\right\}^{1/2} + \frac{2e}{d} \qquad (2.57)$$

The first term decreases slowly as d increases and the second term causes a further reduction in $\frac{s}{d}$. The effect of this second term diminishes as the source is moved in the source plane away from the image, and it becomes zero under the conditions of equation 2.54.

The reduction in solid angle, as d increases, is therefore smallest for sources displaced by half their effective width from the central position to the side remote from the image. This source position, however, gives an objectionable "tail" to the line shape as discussed in § 10.3.

In all cases an increase of d is accompanied by an increase in resolution.

§ 11. The β-ray Continuous Spectrum.

§ 11.1 Introduction.

A β-ray continuous spectrum is observed by plotting the β-ray counting rates at various settings of the detector slit, in the plane of focusing, against the detector setting. The abscissa chosen for such a plot is the distance, denoted by a, of the centre of the counter slit from the centre of the source slit. Corresponding to every value of a, there is a value of ρ, and from the value, H, of the intensity of the magnetic field for the plot, $H\rho$ values corresponding to each detector setting may be calculated. Superimposed on this continuous spectrum will be internal conversion electron lines, and it is necessary to estimate the shape of the continuous spectrum for regions in which lines are situated.

For any particular setting of the magnetic field only a limited range of $H\rho$ values is focused (corresponding to values of ρ from ~3 cm. to ~6 cm.). Hence a complete mapping of a continuous spectrum usually involves several plots, each made at a different field setting. The values of the field are chosen in such a manner that the $H\rho$ values of adjacent plots overlap slightly.

It is then necessary to deduce the true momentum spectrum from the observed series of β-particle

counting rates at various field settings. To achieve this, a detailed study of the nature of the observed continuous spectrum is necessary.

§ 11.2 General nature of the observed continuous spectrum.

In this discussion frequent reference to line profiles similar to those of figures 2.15 and 2.16 will be made.

A profile, such as that of figure 2.15, shews the variation, with x', of the fraction of the electrons (leaving each square cm. of the source) which arrive in a strip of width dx' and length 2ℓ in the plane of focusing. The rate at which electrons arrive in an image strip of these dimensions is then given by multiplying the ordinates of the profile by the rate at which electrons of this momentum leave the source (per sq. cm. of the source). A profile modified in this way will be referred to as an "unscanned" profile.

By the term "'scanned' profile" reference will be made to the line shape produced by scanning the "unscanned" profile with a counter slit of width 2w and length 2ℓ . A profile similar to that of figure 2.16, but with ordinates modified in the manner indicated above, is an example of a "scanned" profile.

The distribution of electrons which fall in a strip of the image plane of width 2ℓ (arising from a

portion of the continuous spectrum) may then be regarded as the integral of an infinite number of overlapping "unscanned" profiles. The area under each member of this set gives the rate of arrival of electrons, with momenta in a range of dp about a momentum p, in this image strip of width 2ℓ .

For a source which, for the sake of argument, is now supposed to possess a flat momentum spectrum, the areas under the "unscanned" profiles, focused at various positions in the image space, will not be equal, due to the diminution of the solid angle as ρ increases. If allowance could be made for this variation in solid angle, the areas enclosed by these "unscanned" profiles would have to be plotted against the momentum p, or the $H\rho$ value of the "representative" point on the profile (rather than the appropriate value of a) before a true representation of the original momentum spectrum would be given.

The discussion has been limited to the case of one specific field intensity H. Doubling the value of H will double the total range of momentum focused. The "unscanned" profiles of the continuous spectrum may then be regarded as being packed twice as closely as before.

The integrating effect of the finite width of the counter window now has to be considered. Movement of the slit through an "unscanned" profile gives a

"scanned" profile. Hence, for a source possessing a postulated flat momentum spectrum, movement of the counter window through the whole plane of focusing gives an infinite number of overlapping "scanned" profiles of gradually changing size and shape (which again become packed twice as closely together on doubling the value of the field intensity).

Due to the fact that electrons of a specific trajectory are counted repeatedly when a counter slit of finite width traverses an "unscanned" profile, the area under a scanned profile will bear a definite relation to the area under an "unscanned" profile, (both profiles being plotted against the distance a). The ratio of the area under a "scanned" profile to that under the corresponding "unscanned" profile will, however, vary with the position at which the profiles are focused unless the areas under "unscanned" profiles, focused at all image positions, are made equal.

That this is the case may be shewn by writing the double integral corresponding to the area under a "scanned" profile, as a doubly infinite series of terms, each of the form f(a), where this function gives the shape of the corresponding "unscanned" profile.

Since the ratio of the area of any "scanned" profile to that of the corresponding "unscanned" profile is constant when the areas under all "unscanned"

profiles are made equal, the ratio will also be constant when the areas under all "scanned" profiles are made equal.

This means that if normalizing factors could be found to make the areas under "scanned" profiles all equal, in the case of a source with a postulated flat momentum spectrum, then for any other source, the area under each "scanned" profile, after normalization, would be proportional to the rate of emission of electrons by the source, in the momentum range dp at the momentum p, to which the profile refers.

To summarize the argument, the rate of emission of electrons per square cm. of the source, possessing momenta in the range dp about a momentum p is given by the area enclosed by the appropriate "unscanned" profile. When normalized the area of the corresponding "scanned" profile is proportional to the area of the "unscanned" profile, the constant of proportionality being independent of the position in the image plane at which the "scanned" profile is focused. Hence the area under a normalized "scanned" profile is proportional to the rate of emission of electrons, by the source, of momenta in the range dp about p.

Three problems then remain. Firstly the area under a "scanned" profile has to be determined from the observed β-ray counting rate. Then normalizing

factors must be found to make such areas equal in the case of a postulated source with a flat momentum spectrum. Lastly the ρ value representative of a given counter setting, in the case of the continuous spectrum, has to be determined in order to find the momentum, p, to which the "scanned" profile under consideration, refers.

§ 11.3 The determination of the area under a "scanned" profile from the observed β-ray counting rate.

Due to the finite width of the counter window, a range of electron momenta, $\Delta\rho$, enters the window at any given setting of the detector. One limit to this range is set by the momentum of the "unscanned" profile whose leading edge falls in the image space at a position occupied by the edge of the counter slit nearer to the source, and the other limit is set by the momentum of the "unscanned" profile, the tail of which falls in the image space at the position occupied by the edge of the counter slit remote from the source. The rate at which electrons, possessing momenta in the elementary range dp about a momentum p (which lies within the finite range $\Delta\rho$), enter the counter slit is then given by the area, subtended by the counter window, of the appropriate "unscanned" profile.

If it is assumed that over the range of momenta $\Delta\rho$, the shape and size of all elementary "unscanned"

profiles remains sensibly constant, the momentum distribution of the electrons which enter the detector window is obtained from the movement of an "unscanned" profile across the fixed counter slit, by plotting the areas of the profile subtended by the slit against the momentum corresponding to each position of the profile. The total area under this distribution gives the counting rate for electrons in the range $\Delta\rho$.

Let the abscissae of this distribution, now expressed as $H\rho$ values corresponding to the momenta p, be divided by H. The area of this distribution is now $\frac{1}{H}$ of the area of the distribution plotted against $H\rho$. Let this distribution now be plotted against a (that is the distance from the centre of the source slit to the centre of the counter slit) instead of ρ . ρ and a are related by the equation

$$4\rho^2 = a^2 + d^2$$

where d is the distance between the source and the source slit.

Hence $$\frac{da}{d\rho} = \frac{4\rho}{a}$$

Over small ranges of ρ, $\frac{da}{d\rho}$ will remain effectively constant, even when ρ is small, and the value appropriate to the position of the centre of the counter slit may be taken to apply to the whole range $\Delta\rho$ of the distribution under consideration.

The area of the distribution plotted against

a , is therefore $\frac{4\rho}{a}$ of the area of the distribution plotted against ρ, and $\frac{1}{H} \cdot \frac{4\rho}{a}$ of the area of the distribution in $H\rho$.

Hence the area of the distribution in a is $\frac{c}{e} \cdot \frac{1}{H} \cdot \frac{4\rho}{a}$ of the counting rate for electrons in the range Δp of the continuous spectrum, since $H\rho = \frac{pc}{e}$.

But this distribution in a is the "scanned" profile corresponding to the "unscanned" profile (of constant shape) which was moved across the fixed detector slit, since the process of scanning may either be performed in this fashion or by moving a counter slit across a fixed "unscanned" profile.

The argument applies to all settings of the magnetic field, since division of the observed counting rate by H in effect standardizes the "packing" of "unscanned" profiles referred to earlier.

To summarize, let A represent the area of a "scanned" profile which refers to momenta in the range dp about the momentum p. Then

$$A = \frac{c}{e} \cdot \frac{1}{H} \cdot \frac{4\rho}{a} \cdot N$$

where N is the counting rate for electrons of momenta in the range Δp, which are capable of entering the detector window.

§11.4 The normalizing factors for the continuous Spectrum.

The appropriate normalizing factors could be obtained analytically from the areas under calculated "scanned" profiles focused at various positions in the image space. The arithmetical work involved would, however, be very considerable, and, moreover, an experimental objection to this method exists which will be discussed in Chapter 5.

To obtain the normalizing factors, experimental methods were therefore adopted which are described in detail in Chapter 5.

The problem is to find numerical factors by which the areas of individual "scanned" profiles, resulting from a postulated source with a flat momentum spectrum, are made equal.

Clearly a direct approach is impossible for such a source does not exist. If instead a flat portion of a real momentum spectrum is selected, which is situated about an $H\rho$ value of, say, k, then from observations of the counting rates, N_1, N_2, ---------- with the detector set at radii ρ_1, ρ_2, ---------- and the field intensities H_1, H_2, -------- chosen so that $H_1\rho_1 = H_2\rho_2$ ------ = k, normalizing factors may be found.

The areas under the "scanned" profiles focused at radii ρ_1, ρ_2, ---------- will be given by

$\frac{c}{e}\cdot\frac{1}{H_1}\cdot\frac{4\rho_1}{a_1}\cdot N_1$, $\frac{c}{e}\cdot\frac{1}{H_2}\cdot\frac{4\rho_2}{a_2}\cdot N_2$, - - - - - - - - - - - - - - .

These areas, when normalized, are proportional to the rate of emission of electrons by the source in the momentum range dp at a momentum p which corresponds to the $H\rho$ value of k selected.

Hence, after correcting the rates N_1, N_2 ---- for source decay, the required normalizing factors are

$\frac{e}{c}\cdot H_1\cdot\frac{a_1}{4\rho_1}\cdot\frac{1}{N_1}$, $\frac{e}{c}\cdot H_2\cdot\frac{a_2}{4\rho_2}\cdot\frac{1}{N_2}$, - - - - - - - - - - - - . *

This method is similar to that described by Feather, Kyles and Pringle[2], for the same purpose.

Other experimental methods for determining the normalizing factors will be discussed in chapter 5.

§ 11.5 <u>The normalization of the conversion lines</u>.

"Scanned" profiles of conversion lines are observed. These profiles are usually superimposed on the continuous spectrum, and so an estimate of the β-ray counting rate, due to the continuous spectrum has usually to be deducted from the total counting rate on a line before the "scanned" line profile itself is obtained. The area under the profile (plotted against the distance a) will, after normalization, be proportional to the area under the corresponding "unscanned" profile. Normalization is required to make the area of the "scanned" profile of a conversion line independent of the value of a at which the profile is focused.

---

* See §11.6.

The normalizing factors found for the continuous spectrum are therefore also appropriate to conversion lines.

To obtain a correct representation of the conversion lines on the continuous momentum spectrum the area of the line, after normalization, is plotted as an ordinate at the momentum obtained from a knowledge of the intensity of the magnetic field and the value of a, appropriate to the "representative" point on the line, discussed in § 8.

§ 11.6 Alternative procedure for normalization.

Reduction in the arithmetical work of normalization results from plotting conversion line profiles on the normalized continuous momentum spectrum. Each normalized ordinate of the profile has then to be multiplied by the factors $\frac{c}{e}\cdot\frac{1}{H}\cdot\frac{4\rho}{a}$ to correct for the change from an abscissa of a to an abscissa of p.

The area under the profile on the momentum spectrum will then correctly represent the rate of emission of conversion electrons of momentum p by the source.

To normalize either a line, or the continuous spectrum, the counting rate, after division by H, is multiplied by $\frac{c}{e}\cdot\frac{4\rho}{a}$. The result is then multiplied by the normalizing factor which includes the terms $\frac{e}{c}\cdot\frac{a}{4\rho}$.

These terms may therefore be omitted from the normalizing factors which then become $\frac{H_1}{N_1}, \frac{H_2}{N_2}$, ----

(adopting the notation of § 11.4), and the observed counting rates only require division by H before the application of these modified normalizing factors.

§11.7 The "representative" momentum of the range Δp which enters the counter window.

If the "scanned" profile is plotted against ρ a curve is obtained which possesses the same shape as the momentum distribution of the electrons, arising from the continuous spectrum, which enter the counter window. When the value of a, corresponding to the minimum value of ρ of this distribution, is a_1 and when a_2 corresponds to the maximum value of ρ of the distribution, the ρ value for the setting of the centre line of the detector slit is given by $\frac{a_1 + a_2}{2}$. This ρ value will not necessarily "represent" the ρ value for the distribution.

The method for obtaining the "representative" ρ value has been established by Lawson and Tyler[15]. Let the function $T(\rho)$ refer to the distribution in ρ. Then the "representative" ρ value, denoted by ρ_0, is given by the equation

$$\int (\rho - \rho_0) T(\rho) \, d\rho = 0 .$$

ρ_0 is therefore the abscissa of the mass centre of a card cut to the shape of the distribution in ρ.

The difference between ρ_0 and the value of ρ corresponding to the centre line of the counter slit is,

in most cases, very small.

§ 12. The ratio of the line height to the height of the background.

In the first place, the continuous spectrum, together with any internal conversion electron lines, is plotted against a, the distance between the centre of the counter slit and the centre of the source slit, for various settings of the magnetic field.

To recognize the existence of weak conversion lines, it is desirable that the design of the spectrometer should not reduce the maximum height of a conversion line relative to that of the continuous spectrum.

Let N' be the rate of emission of electrons of the continuous spectrum by the source (per sq.cm. of the source), in the momentum range Δp about a momentum p. Δp is the range of electron momenta capable of entering the detector slit at a particular setting.

Let A' be the area of a profile, corresponding to that of figure 2.16, for the particular counter setting.

Then the rate of counting electrons of the continuous spectrum will be $N'A' \cdot \frac{e}{c} \cdot \frac{a}{4\rho} \cdot H$ (cf. § 11.3).

Where N'' represents the rate of emission of internal conversion electrons of momentum p by the source (per sq.cm. of the source), the maximum height of a conversion line is given by N'' multiplied by the maximum height of the profile of figure 2.16.

The ratio of the line height to the background will therefore be proportional to the maximum height of the profile of figure 2.16 divided by the area of this profile.

A high value for the line: background ratio will therefore be given when a profile such as that of figure 2.15 has steep sides and a flat top, and the counter window is chosen to be equal to the width of the profile at half the maximum height.

The conditions for high resolution will automatically give a high line:background ratio.

Lines of small momentum will be counted with less background than lines of high momentum since the background counting rate is proportional to H.

§ 13. Summary of optimum geometrical conditions for various types of experiment.

The particular choice of the source slit and counter window widths, and of the source size, strength and position depends on the particular experiment to be performed. Each type of experiment will now be considered.

§ 13.1 Experiments to investigate the existence of coincidences between internal conversion lines.

Before specifying the geometrical conditions for experiments of this type expressions for the genuine coincidence counting rate and for the chance coincidence rate will be established.

Let there be N disintegrations of the source per second. Let:-

(i) f_1 be the fraction of these disintegrations in which a particular ~~γ-ray, say γ_1 is emitted,~~ transition (γ_1) takes place.

(ii) c_1 be the probability of this ~~γ-ray's~~ transition's giving rise to a particular internal conversion electron, the line of which is to be studied.

(iii) ϵ_1 be the probability of detecting an electron of this momentum, taking into account both the solid angle subtended by the counter window at the source, and the efficiency of the counter to electrons of this momentum.

(iv) Nb_1 be the number of background electrons of the β-ray continuous spectrum counted when the detector is set on the peak of the particular internal conversion line of γ_1.

(v) f_2, c_2, ϵ_2 and Nb_2 refer to a second γ-ray, γ_2, in the same manner, which is emitted within a time τ of γ_1 in a fraction, p_2 of the occasions in which γ_1 is emitted. τ is the resolving time of the coincidence set.

With the detectors set on the peaks of the respective lines the following coincidence counting rates will be obtained:-

(a) The genuine rate between the internal conversion electrons, which will be:-

$$G_1 = N f_1 c_1 \epsilon_1 p_2 c_2 \epsilon_2 \qquad (2.58)$$

(b) The genuine rate between the internal conversion electrons counted in ~~one~~ either detector and the electrons of the β-ray continuous spectrum counted in the other detector, which will be:-

$$G_2 = N (f_1' c_1 \epsilon_1 b_2 g_2 + f_2' c_2 \epsilon_2 b_1 g_1) \qquad (2.59)$$

where the fractions g_2 and g_1 select, from the total number of electrons of the continuum counted, electrons of those partial β spectra which are in coincidence with γ_1 and γ_2 respectively. f_1' and f_2' respectively then refer to the fraction of the disintegrations in which γ_1 and γ_2 follow the appropriate modes of

β disintegration.

(c) The genuine rate between the internal conversion electrons (or electrons of the β-ray continuous spectrum) counted in either ~~one~~ detector and the γ-rays counted directly from the source in the other detector which will increase with ϵ_1 and ϵ_2 (or with b_1 and b_2) and with the net efficiency of the detectors to γ-rays.

(d) The genuine rate between the γ-rays counted in the detectors directly from the source, which again increases with the net efficiency of the detectors to γ-rays.

(e) The chance counting rate which will be:-

$$C = 2N^2\left(b_1 + f_1c_1\epsilon_1 + h_1 + \frac{n_1}{N}\right)\left(b_2 + f_2c_2\epsilon_2 + h_2 + \frac{n_2}{N}\right)\tau \qquad (2.60)$$

where Nh_1 and Nh_2 are respectively the total number of counts recorded in each counter per second due to γ-rays direct from the source and n_1 and n_2 are the number of noise counts recorded per second.

The geometrical conditions suitable for the study of coincidences between conversion lines may now be discussed.

The source and its backing must be as thin as possible to allow the transmission of the internal conversion electrons with the smallest loss of energy. For all coincidence studies the strength of the source should, wherever possible, be limited to make the genuine

coincidence rate not less than the chance coincidence rate. The source should not, on the other hand, be so weak that excessively long counting periods are required to achieve the required statistical accuracy in the number of genuine coincidences. Geometrical changes which produce an increase in the required genuine coincidence counting rate, without an even larger increase in the chance coincidence rate therefore lead to a reduction in the time spent in counting. It is clear from equations 2.58 and 2.60 that an increase in the solid angles subtended by the detectors at the source would produce an increase in G_1 with an almost proportionate increase in C, (for b_1 and b_2 will depend on the solid angles). Hence large solid angles are desirable to reduce the time spent in counting.

In this connection it is noteworthy that "line" sources do not offer great advantages, for the source slit must be broad to obtain a large solid angle, and so advantage may not be taken of the high resolution usually associated with line sources (vide § 10.4).

The electrons of the β-ray continuous spectrum lead to unwanted genuine coincidences, in addition to chance coincidences, and the ratio of line height:background height should therefore be as large as possible. When lines are closely spaced the resolution should be as high as possible.

Hence, having decided upon the minimum width of the source (set at a suitable emission angle if necessary) for adequate thinness and strength, the slit width is calculated from equation 2.52. The equation applies to a source displaced towards the image, from the central position, by half its effective width; this position is adopted as it gives an increased solid angle as discussed in § 10.3. Moreover the absence of a "tail" to the line profile accompanying this source position will tend to improve the ratio of line height: background height. Equation 2.52 is solved for the largest radius of curvature to be used (as discussed in § 10.2).

To improve further the line:background ratio the width of each counter slit may then be chosen to be equal to the half width of the approximate curve giving the line spread along the X' axis of the image at the particular radius at which each conversion line is focused (cf. § 10.3).

It may be necessary to adopt a modified value for the source width if either the resolution or the solid angle is inadequate.

The length of the counter window is always made as large as possible, and the γ background rate is reduced to a minimum. This is achieved in a manner discussed in chapter 3 .

§ 13.2 Experiments to study coincidences between γ rays direct from the source and the β-ray continuous spectrum.

A high degree of resolution for the β detector is not essential for these experiments but both the β and the γ counters should subtend large solid angles at the source. The source, (which again need not be extremely narrow), should be off-set from the central position towards the image by half its effective width. The source slit width is then found from equation 2.52 but now at the minimum radius of curvature to be employed, since the need for high resolution is not so important as the requirement for a large solid angle. The counter slit width may be large to produce a further increase in the solid angle subtended by the β-counter at the source.

Under these conditions the range of momentum of electrons of the continuous spectrum which enters the counter window at a particular setting will be higher than usual. When an end-point of the continuous spectrum falls within this range, a "tail" is produced extending beyond the true upper limit of the spectrum. Even when a broad counter slit is used, the statistical error involved in the coincidence counts does not warrant the application of a mathematical correction for this effect.

The γ-ray counting rate in the β-detector is reduced as much as possible.

§ 13.3 <u>Experiments to study coincidences between γ-rays direct from the source and internal conversion electron lines.</u>

Especially for closely spaced lines a fairly high degree of resolution is required for experiments of this type. This necessitates a reduction in the solid angle subtended at the source by the window of the β-deunter, but the γ-counter may be situated to subtend a large solid angle, and the conditions are therefore not so stringent as those of § 13.1. The source, which should be narrow (but not necessarily a "line" source), is placed in a central position to give a moderate degree of resolution and the source slit width is chosen by equation 2.53, using the largest radius of curvature, to improve the resoltuion. The detector slit is chosen to be of width between the optimum widths for small and large radii (vide § 10.3), with a tendency towards the narrower value since this gives an improvement in the line heignt to background ratio at small radii as indicated in §12. The counting rate in the β-detector due to γ-rays direct from the source is reduced as much as possible.

§ 13.4 Experiments to map out the continuous spectrum and to determine the line positions using one half of the spectrometer.

The source is made as strong and as narrow as possible consistent with its being sufficiently thin, and it is placed centrally. The source slit is now reduced to a width limited only by the required statistical accuracy in the final counting rate, without the need for unduly long counting periods. The detector slit is again chosen to lie between the optimum widths for large and small radii as in § 13.3. The resolution will be high, and the ratio of the line to background height in the initial plots will be as high as possible (cf. § 12). The use of a high resolving power will make the estimate of the continuous spectrum in the regions occupied by lines more accurate (cf. §§ 11.5 and 11.6).

A further advantage of a high resolving power is that the range of momenta of the continuous spectrum which may enter the detector slit is reduced. It has been mentioned in § 13.2 that, when an end point of a continuous β-particle spectrum falls within this range of momenta selected by the detector slit, a "tail" is produced extending beyond the true upper limit. A correction for this effect, such as that discussed by Saha[16] is hardly warranted, especially as, in practice, end points are found from the final linear portions of

Fermi plots.

To improve the statistical accuracy of the β -particle counting rates, the γ background counting rate should be reduced as much as possible.

§ 13.5 Experiments to determine tne positions of lines photographically.

The resolving power of the spectrometer will be increased by using a photographic plate to determine the line positions, since by this method, the additional broadening of the line profile by the width of the counter slit is avoided. (The slit of a microphotometer, used to determine the line positions, may be made very narrow). The discussion of § 10.3 shews that the source, which should be as strong and as narrow as possible consistent with adequate thinness, is best displaced from the central position, by half its effective width, away from the image. The source slit width is then chosen by equation 2.54, into which the largest radius of curvature to be used is substituted.

CHAPTER 3.

The Scintillation Counters and Associated Electronic Circuits.

§ 1. Mechanical description of the counters.

Figure 3.1 illustrates the mechanical features of the scintillation counters. The bevelled brass slit D, of adjustable width, allows a narrow beam of electrons to fall upon the anthracene crystal A. Optical contact between the crystal and the perspex rod, C, (of 1" diameter) is made by a thin layer of white petroleum jelly which, when tested with a "Unicam" quartz spectrophotometer, was found to transmit radiations of wavelength down to 3500A° with nearly 100% efficiency. Care is taken to obtain a highly polished plane surface for the "shelf" on which the crystal is placed, and for the plane reflecting surface cut at 45° to the axis of the rod. The vertical plane surface, against which the crystal butts, is likewise polished, and attention is paid to the optical contact between this surface and the edge of the crystal. Light quanta, emitted during the passage of an electron through the anthracene, which occur within a suitable solid angle, are transmitted by total internal reflection along the perspex rod to the plane end, E. Petroleum jelly is again used to ensure good optical contact between this end and the glass window of the photomultiplier (E.M.I. Type 5045). The

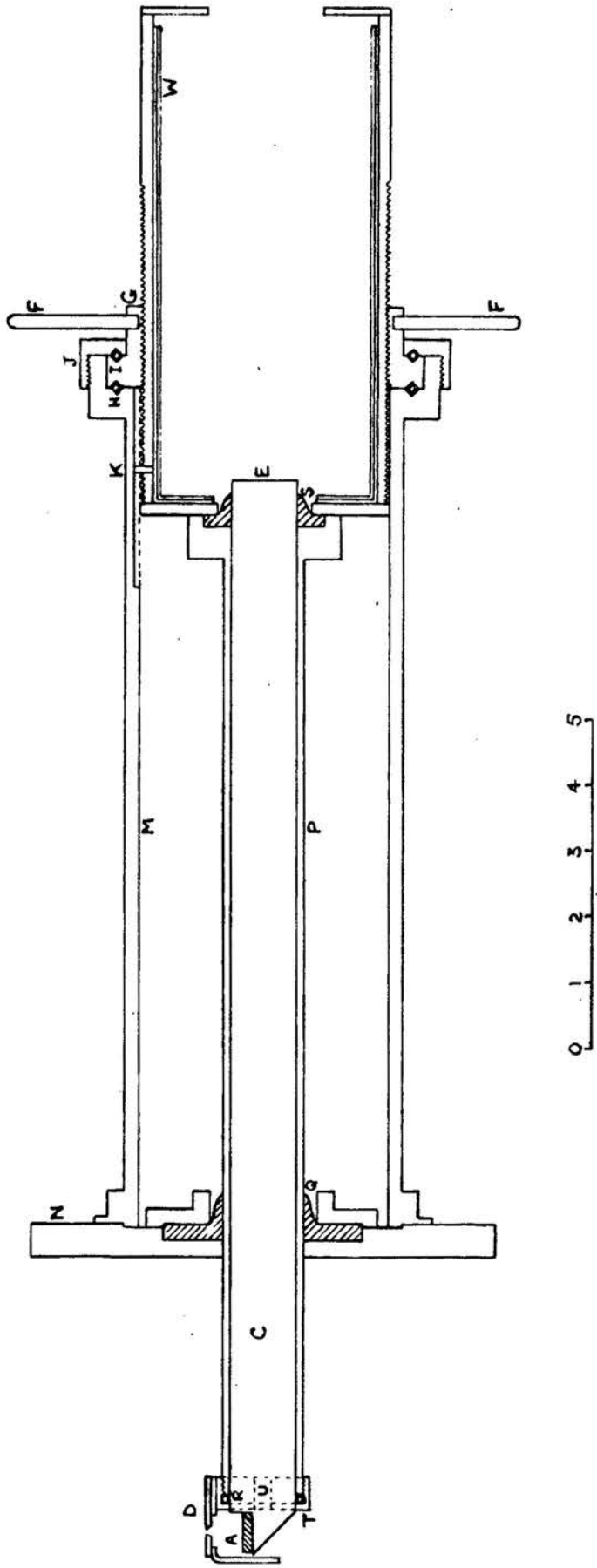

FIGURE 3-1. The scintillation counter.

photo-sensitive cathode of this multiplier is deposited directly upon the glass window, and associated with each conducted light quantum there is a certain probability of the emission of an electron from the cathode surface. The base of the photomultiplier is spring loaded to maintain adequate pressure of the perspex rod on the window, without the risk of breakage of the window.

To focus β-particles of various radii of curvature at will, the perspex rod and the multiplier have to be pushed in and out of the vacuum box. This is achieved by rotation of the arms, F, attached to the screwed flange, G, which runs on ball bearings, H and I. The flange is retained by the screwed cap, J, which is held in position with grub screws. The screwed thread of the flange engages in an accurately cut double-start thread of 4 mm. pitch cut on the outer surface of the cylinder accommodating the multiplier. The pin, K, runs in a groove cut in the inner surface of the cylinder, M, and prevents rotation of the multiplier assembly. The cylinder M is attached to the brass plate, N, which is bolted to the end of the vacuum box and sealed with a neoprene ring. The perspex rod fits into a brass tube, P, which is pushed through the neoprene vacuum packing, Q. Vacuum sealing of the perspex rod is obtained by the neoprene ring, R, at the crystal end, and the

neoprene packing, S, at the multiplier end. A brass cap, T, which carries the slit system, screws on to the brass tube, P, and retains the ring R. Lugs, U, engage in horizontal grooves cut in the walls of the box and serve to locate the detector.

The radius of curvature of the β-particles which enter the detector is determined by the setting of the detector expressed in turns on the setting screw thread.

Every precaution is taken to ensure that light, other than that emitted by the phosphor, does not reach the cathode of the photomultiplier.

§2. Limitation of the length of the detector slit.

It has been observed in §10.4 of Chapter 2 that the solid angle of the spectrometer is improved by increasing the length of the detector slit. If all the β -particles which enter this slit are to strike the anthracene crystal, irrespective of the inclination of their trajectories to the medial plane, then it can be shewn that the length of the slit must be limited to 1.5 cm., when the length of the source is 1 cm. and the length of the crystal is 2.5 cm. If this criterion is not imposed and a detector slit of length 2.5 cm. is used, then the fraction of the electrons entering the slit which strike the crystal will increase with the radius of curvature. This, in turn, will produce normalizing factors of more nearly constant value.

§ 3. The electronic circuits.

The coincidence set was designed and constructed by the Electronics Division of the A.E.R.E., at Harwell. The units of which the set consists are:-

Discriminator unit type 1153A.

Coincidence mixer unit type 1153A.

Power units.

Head amplifiers.

A detailed description of the circuits will not be given, but their functions will be discussed.

The integrated pulse at the last dynode* of a photo-electron multiplier, which arises from the burst of electrons ejected from the photo-cathode, due to the rapid series of light quanta emitted by a phosphor through which an ionizing particle passes, possesses a rise-time dependent on the phosphor employed, and to a smaller extent, on the statistical spread in the electron transit times in the valve itself. For anthracene, used with the E.M.I. Type 5045 multiplier, this rise time is $\sim 10^{-8}$ sec., and a coincidence resolving time of 10^{-8} sec. may be used without loss of genuine coincidences.

---

* The last dynode rather than the anode is used to obtain a positive pulse which is required for the rapid operation of the pulse shaping circuits.

It is of great importance to preserve the rapidly rising leading edges of the pulses until they are mixed with similar pulses from the second channel in the coincidence unit. In order to achieve satisfactory operation of the coincidence mixer, pulses of some 10 volts amplitude are required. This means that the pulses obtained from the multiplier require an amplification of about 50, at a bandwidth from 0 to ~ 100 Mc/s.

The multiplier itself generates noise pulses with a distribution shewing a rapid increase in the number as the amplitude falls. The output pulses of the multiplier due to mono-energetic β-particles are, on the other hand, of nearly constant height (cf. § 5). It is therefore necessary to restrict the number of noise pulses counted, by means of a pulse height discriminator. Present discriminators do not possess the requisite bandwidth, and cannot therefore be incorporated in the circuits delivering pulses to the coincidence mixer.

The block diagram of figure 3.2 shews the manner in which this difficulty is overcome.

The multipliers pass their pulses through wide-band amplifiers to a coincidence set with a resolving time of 10^{-8} sec. At the same time the pulses

are amplified at a bandwidth of ~ 5 Mc/s. and those pulses over a pre-set amplitude of ~ 5 volts are mixed in coincidence with a resolving time of 10^{-7} sec.

For a source which emits β-particles in coincidence, the output of the 10^{-8} sec. mixer records genuine coincidences, the number of which will be proportional to the strength of the source. In addition, a large number of accidental coincidences is recorded, due to the small amplitude noise pulses of each channel, together with a number of accidental coincidences between β-particles which is proportional to the square of the source strength. The output of the 10^{-7} sec. mixer, on the other hand, records the same number of genuine coincidences, together with ~10 times the number of accidental coincidences between β-particles recorded by the 10^{-8} sec. mixer. The number of accidental coincidences between noise pulses is, however, very small. The total number of accidental coincidences included in this output may be assessed, when the resolving time of the 10^{-7} sec. mixer is accurately known (cf. §8), from the single channel counting rates recorded by the scalers monitoring the output of each discriminator unit.

If the outputs of the two coincidence sets are passed into a third coincidence mixer (which possesses

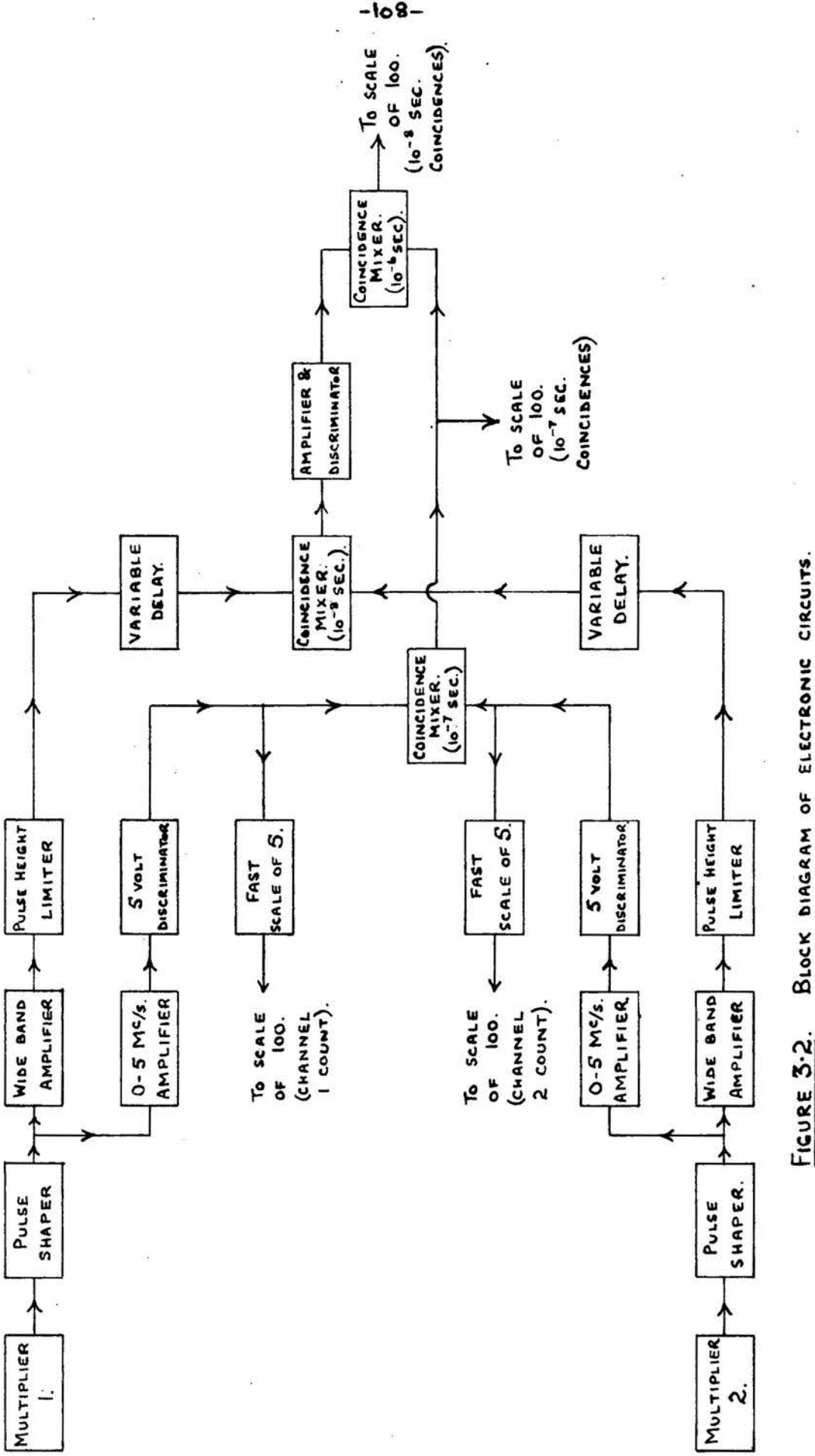

FIGURE 3·2. BLOCK DIAGRAM OF ELECTRONIC CIRCUITS.

a resolving time of $\sim 10^{-6}$ sec.) the output of this mixer will not include the noise coincidences of the 10^{-8} sec. mixer, nor will it include all the accidental coincidences between β-particles in the output of the 10^{-7} sec. mixer. The output of the 10^{-6} sec. mixer, will, in fact, record coincidences with a resolving time of 10^{-8} sec., the number of accidental coincidences included being assessed from the single channel counting rates and an accurate value for the resolving time of the 10^{-8} sec. mixer.

The following remarks refer to the design and function of the individual sections of the circuit. More detailed descriptions are given by Wells[17].

The pulse shaping circuits. The output pulses from each multiplier decay exponentially with a time constant of $\sim 10^{-6}$ sec. determined by the output circuit. For high pulse rates there is a danger of a "piling up" of pulses due to the arrival of a second pulse before the output voltage of the multiplier, arising from a previous pulse, has returned to zero. A pulse shaping circuit is therefore incorporated which gives output pulses, of approximately rectangular shape, with a 5×10^{-8} sec. duration. Pulses of this shape operate the following circuits more efficiently, and pulse rates up to 5×10^{5} per sec. may be be used. The circuit is mounted adjacent to the base

of the multiplier and has a low impedance output.

The 100 Mc/s. amplifiers are of the "distributed amplifier" type in which delay lines, inserted in the grid and anode circuits of a sequence of parallel pentodes, are used to increase the apparent gain-bandwidth product of the pentodes[18].

The pulse height limiters are incorporated to ensure that the input pulses to the coincidence mixer are of nearly constant amplitude. The circuit employs a pentode which is cut off by a negative input pulse exceeding ~4 volts in amplitude. An output pulse of ~ 0.2 volts amplitude is produced, which possesses a rise time equal to the time taken for the input pulse to reach the level required to cut the valve off.

The delay lines. By matching the delays in the two channels, loss of genuine coincidences is avoided.

The 10^{-8} sec. coincidence mixer, receives pulses of 0.2 volts amplitude from the limiters of each channel. These pulses are reflected, with a change of phase, from the short-circuited termination of a coaxial cable. The time taken for the pulses to travel to and fro along the cable is 10^{-8} sec. so that the pulses are shortened to this duration. If the leading edges of pulses, from each channel, occur within 10-8 sec. of each other, they will overlap and a 0.4 volt amplitude will be given during part of the resulting

pulse. Nominal resolving times of 2, 3, 4 and 5 x 10^{-8} sec. may be selected by switching longer coaxial cables into the mixer. The output pulses of this unit are lengthened by a germanium diode circuit in order to operate later circuits more satisfactorily.

The amplifier and discriminator unit receives the lengthened output pulses of the coincidence mixer. The gain of the amplifier (which has a bandwidth of ~ 2Mc/s) is adjusted until pulses of 0.2 volts amplitude at the coincidence mixer give output pulses of ~10 volts. The coincidence pulses will then produce output pulses of ~20 volts, and are distinguished from non-coincidence pulses by the use of a discriminator set at 15 volts, which follows the amplifier.

The 5 Mc/s. bandwidth amplifiers are conventional.

The discriminators operate at a fixed level of 5 volts. Pulses of equal amplitude are given by a triggered output circuit.

The scales of 5 are provided for rapid counting without losses. The outputs are taken to scales of 100, (A.E.R.E. type 1009). In this way the input "paralysis" time of each channel of the coincidence set is reduced to 2.5 x 10^{-7} sec.

The 10^{-7} sec. coincidence mixer is a "delay line" mixer similar in operation to the 10^{-8} sec. circuit. The output pulses operate a triggered circuit for pulse

height equalization.

The 10^{-6} sec. coincidence set is again a "delay line" mixer similar to the other coincidence sets.

Type 1009 scalers are used to monitor the outputs of both the 10^{-7} sec. coincidence unit, and the 10^{-6} sec. unit (which supplies coincidence pulses with a resolving time of 10^{-8} sec.).

§4. Screening of the electron multipliers from the stray field of the spectrometer magnet.

To check that the electron trajectories between the dynodes of the photo-multiplier were not being defocused by the stray field of the spectrometer magnet, a radium source was fixed to the tube P (of Fig. 3.1) and the counting rate of the multiplier was compared, at various positions in the stray field, with the rate when the multiplier was situated in a region free from the spectrometer field. Initial tests shewed that a reduction in the counting rate occurred when the multiplier entered a field at right angles to its axis of intensity exceeding 1 oersted. Double-walled "mu-metal" screening cans, shewn at W of Figure 3.1, were fitted, and after extending the perspex light guides, (and the brass tubes M and P), by eight inches, no detectable change in the counting rate was observed as the multiplier was moved in to the operating position closest to the magnet. These tests were made at a field setting of ~2000 oersteds, which exceeded the strongest field used in later experiments. Tests were made to ensure that the proximity of the "mu-metal" cans did not affect the field in the box by observing that the position of the F line of ThB $\rightarrow$C focused at a radius of 6 cm., remained in exactly the same position whilst a similar "mu-metal" can was placed in various positions near to the top of the spectrometer box.

§5. Counting rate/multiplier voltage characteristics.

With mono-energetic β-particles of energies exceeding ~80 keV, the scintillation counters shewed plateaux in the counting rate/multiplier voltage* curves, starting at a voltage which decreased as the energy of incident β-particles increased. Corrections for the noise and γ-ray background counting rates were made, and typical curves are shewn in Figure 3.3.

The interpretation of these curves was that, at the starting voltage of a plateau, the gain of the multiplier was sufficient for all pulses arising from the corresponding β-particles to exceed an amplitude of 5 volts at the discriminator. That the characteristics shew a fairly steep rise indicates that pulses obtained from mono-energetic β-particles are of almost constant amplitude. This in turn implies that the light collection from various parts of the crystal is uniform.

The counting rate due to γ-radiations from the source increases with the multiplier voltage. This counting rate was reduced by operating the multipliers at the starting voltage of the plateau for β-particles of the particular energy counted. Unnecessary sensitivity to low-energy scattered β-particles was, at the same time, avoided.

It was assumed that the β-particle counting

* E.H.T. power units (Type 1033A), which derive their outputs from 215 Kc/s oscillators, were used to supply the voltage to the multipliers.

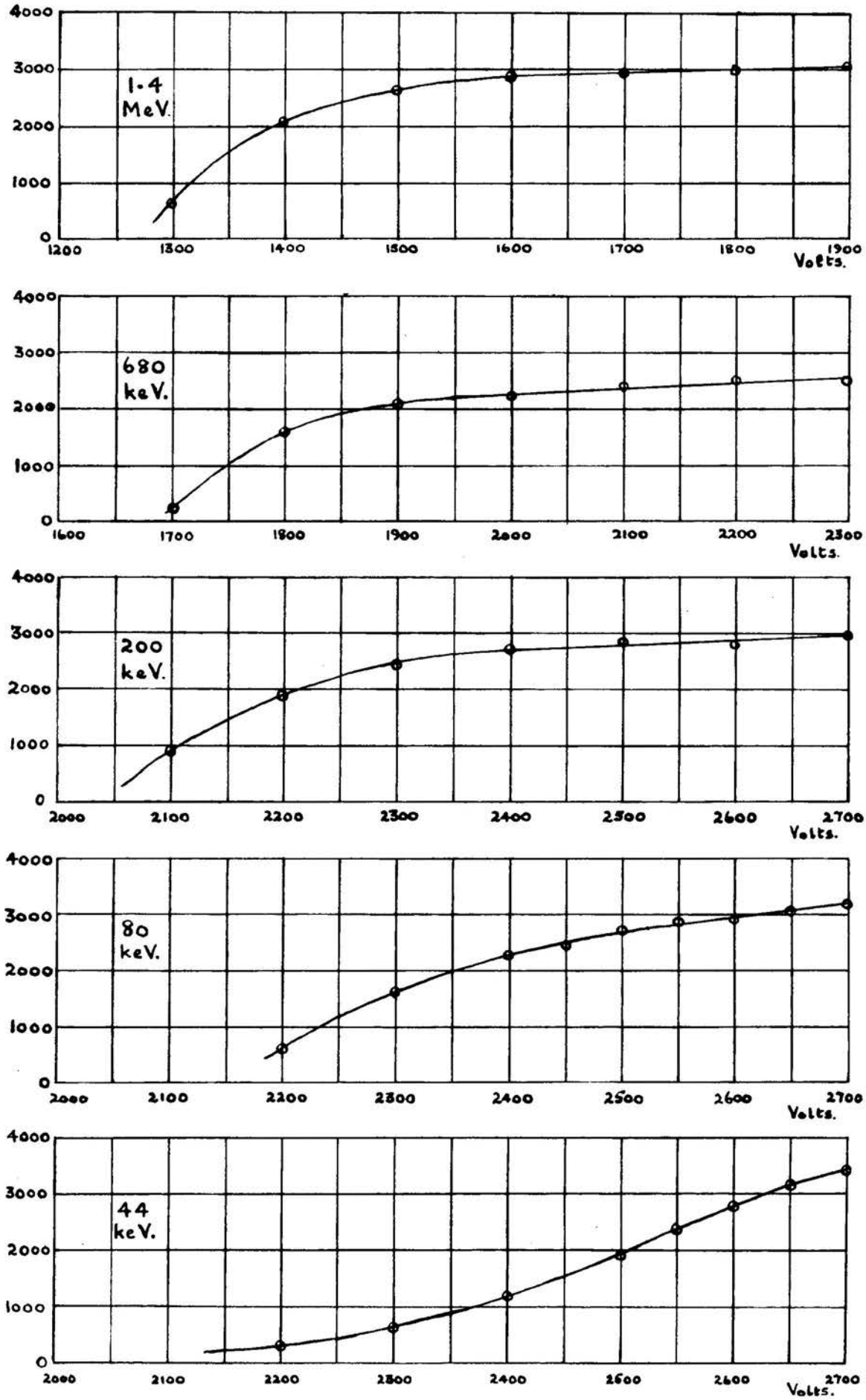

FIGURE 3-3. Typical counting rate / multiplier voltage characteristics for monoenergetic β-particles of various energies. (5mm. thick Anthracene crystal).

efficiency, on a plateau, was 100%. Although β-particles of 30 keV could be counted, those β-particles of energies below ~80 keV were counted with efficiencies which became less as the β-particle energy was reduced.

§ 6. Noise and its reduction.

It has been mentioned in § 3 that the distribution of noise pulses obtained from a photomultiplier shews a rapid increase in number as the amplitude of the pulses diminishes. Discrimination against noise is achieved by allowing only those pulses of amplitude greater than a certain pre-set value to pass to the counting circuits. Since the pulse height obtained at the output of a photomultiplier increases with the voltage applied, the noise also increases. A limit to the lowest energy β-particles which may be counted with 100% efficiency is therefore reached when the starting voltage of the plateau is at a value so high that the noise counting rate is large compared with that for the β-particles.

It is therefore of great importance to ensure that, for β-particles of a particular energy, the largest possible intensity of light is transmitted from the phosphor to the photoelectric cathode of the multiplier, for then the largest number of electrons will be ejected from the cathode and the pulse height at the output will be a maximum. Unfortunately the particular arrangement of the spectrometer does not favour a light collecting system of high efficiency. Of several different geometrical arrangements for mounting the crystal at the end of the light guide, the method

adopted proved to be the most efficient. Arrangements requiring crystals of large volume would give high background counting rates for γ-radiations. Various reflecting surfaces, including aluminium foil and layers of magnesium oxide, placed in different positions, were tested, but none was found to improve the efficiency of light collection, judged by the starting voltage of the plateau. The situation of the detector slit in a region of high field intensity does not permit the use of short light guides with correspondingly low transmission losses.

Attention was then paid to the reduction of the multiplier noise itself. A very considerable contribution to the total noise counting rate at high multiplier voltages was found to be due to discharges between the cathode of the multiplier (operated at a high negative potential) and the earthed box in which the multiplier was mounted. To shew that this was the case, the box was insulated from earth, and with a multiplier voltage of ~3000 v. it was found that the noise counting rate gradually fell. An electrostatic voltmeter indicated that the box had acquired a potential ~1500 v. When the box was earthed, the noise counting rate immediately increased to its former value. A coating of paraffin wax on the cathode connections to the multiplier and on the interior of the box, together with a sheet of polythene for additional insulation were found

greatly to reduce noise caused in this way.

§ 7. The Phosphors.

Anthracene was an obvious choice of phosphor for β-β coincidence studies with a resolving time $\sim 10^{-8}$ sec., since the light yield for β-particles is very high. The decay time moreover is sufficiently small, the emission of light falling to ½ of its initial value in $\sim 3 \times 10^{-8}$ sec. at room temperatures.[19,20] Moreover large single crystals of anthracene may be grown, which leads to efficient light collection. The vapour pressure of anthracene at room temperature is sufficiently low to allow the crystal to be kept in the vacuum box of a spectrometer over long periods without detectable loss by evaporation. The spectral emission of light by anthracene matches closely the photoelectric response of the cathode material of the particular type of photomultipliers used.

A large single crystal of anthracene was obtained from the A.E.R.E. at Harwell, from which two pieces of 2.5 cm. x 2.5 cm. x 0.4 cm. were cut and polished.

Before this crystal was obtained, a furnace was constructed for the growth of anthracene crystals by the method due to Bridgman[21]. A sealed evacuated glass tube of ~2 in. diameter containing dry anthracene powder was to be dropped very slowly through the temperature gradient produced by boiling distilled ethyl salicylate in an electrically heated jacket

surrounding the upper half of a guide tube, and by boiling distilled para-cresol in a similar jacket round the lower half of the tube. Well regulated temperatures of ~16°C above and ~16°C below the melting point of anthracene (217°C) were obtained in this way, with a very steep temperature gradient between the jackets. The development of the method was abandoned when a suitable crystal was obtained elsewhere. It is interesting to note that a similar method has been developed by Leininger[22] for the growth of crystals of stilbene.

Uniform and transparent crystalline layers of anthracene of thickness ~20 mg./cm.^{2} were however formed on the surface of a liquid. The method was used by Curling and Newton[23] for the same purpose. Anthracene, twice codistilled with ethylene glycol, was dissolved in distilled amyl acetate, and boiled. With a solution containing 1 gm. of anthracene per 8 cc. of amyl acetate, on cooling a very uniform clear polycrystalline surface layer formed due to the rapid loss of heat from the liquid surface. Such layers were found to be very satisfactory for counting those β-particles which were completely absorbed by a crystal of this thickness, since unnecessary sensitivity to γ-radiations was avoided by using such a small volume of phosphor.

For more energetic β-particles, the whole of the particle energy is not absorbed in the phosphor

which means that the light output of a thin layer is unnecessarily restricted, with a consequent reduction in the β-particle pulse height. Thicker crystals were therefore preferred, so that the counting rate due to noise, to γ-radiations, and to low energy scattered β-particles could be reduced. (cf. § 6).

§ 8. The measurement of the resolving times of the coincidence sets.

To assess the contribution of the "accidental" coincidences to a total number of coincidence counts recorded, the resolving time, τ, of the coincidence set must be known accurately, for the accidental coincidence counting rate, A, is given by

$$A = 2N_1N_2\tau$$

where N_1 and N_2 are the counting rates recorded in the separate channels of the coincidence set.

The "double source" method was used, in which a γ-source, such as radium or cobalt, was placed near to each detector. An observation of the total number of counts in each channel in a given time, together with the number of coincidences recorded by both the "10^{-7} sec." and the "10^{-8} sec." coincidence sets in that time, allowed the resolving times to be calculated. Since it was presumed that all the coincidences recorded were "accidental", care was taken to eliminate the possibility of recording genuine coincidences from the disintegrations of either source by screening each detector from the source counted by the other detector.

This method does not check that the channels carrying pulses to the coincidence set are accurately matched in time, and a separate check was made to ensure that this was the case by determining the number of

genuine coincidences recorded with delay lines of various lengths switched into the channels in turn. Correct matching was obtained when the genuine coincidence counting rate was a maximum. To ensure that no losses of genuine coincidences occurred, this rate was compared with the genuine coincidence counting rate obtained from the "10^{-7} sec." coincidence mixer.

The resolving time of the "10^{-8} sec." coincidence mixer was found to depend on the voltage applied to the multipliers. This effect was presumably due to changes with voltage in the shape of the output pulse of the multipliers, and to consequent variations in the rise time of the pulses at the coincidence mixer.

Small changes in the resolving time were found to accompany changes made in the setting of the magnetic field. These changes were attributed to changes in pulse shape caused by the small residual magnetization of the "mu-metal" multiplier screening cans as a result of the stray field, of several oersteds, which is present at either de-magnetization or re-magnetization of the permanent magnet.

For these reasons it was found necessary to determine the resolving time of the coincidence set after every change in the magnetic field or in the operating voltages of the multipliers.

§9. Use of the counters for the detection of γ-radiations.

The relatively high detection efficiency of scintillation counters for γ-radiations was found to be troublesome when detecting β-particles of low energy, for the voltage applied to the multiplier has then to be relatively high. However, this disadvantage is more than outweighed since this type of detector may be used to count only those γ-rays, coming directly from the source, above a certain minimum energy which may be selected by adjustment of the voltage applied to the multiplier.

A rough calibration of the minimum energy of the radiation registered by the counter at a particular setting of the voltage on the multiplier was made in the following way.

With the detector set as close to the source as possible, the counting rates due to the γ-radiations from a source of ^{60}Co, placed in the source holder, were observed at a series of multiplier voltages with 50 v. increments. An anthracene crystal of 5 mm. thickness was used. A histogram was drawn of the increase in counting rate corresponding to each (equal) increment in the voltage applied to the multiplier.

In addition to the Compton electrons produced by the γ-radiations in the anthracene crystal, a small proportion of photoelectrons from the metal in the

neighbourhood of the crystal was detected, since the application of a strong magnetic field reduced the counting rate.

For the cobalt source, a marked peak in the histogram occurred, of width ~150 volts. The counting rate fell to zero on decreasing the multiplier voltage by a further 100 volts below this peak. The broad peak was attributed to the 1.17 and 1.33 MeV γ-radiations.

With a source of thorium active deposit the voltage of the peak due to the 238 keV γ-radiation of ThB $\rightarrow$C was easily found, and with a radium source the peak due to the 607 keV γ-radiation of RaC $\rightarrow$D was recognized.

The detectors were presumed to become insensitive to a γ-radiation of a particular energy at a voltage somewhat below that of the corresponding peak, and in this way the calibration curve of Figure 3.4 was obtained. This calibration was used in later experiments with $MsTh_2$ to assess the minimum energy of the γ-radiations counted at a particular multiplier voltage.

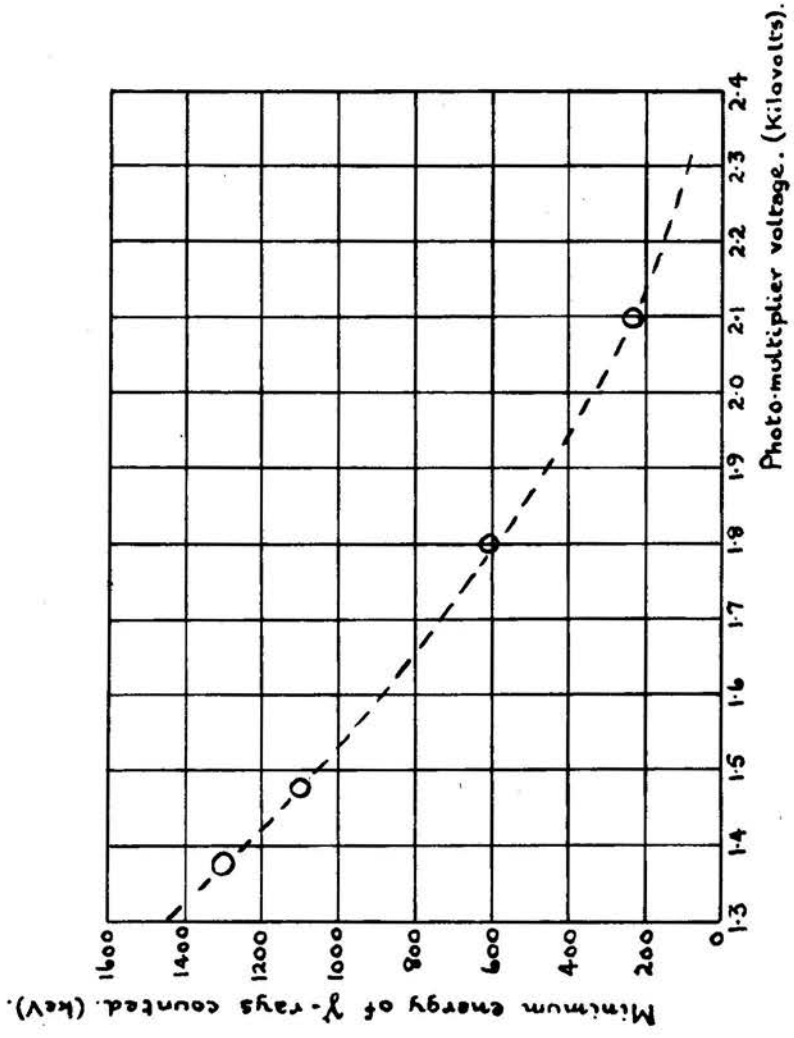

FIGURE 3·4. Calibration of γ-counter.

CHAPTER 4.

The Magnet, and the Magnetic Field.

§ 1. The magnet and the method for setting the field.

The spectrometer field was provided by the large permanent magnet designed by Cockroft, Ellis and Kershaw[24] and constructed by Messrs. Edgar Allan & Co. The air gap between the high permeability steel pole pieces of the magnet was 5.5 cm. wide and the pole pieces themselves were 17 cm. by 29 cm. in size. The coils for adjusting the magnetic field were slipped over 35% cobalt steel laminations, each 42.4 cm. x 14.6 cm. x 1 cm. in size, clamped together to form the magnet arms. These, in turn, were attached to a U-shaped soft iron yoke, 133 cm. long and 61cm. high.

The use of modern high coercivity magnetic alloys would appreciably reduce the size and weight of such a permanent magnet.

The current for adjusting the magnetic field was obtained from the 230 v. D.C. mains through a reversing switch and adjustable series resistances. Six exciting coils were provided each of 1300 turns of No. 15 S.W.G. copper wire. The maximum current used was of the order of 15 amp. per coil, providing fields up to 2000 gauss in the air gap.

In order to obtain a new field, the magnet was firstly demagnetized by using the original current but

in the reverse direction, and then a suitable re-magnetizing current was passed for some 10 secs. The magnitude of this current was obtained from a calibration of the series resistances. The whole process of setting the field to within 2% of any desired value was usually accomplished in a matter of 4 or 5 minutes.

The magnetic field, once having been set, was never found to change by a detectable amount, and such a constant field greatly facilitated the work of long period coincidence counting.

The uniformity of the magnetic field between the pole pieces had been investigated by Ellis[25] during his investigation of the γ-rays of thorium B and C. His investigation was however confined to the central regions of the magnetic field.

The need for focusing β-particle trajectories of a large range of radii of curvature in two separate sheaves meant that the electron paths could no longer be confined to the uniform central region of the magnetic field used by Ellis with his single spectrometer vacuum box. The paths of those β-particles which approached the edges of the pole faces of the magnet were therefore expected to be governed by a smaller effective magnetic field than that for β-particles of small radius of curvature which are confined to the central regions of the magnetic field. That this was the

case became apparent during the calibration of the magnetic field.

§ 2. Initial attempts to determine the field intensity.

For early experiments a search coil was mounted in the stray field on top of the spectrometer box and when rotated through 180° produced a deflection in a Grassot fluxmeter. The initial experiments were designed to obtain a constant factor which, when multiplied by the fluxmeter deflection, would give the value of the field in the spectrometer box. This factor will be referred to as the fluxmeter factor.

A conversion electron line of known $H\rho$, when focused on the slit of the detector, provides a method for determining the value of the magnetic field if the radius of curvature of the conversion electron trajectory is known from the position of the detector slit. Variation of the detector setting is obtained in a manner described in Chapter 3. Let a_o represent the distance between the centre line of the source slit and the centre line of the detector slit when the counter is set at zero turns on the adjusting screw thread, and let this distance be a when the detector is at n turns. Then where k represents the pitch of the screw thread,

$$a = a_o + nk \qquad (4.1)$$

and

$$2\rho = \sqrt{a^2 + d^2} \qquad (4.2)$$

where ρ is the required radius of curvature, and d is the distance between the centre line of the source and the centre line of the source slit.

The determination of the radius of curvature of the electron trajectory from the setting of the detector therefore depends on a knowledge of the distance a_0 .

A second conversion electron line, of known $H\rho$, focused by the same magnetic field would therefore give both the fluxmeter factor and the distance a_0 . Let the subscripts 1 and 2 refer to the first and second conversion lines respectively.

Then

$$\frac{\rho_1}{\rho_2} = \sqrt{\frac{(a_0 + n_1 k)^2 + d^2}{(a_0 + n_2 k)^2 + d^2}} \qquad (4.3)$$

This ratio is known since the $H\rho$ values of both the lines are known, H being presumed constant.

Let $$\frac{H\rho_1}{H\rho_2} = b$$

Solving equation (4.3) for a_0 and rearranging, the expression becomes

$$a_0 = \frac{-k(n_2 b^2 - n_1) + \sqrt{k^2 b^2 (n_2 - n_1)^2 - d^2 (b^2 - 1)^2}}{b^2 - 1} \qquad (4.4)$$

and H is then given by

$$H = \frac{2 H\rho_1}{\sqrt{(a_0 + n_1 k)^2 + d^2}} \qquad (4.5)$$

from which the fluxmeter factor may be determined.

The experiment was performed using sources of thorium active deposit obtained by the exposure of aluminium foils of 0.2 mg./cm.^{2} thickness to the thoron given off by a "dry" emanating preparation of radio-

thorium. For activation the foil was bent over a brass blade so that an area of 1 cm. x 2 mm. of foil was exposed. The blade was maintained at a potential of 240 v. below that of the pot containing the radio-thorium.

The activated foil was mounted on an aluminium frame, petroleum jelly being used as the adhesive. The frame was placed symmetrically under the source slit (that is, in the "central" position of Chapter 2 §10.3) and was set at an emission angle of 45° . The source slit had a breadth of 4 mm. and the counter slit was 1.5 mm. wide and 1.5 cm. long.

The F- and I- lines of ThB→C spectrum were an obvious choice, their $H\rho$ values being well established. The line shapes were observed by plotting the counting rate against the detector setting, and the mean of at least four fluxmeter deflections was obtained. That setting of the counter for which electrons from the centre line of the source, which travel normally to the magnetic field, and pass through the centre line of the counter slit, was known from the theoretical method outlined in Chapter 2 §8. Such "representative" points were used throughout to determine the radii of curvature of the conversion electrons from the line profiles.

A small displacement of an internal conversion electron line occurs if the source is slightly off-

centre. Errors due to this were reduced both by paying particular attention to the mounting of the source, and by rotating the source through 180° about an axis normal to the plane of the source, and then re-determining the line profile. The mean of the two representative counter settings obtained in this way was used to determine the radius of curvature of the electron trajectory.

From a series of observations of F- and I-lines focused by various settings of the magnetic field a set of values of the fluxmeter factor and of the distance a_o was obtained. The $H\rho$ values for the F- and I-lines used in the calculations were those obtained by Ellis[25], being 1385.8 gauss-cm. and 1751 gauss-cm. respectively. The values of a_o obtained in this way are shewn in Table 4A.

TABLE 4A.

Position of I-line (turns)	Position of F-line (turns)	a_o (mm.)	
5.0625	0.9063	51.742	
5.1406	1.1094	48.721	
5.6250	1.3438	52.174	Mean value = 50.67 mm.
6.8750	2.4063	51.156	
7.1875	2.6563	51.223	
7.9453	3.3047	50.488	
8.6875	3.9063	50.452	
9.5547	4.6563	49.414	
11.8438	6.3281	52.906	
12.3750	6.8203	51.573	
13.9063	7.9063	54.439	
16.0937	9.6719	54.140	
17.5625	10.6875	57.289	

These results clearly indicate that there is a marked increase in the value for a_o when the radius of curvature of the I-line trajectory is large. On the other hand, the agreement between the value for a_o and the measured value (50.85 mm.) is satisfactory when the I-line trajectory has a small radius of curvature. It was therefore apparent that the effective value of the magnetic field for electron paths of large radius was smaller than the value in the central regions of the field.

§3. Later experiments to determine the magnetic field.

At this stage of the investigation it was noticed that the proximity to the search coil of the "mu-metal" cans, (used for shielding the multiplier from the stray magnetic field) made a slight difference (~ 1%) to the fluxmeter deflection. The search coil mounted in the stray magnetic field was therefore replaced by a coil of much smaller area-turns (and consequently lower resistance) which was inserted into the magnetic field at the position normally occupied by the source. The search coil was rigidly mounted in a holder equipped with locating pins to ensure that it would occupy the same position in the field every time it was used. A second coil, of smaller area-turns, was mounted in an exactly similar holder, and was used for the measurement of large values of the field.

The mirror attached to the suspension of the fluxmeter was now used with a distant lamp and scale to improve the reading accuracy of the instrument.

A second series of experiments was then performed. A similar source of thorium active deposit was used and the representative position of the F conversion line determined at various field settings together with the mean fluxmeter deflection. The source was reversed as hitherto, to reduce errors due to its positions possibly being off-centre.

Each value of the magnetic field was found from equation 4.5, using the directly measured value of 50.85 mm. for a_o, and from this, the new fluxmeter factor was determined.

The fluxmeter factor shewed a definite variation, low values being obtained for small fields, when the electron paths approached the edges of the pole faces of the magnet. The factor was constant for larger values of the field when the electron paths were confined to the central regions of the field.

It would be possible to obtain such an effect if the fluxmeter deflection were a non-linear function of the magnetic field, being somewhat smaller than the correct value for large fluxmeter deflections. To shew that this was in fact not the case, the magnetic field was set to focus the F-line at a radius of curvature of 3.5 cm. and then reset to focus the I-line at the same radius. The fluxmeter factors were calculated in both cases and although the magnetic field was 1.26 times stronger for focusing the I-line, the factors were found to agree closely, as shewn in Table 4C. It was therefore assumed that the fluxmeter deflection was a linear function of the magnetic field.

The experimental results shewn in Table 4B indicate that the fluxmeter factor was constant for counter settings over the range from 0 to 7½ turns of the setting screw thread. The mean value of the

fluxmeter factor was found over this range, and the fluxmeter factors for focusing the F-line for the range $7\frac{1}{2}$ to 19 turns were expressed as percentages of the mean fluxmeter factor for the range 0 - $7\frac{1}{2}$ turns. This percentage was plotted against the counter setting and the circled points of Figure 4.1 then shew the manner in which the ratio of the effective magnetic field for focusing a conversion line, at any particular counter setting, to the value of the field at the centre, depend on the counter setting. It was assumed that the shape of the magnetic field itself did not change as the field was changed.

TABLE 4B.

Position of I-line. (Turns)	Position of F-line. (Turns).	Fluxmeter deflection. (Arbitrary units).	H (gauss).	Fluxmeter factor.	Fluxmeter factor ÷ 16·626 x 100.
-	1.7500	26.90	447.81	16.647	100.13%
-	3.375	23.92	399.21	16.689	100.37%
4.25	-	29.60	490.97	16.587	99.76%
-	3.9375	23.83	395.15	16.582	99.73%
-	5.9375	21.37	356.36	16.675	100.29%
-	7.2500	20.19	334.63	16.574	99.69%
				Mean fluxmeter factor 16.626	
-	14.8125	15.02	246.86	16.435	98.85%
-	16.5625	14.21	232.62	16.364	98.42%

§4. Re-examination of the results of the earlier experiments.

The experimental results obtained earlier using the search coil mounted on top of the spectrometer box were then re-examined. The directly measured value for a_o was used to give the value of the magnetic field using equation 4.5. Two values were obtained for each field setting, one being the effective field for focusing F-line conversion electrons, and the other for focusing electrons of the I-line. The position of the F-line was known and with this as the abscissa the corresponding ordinate was obtained from the graph of Figure 4.1. The ratio of the field found from the I-line position to that found from the position of the F-line was calculated, and this number was multiplied by the percentage read off the graph corresponding to the F-line setting. The crossed points of Figure 4.1 shew this new percentage as a function of the I-line setting. All the points determined in this way were found to lie close to the curve already drawn. The results of these calculations are shewn in Table 4C.

TABLE 4C.

Position of I-line. (Turns). (1).	Position of F-line. (Turns). (2).	$\frac{H_I}{H_F}$ (3).	F-line ordinate from graph. (%) (4).	I-line ordinate = Col. (3) × Col. (4). (5).
5.0625	0.9063	0.99739	100	99.74
5.1406	1.1094	1.00618	100	100.62
5.6250	1.3438	0.99619	100	99.62
6.8750	2.4063	0.99915	100	99.92
7.1875	2.6563	0.99898	100	99.90
7.9453	3.3047	1.00097	100	100.10
8.6875	3.9063	1.00104	100	100.10
9.5547	4.6563	1.00364	100	100.36
11.8438	6.3281	0.99512	100	99.51
12.3750	6.8203	0.99831	100	99.83
13.9063	7.9063	0.99199	100	99,20
16.0937	9.6719	0.99312	99.97	99.28
17.5625	10.6875	0.98706	99.90	98.61

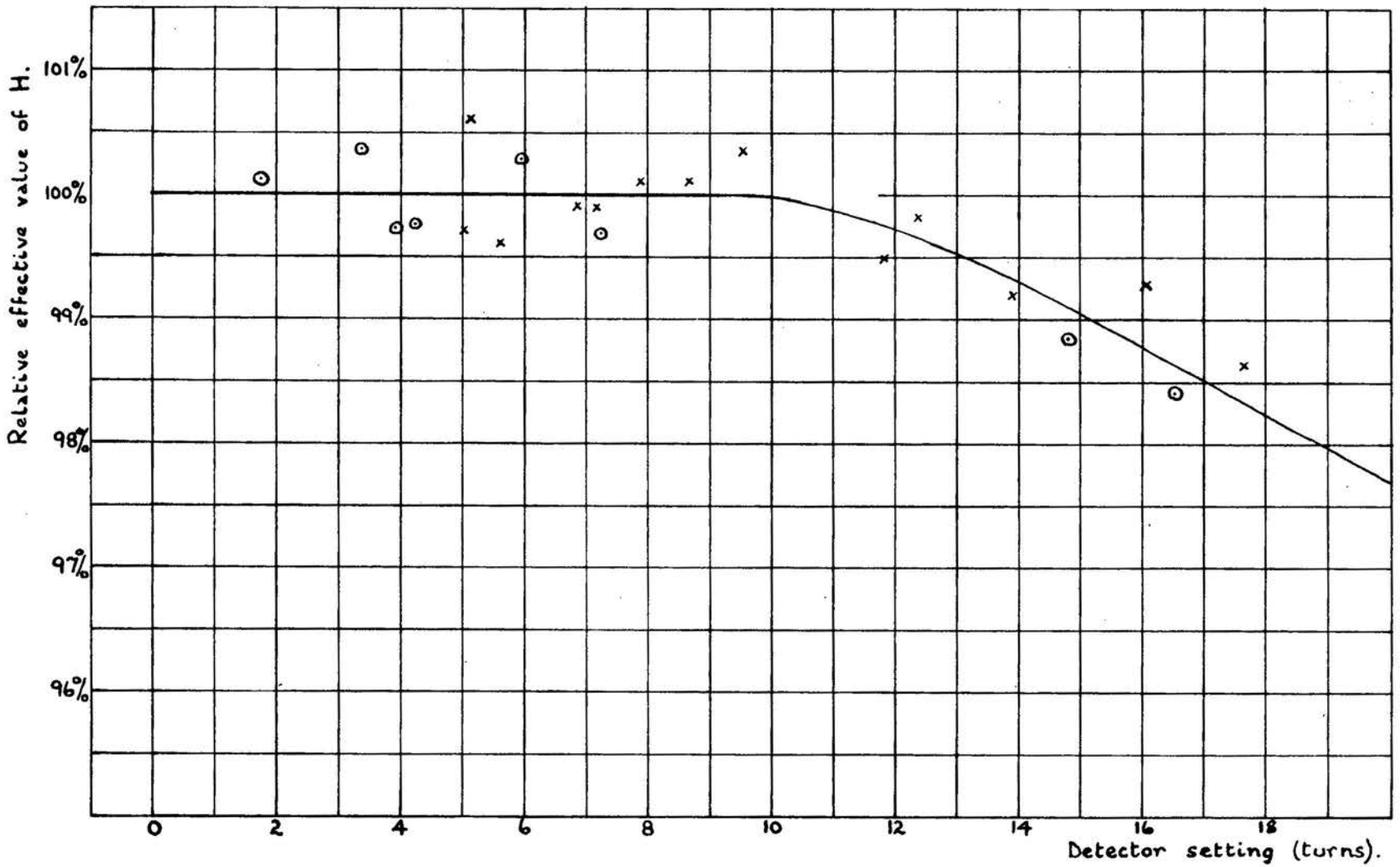

FIGURE 4·1. Circled points obtained by method of §3 of text.
Crossed " " " " " §4 " "

§ 5. Calculation of $H\rho$ values.

A tabulation of the radius of curvature of the electron trajectory as a function of the setting of the counter, measured in turns of the setting screw thread, was made using the directly measured value for a_o . From this table the $H\rho$ value could be obtained directly from a knowledge of the effective value of the field at any particular counter setting, which was determined from the fluxmeter deflection, the fluxmeter factor, and the graph of Figure 4.1. To facilitate calculation of $H\rho$ values, the tabulated values of ρ were multiplied by the percentage at that counter setting obtained from the graph, and a constant value of H was then assumed, this value being that given directly by the fluxmeter deflection and the fluxmeter factor.

The fluxmeter factor for the smaller area-turns coil was obtained directly from that of the larger area-turns coil by comparing the fluxmeter deflections for each coil produced by a suitably chosen magnetic field.

CHAPTER 5.

The Experimental Methods for Determining the Normalizing Factors.

§1. Introduction.

The problem of obtaining, from experimental observations, a true representation of a momentum spectrum together with internal conversion lines of correct relative magnitude has been discussed in §11 of Chapter 2. In this connection, the need for appropriate normalizing factors has been established.

It was mentioned in §11.4 of Chapter 2 that, apart from the quantity of arithmetical work involved in obtaining normalizing factors analytically, an experimental objection exists to this method. Allowance cannot easily be made analytically for such effects as the scattering of electrons from the walls of the detector slit. Although these walls are bevelled (vide Chapter 1) the number of electrons which is likely to be scattered may vary systematically with the detector setting, since the range of angles at which electrons arrive at the plane of focusing varies with ρ. A proportion of the scattered electrons may fail to be registered by the detector. For this reason it was decided that a more reliable set of normalizing factors would be obtained experimentally.

§ 2. First experimental method.

In § 11.4 of Chapter 2 the theory of an experimental method for determining normalizing factors, due to Feather, Kyles and Pringle,[2] has been outlined. With the simplification discussed in § 11.6, the method consists of observing the β-ray counting rates N_1, N_2..... for electrons of a specific $H\rho$ value, selected in the flat portion of a momentum spectrum, at various radii ρ_1, ρ_2 ..... focused by field settings of H_1, H_2..... so that $H_1\rho_1 = H_2\rho_2$ .....

After correction for source decay, the normalizing factors appropriate to the settings of the detector are given by $\frac{H_1}{N_1}, \frac{H_2}{N_2}$ ----.

The experiment was performed with a source of thorium active deposit, of dimensions 1 cm. by 2 mm. which was mounted centrally with respect to the source slit, and set at an emission angle of 45°. The source was prepared by exposing an aluminium foil of thickness 0.2 mgm. per square cm., maintained at a potential of 240 v. below that of a pot containing a dry emanating preparation of RdTh as described in Chapter 4, § 2. The source was covered with a similar aluminium foil to prevent loss of atoms, in particular those of ThC", by α-particle recoil. The decay products of ThB were allowed to reach transient equilibrium before observations were commenced.

A source slit of 4 mm, width was used with a counter window of length 1.5 cm. and width 1.5 mm.

The value of $H\rho$ selected was 3600 oersted-cm. to satisfy the requirement for lying at a flat portion of the momentum spectrum, and to be clear of internal conversion electron lines.

The voltage on the photo-electron multiplier, which was used with a single crystal of anthracene of 4 mm. thickness, was chosen to lie near the knee of the counting rate/voltage characteristic for this value of $H\rho$, to avoid unnecessary sensitivity to γ-rays counted directly from the source.

Each setting of the magnetic field was found by multiplying the mean of four observations of fluxmeter deflection by the fluxmeter factor, as described in Chapter 4.

The β-particle counting rates were found by deducting the counting rates due to γ-rays and electron multiplier noise pulses, observed with the shutter down, from the total counting rates given with the shutter up. Corrections for source decay were made. Counting losses were negligibly small.

The relative variation of the normalizing factor with the detector setting (expressed as the number of turns on the setting screw thread) is shewn in Figure 5.1, for the particular geometrical conditions of the experiment. A factor of unity at a detector

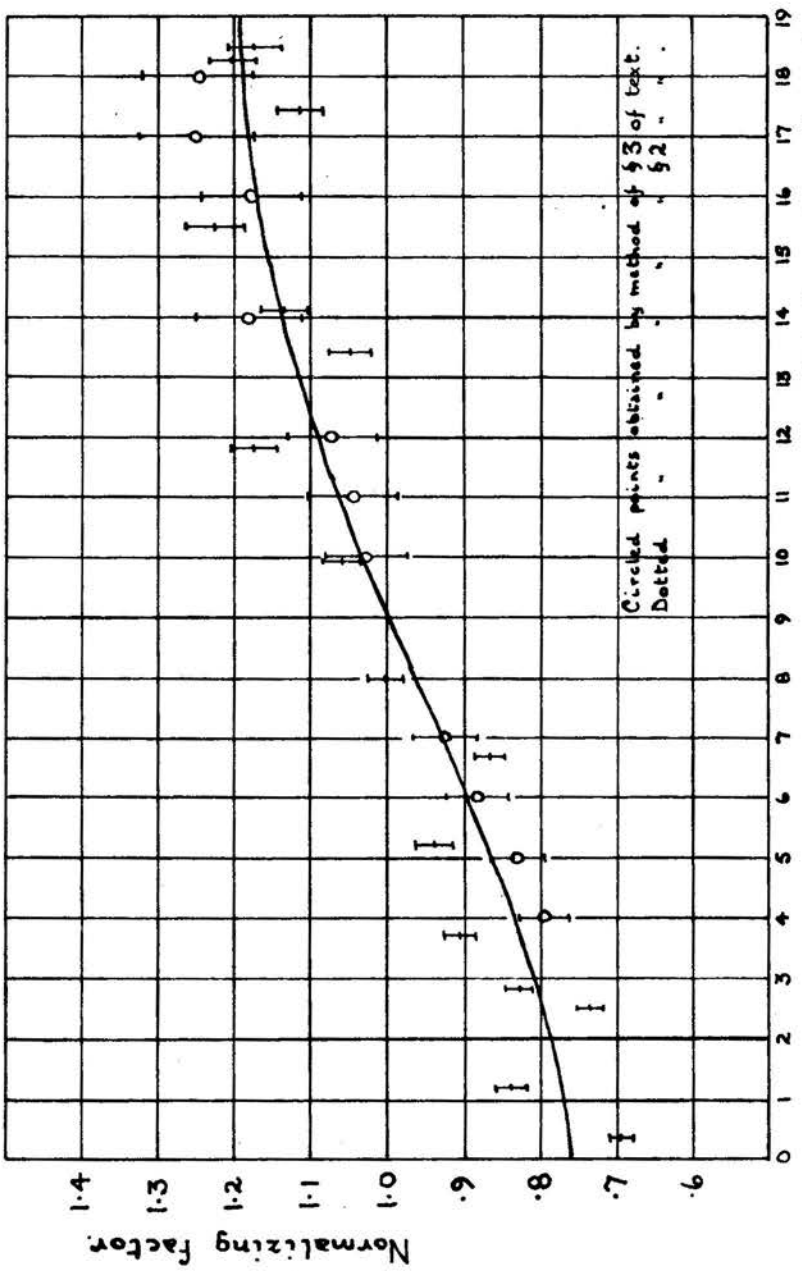

FIGURE 5·1 (See text).

setting of 9 turns was arbitrarily chosen.

In assessing the errors in the normalizing factors, a 1% error in H has been allowed together with the usual estimate of the standard deviation in each value of N.

§ 3. Second experimental method.

With the geometrical conditions of the experiment described in the previous paragraph, the continuous spectrum of Th(B+C+C") was observed over the region from $H\rho$ = 2100 oersted-cm. to $H\rho$ = 3800 oersted-cm. A single setting of the magnetic field, measured by taking the mean of four fluxmeter deflections, focused this range of $H\rho$ values.

The γ-ray background counting rate was reduced by inserting a lead block (covered with a perspex sheet to reduce scattering) between the detector and the source. The minimum radius of curvature which could be employed was consequently increased, but the statistical accuracy of the β-particle counting rate, obtained in a given counting period, was improved appreciably.

The β-counting rates, observed at various values of $H\rho$ in the range, were corrected for source decay, and then compared with the corresponding heights of the normalized momentum spectrum observed by Martin and Richardson[26]* with a fixed radius semi-circular focusing spectrometer. The factors by which the counting rates had to be multiplied to yield the height

* The original large scale plot of this momentum spectrum was kindly made available by Dr. H.O.W. Richardson, for this purpose.

of the normalized spectrum then gave a set of relative normalizing factors.

These factors, again adjusted to be relative to a factor of unity at 9 turns, are shewn on Figure 5.1. The effect of statistical errors in the counting rates are indicated.

This method, having been shewn to yield values for the normalizing factors in agreement with those of the previous method, was adopted to determine normalizing factors for other geometrical conditions of the spectrometer, to avoid frequent re-setting of the magnetic field.

§ 4. Further experimental check of the method of normalization.

To observe the entire continuous spectrum of $MsTh_2$, which extends to an $H\rho$ value of ~8800 oersted-cm., several different field settings were required. The fact that a smooth curve was finally obtained from the overlapping junctions of the portions of the spectrum focused by each field setting, provided a useful check of the accuracy of the method of normalization.

CHAPTER 6.

Preparation of Sources of Mesothorium 2.

§1. Chemical separation of mesothorium 2.

From a stock solution containing mesothorium 1 and its decay products, associated with an appreciable activity of radium and its daughter elements, the mesothorium 2 was extracted by a method based on that of Haissinsky[27]. Frequent separations were made, and it was found that more than 1 mC activity, due to $MsTh_2$, could be obtained from the solution some 24 hours after each extraction.

With as little as 0.015 mgm. of ferric hydroxide as carrier, the $MsTh_2$, with all decay products except ThX and Tn and Rn, was precipitated by neutralizing the stock solution (in hydrochloric acid) with ammonium hydroxide. The precipitate was filtered off, using a sintered glass filter, and after washing the residues, the filtrate of $MsTh_1$, Ra and ThX was acidified with hydrochloric acid and set aside for the re-growth of $MsTh_2$.

The residues were dissolved from the filter in dilute hydrochloric acid and ~1 mgm. of both lead and bismuth nitrates were added. Hydrogen sulphide was bubbled through this solution and the sulphide precipitate formed carried activities due to

polonium, bismuth, lead and thallium isotopes. After filtering and washing, the filtrate was boiled to remove any excess H_2S, and ~1 mg. of barium was added as hold-back carrier. The $MsTh_2$ and iron were reprecipitated by neutralizing the solution, and were removed by filtering. The filtrate and washings were kept to ensure no loss of $MsTh_1$ or Ra. Restoration to the stock solution of activity in these washings is described in §3. The residue of $MsTh_2$ (with carrier) was dissolved in 1N nitric acid and after evaporation to dryness, was taken up in the minimum quantity of N/10 nitric acid.

No attempt was made to separate radiothorium, although a method for doing so was available[28], since after the first extraction of $MsTh_2$ (which was not used as a source) the contamination due to RdTh resulting from ~24 hours growth was of negligible proportions.

The chemical separations were made in a fume cupboard. Lead screening was used for protection.

The $MsTh_2$ may equally well be carried with cerium, and in this case a method for obtaining carrier-free sources is outlined by Peterson[29]. The method was initially used, but was later abandoned in view of the very small weight of ferric chloride which proved to be effective.

Particular attention was paid to the cleanliness of the glassware as any dirt present greatly increased the quantity of material in the final source.

§2. Techniques for making sources.

To obtain sources suitable for use in the spectrometer from the final solution of $MsTh_2$ (with a small quantity of carrier) in nitric acid, the following general technique was adopted. The active material was taken up in a glass dropper, drawn out into a fine bore. The solution was then applied drop by drop to a ribbon of aluminium foil cut to the breadth of the final source. Each drop was evaporated to dryness under an infra-red lamp before the next drop was applied. It was found impracticable to reduce the breadth of the aluminium ribbon below 2 mm., otherwise the drops were not confined to the ribbon. This set the limit to the narrowness of the sources which could be made in this way.

When sources of this breadth were set at an emission angle of 45°, the effective breadth was reduced to 0.85 mm. at a radius of curvature of 3 cm. and 1.15 mm. at a radius of 6 cm. (cf. § 7 of Chapter 2). For coincidence studies with the spectrometer, sources of this breadth gave a satisfactory degree of resolution, together with an adequate solid angle (cf. §13.1, 13.2 and 13.3 of Chapter 2).

For the study of coincidences between internal conversion lines it is essential to minimize the amount of material present per $cm.^2$ of the source. Aluminium foil of thickness 0.2 $mgm./cm.^2$ was therefore

used to form the ribbon. The acid solution, which was necessary to dissolve the $MsTh_2$, was found to attack the thin foil, which was therefore supported on a collodion film. The length of the foil placed on the film was confined to 1 cm., this being the desired length of the final source (cf. §10.4, Chapter 2). It was found that only three drops of solution could be applied before the foil became so dissolved that the final source failed to conform with the original dimensions of the aluminium foil. Provided the solution applied was reduced sufficiently in volume, activities of ~1 mC were obtainable in three drops of the liquid. The total thickness of sources made in this way amounted to ~0.7 mg./cm.^{2}, after allowing for the increase in thickness due to the emission angle at which they were set. The collodion film was finally placed on to the rectangular source holder, described in §1 of Chapter 1, so that the source occupied a central position.

Whenever the requirement for sources on such a thin backing could be relaxed, (such as in coincidence studies between γ-rays, counted directly from the source, and the β-particles of the continuous spectrum at all but low energies) an aluminium ribbon of thickness 1 mg./cm.^{2} was used. This was stretched across the source holder, as illustrated in Figure 1.2of Chapter 1, petroleum jelly being used as the adhesive. Careful application

of the active drops ensured that the length of the source approximated closely to 1 cm. This thicker foil allowed the application of about twelve drops of active material before it was appreciably reduced in thickness by the acid solution, and sources of ~2 mC. strength were regularly obtained.

For detecting line positions with photographic plates (using only one half of the spectrometer), the drops were evaporated on to a loop of platinum wire of diameter 0.3 mm., bent into the shape of a hair pin. In this way narrower sources were obtained leading to increased resolution. The wire was straightened after the application of the drops and was then clamped into position in a source holder designed for the purpose.

§3. Treatment of the stock solution and restoration of active material.

It was found that after separating the $MsTh_2$ from the stock solution some 20 times, the ferric ~~chloride~~ hydroxide ceased to carry the activity efficiently. This was due to the excess of ammonium salts present. The volume of the stock solution moreover usually became inconveniently large at this stage (~5cc.) due to repeated additions of ammonium hydroxide in the chemical separation, and to subsequent addition of hydrochloric acid. To restore the solution to a small volume and to remove the excess ammonium salts, about 10 cc. of a saturated solution of ammonium carbonate was added to the stock solution previously neutralized with ammonium hydroxide. The insoluble barium carbonate, formed in this way, carried with it the $MsTh_1$ and Ra. After filtering and washing thoroughly, the residue was taken up in a small quantity of hydrochloric acid. The filtrate was discarded if it were found to possess no detectable activity, due to the growth of $MsTh_2$, after several days. If $MsTh_2$ activity were found to grow in the solution, it was added to the filtrate and washings from the separation of $MsTh_1$ and Ra from the final sources of $MsTh_2$.

These washings were found to possess considerable activity after repeated separations of $MsTh_2$. The

$MsTh_1$ and Ra, giving rise to this activity, were restored to the stock solution in the same way by addition of ammonium carbonate after reducing the volume substantially by evaporation.

CHAPTER 7.

An Investigation of the Spectrum of Mesothorium 2.

§ 1. The internal conversion lines.

Geometrical conditions of the spectrometer which lead to the relatively high degree of resolution required for the study of internal conversion lines have been discussed in §13.4 of Chapter 2. The source, of width 2 mm. and of length 1 cm. was set, at an emission angle of 45°, centrally beneath the source slit which was of width 4 mm. These conditions gave a theoretical ~~resolution~~ resolving power at a radius of 3 cm. of ~45, with a solid angle of 1/2000 of 4π, when a counter slit of length 1.5 cm. and width 1.5 mm. was used.

A survey was made of the spectrum from an $H\rho$ value of ~600 gauss-cm. to ~10,000 gauss-cm. using one half of the spectrometer. The counting rate for β-particles was found from the difference between the counting rates observed with the shutter C (of Figure 1.1) open, then with it closed. This rate was corrected for source decay. With sources of ~1 mC. strength, the accuracy in the β-particle rate was ~2% for counting periods of 40 sec.

It was confirmed that the strongest lines of the spectrum occur below an energy of 80 keV. It has been observed in Chapter 3, § 5, that the counters are

100% efficient only for incident β-particles of energies exceeding this value, and without a calibration of the counter efficiency at energies below 80 keV, any attempt to measure the intensities of the lines was precluded. Had the detector efficiencies been assessed, only a very rough estimate of the area under a line profile would have been possible, since conversion lines are broadened by the effective thickness of source material ($\sim$0.7 mg./cm.^{2}, including the weight of the dissolved aluminium backing, referred to in § 2 of Chapter 6) required to obtain sufficiently large counting rates. This, together with the scattered electrons from the box walls, causes considerable overlapping of the lines, and a spectrum consisting of peaks standing out from a high background was observed. It was impossible to assess the shape of the true β-particle continuous spectrum beneath these overlapping lines, without which the area under an individual line profile could not be estimated.

Typical curves obtained before normalization are shewn in Figures 7.1 and 7.2, for this low energy region.

Estimates of the intensities of these low energy lines were however made possible from the low energy region of the spectrum, recently observed at Edinburgh by Brodie using the lens spectrometer with a post-focusing accelerator, described by Butt.[30,31]

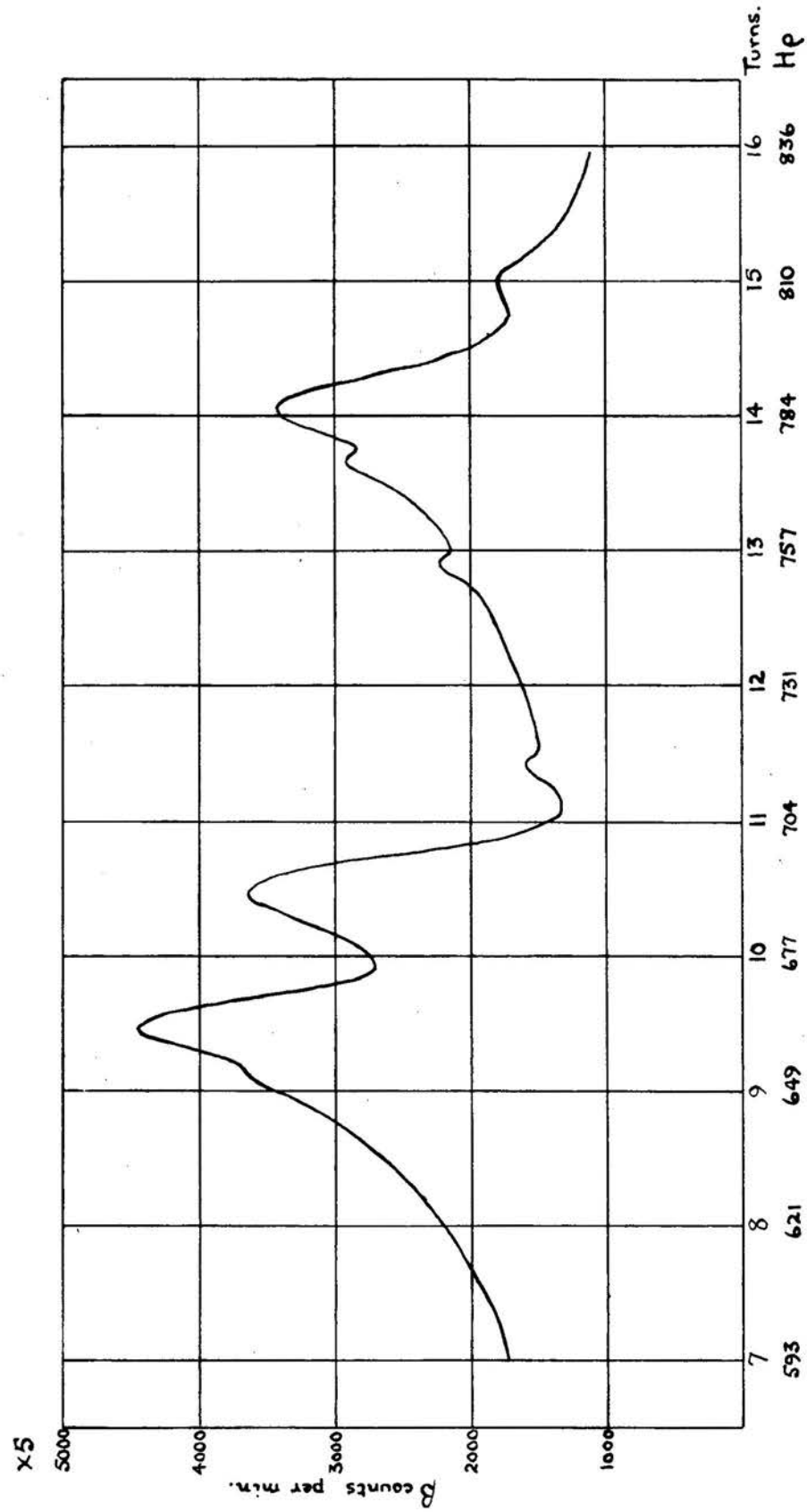

FIGURE 7·1

Low energy lines. $MsTh_2 \rightarrow RdTh.$

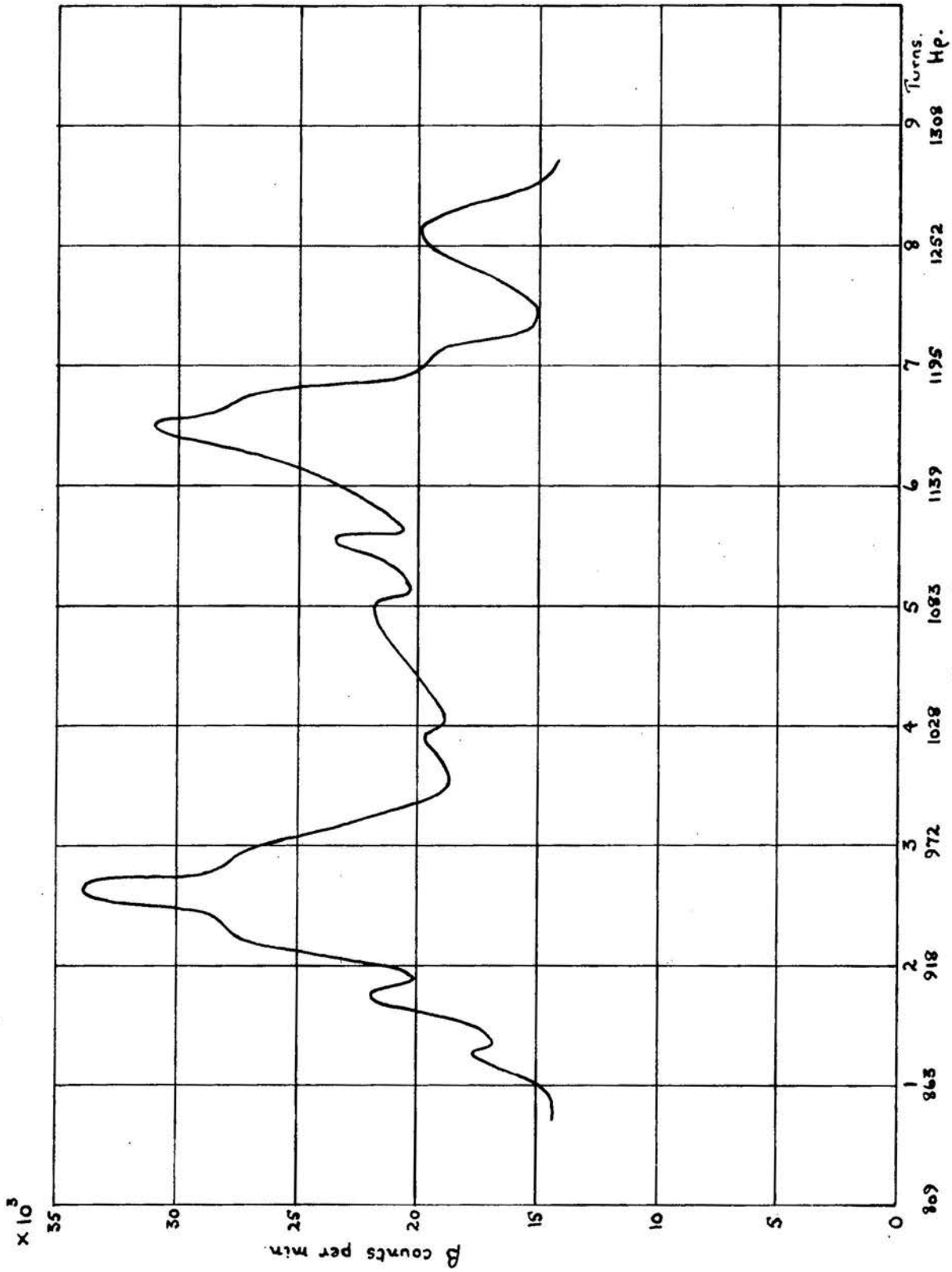

FIGURE 7·2

Further low energy lines. $MsTh_2 \rightarrow RdTh.$

This instrument focused electrons of energies up to ~ 300 keV only, but, with the larger transmission of a spectrometer of this type, weaker sources could be used. This, in turn, meant that the thickness of source material could be reduced to ~ 0.1 mg./cm.^{2}, in the case of $MsTh_2$. Corrections were made for back-scattering from the source backing, and for counter window absorption.

It will be shewn in § 5 that an estimate of the shape of the continuous spectrum of $MsTh_2$, shewn in Figure 7.9, may be made from the superposition of the observed partial spectra.

This estimate of the continuous spectrum was fitted to the region of the continuous spectrum observed by Brodie, and in this way the absolute intensities of the conversion lines were found.

The resolution of the lens spectrometer was not sufficiently high to allow the determination of the individual intensities of closely spaced lines. The results of the measurements are shewn in column 7 of Table 7.1. No estimate of the intensities of weak lines was attempted. Black's[4] values for the line intensities are shewn, for comparison, in column 6 of the table. These have been normalized to give the same intensities for the pair of lines at 948 and 977 gauss-cm., not resolved by the lens spectrometer.

Column 3 of Table 7.1 shews the $H\rho$ values for the lines observed with a counter in one half of

the double spectrometer. For the region of the spectrum above an energy of 80 keV, the multiplier voltage was chosen to be a little above that of the knee of the plateau of the counting rate/multiplier voltage characteristic for the lowest energy β-particles focused by the particular field setting.

For the investigation of the low energy region of the spectrum, a thin polycrystalline layer of anthracene was used (of ~20 mg./cm.^{2}) in order to minimize the background counting rate due to γ-rays. For those β-particles which were sufficiently energetic not to be absorbed by such a layer, a thicker single crystal of anthracene was used. Lead screening between the source and the detector was used to reduce the background counting rate due to γ-rays.

To reduce any error due to possible placing of the source in an off-central position, the line positions were again observed with the source frame rotated through 180°. The mean values of the appropriate representative points of the various lines (cf. § 8 of Chapter 2) were then used to evaluate the $H\rho$ values. The magnetic field setting was found from the mean of several fluxmeter deflections in the manner described in Chapter 4. Each portion of the spectrum was surveyed with at least four different sources, and weak lines were distinguished from statistical fluctuations

by detailed comparison of the spectra observed.

The first column of Table 7.1 shews the corrected* $H\rho$ values of Black[4], found using a semi-circular focusing spectrograph with photographic plates.

To determine the positions of the more intense low energy lines with greater accuracy, the lines of a source of thorium active deposit, on a platinum wire of 0.3 mm. diameter, were observed photographically using a plate with an emulsion thickness of 50 microns (Ilford type G5). With the same field setting, the lines due to $MsTh_2$, evaporated on a similar wire, were observed with a second plate.

The distance between the edge of the plate and the centre line of the source slit was accurately measured, and the distances of the various lines from that edge of the plate were then found by scanning the plate with the slit of a microphotometer (Hilger and Watts type H451). The mean values of four separate runs along the plate were used.

From the positions of the lines of thorium active deposit, the radii at which they were focused were calculated, and, assuming the lines to possess

---

* Black determined his field settings from the $H\rho$ values of the lines of Ra(B+C) observed by Ellis and Skinner[32]. Black's values have been altered to agree with the more recent measurements on Ra(B+C) by Ellis.[33]

the $H\rho$ values determined by Ellis[25], the magnetic field intensity was calculated.

From this field intensity the $H\rho$ values of the stronger lines of $MsTh_2$ were determined, and are shewn in column 4 of Table 7.1. Allowance was made for the manner in which the effective field intensity changed with radius (vide Chapter 4).

The energies corresponding to the $H\rho$ values of the lines are shewn in column 5. The $H\rho$ values determined photographically were used when available, otherwise the values of column 3 were taken.

TABLE 7.1.

Line. (1)	Hρ (Black). (2)	Hρ observed with counter. (3)	Hρ observed photographically. (4)	Energy. (keV). (5)	Black's intensities per 100 disintegrations. (6)	Intensities observed, per 100 disintegrations. (7)
1	-	652	-	36.34	-	
2	665	661	659	36.91	9.4	44
3	696	689	690	40.33	8.0	
4	-	715	-	43.14	-	Weak
5	-	750	-	47.28	-	Weak
6	-	776	-	50.47	-	Weak
7	790	787	789	52.16	6.1	15
8	816	816	815	55.41	4.2	
9	836	-	-	58.19	0.56	-
10	864	872	-	61.91	0.38	Weak
11	900	901	-	66.97	1.5	.1
12	-	929	-	71.03	-	Weak
13	946	949	948	73.76	4.7	8.0
14	975	976	977	77.98	3.3	
15	-	1017	1000	81.49	-	Weak
16	1069	1077	1072	92.66	1.5	1.3
17	-	1114	1099	97.04	-	
18	1162	1166	1166	108.1	3.3	5.6
19	1183	1182	1185	111.3	2.3	
20	-	1205	-	114.8	-	Weak
21	1248	1248	1247	122.2	2.1	1.8
22	1267	-	-	125.8	0.56	
23	1299	-	-	131.6	0.38	-
24	1336	1357	-	140.3	1.7	Weak
25	-	1376	-	145.8	-	Weak
26	-	1435	-	157.0	-	Weak
27	1459	1475	-	164.9	1.9	1.3
28	1528	1545	-	178.7	0.56	
29	1681	1660	-	202.4	1.5	Weak
30	-	1721	-	212.0	-	Weak
31	1770	1771	-	225.9	0.75	Weak
32	2081	2102	-	300.5	0.56	Weak
33	2159	2168	-	315.9	0.19	Weak
34	2303	2305	-	348.6	0.75	Weak
35	2663	-	-	437.0	0.38	-
36	2722	-	-	451.9	0.19	-
37	4012	4013	-	796.4	0.56	Weak
38	4214	4237	-	858.5	0.28	Weak
39	4347	4345	-	888.6	0.19	Weak
40	-	4475	-	925.1	-	Weak
41	4530	-	-	940.4	0.19	-
42	-	4689	-	985.1	-	Weak
43	6430	6406	-	1477	0.09	Weak
44	6564	6588	-	1530	0.09	Weak

§2. Analysis of the final portion of the continuous spectrum.

The results of preliminary studies of the final portion of the spectrum have already been published[34], and details of the two most accurate series of observations will now be given.

It is desirable to find a method for checking the value of the magnetic field, obtained from the fluxmeter deflection, for experiments on the end-point of a spectrum, and, in this case, the end-point of the β-particle spectrum of ThC provided a useful reference point for this purpose.

A source of thorium active deposit of dimensions 1 cm. by 2 mm. was prepared by exposing this area of a foil of aluminium of equivalent thickness 0.2 mg./cm^2, to a dry emanating preparation of RdTh. The activated foil was covered with a similar aluminium foil to prevent loss of atoms to the walls of the spectrometer box by α-particle recoil. With the magnetic field set to focus electrons of energies up to ~2.4 MeV, observations of the β-particle spectrum, above the end-point of ThC" (at 1.805 MeV), were commenced after the source had attained transient equilibrium; corrections for source decay could then be made using the decay constant for ThB.

For these observations, together with those using $MsTh_2$ yet to be described, the spectrometer geometry was the same as that of § 1. An anthracene crystal of thickness ~5mm. was used.

Counting rates were taken with the shutter C, of Figure 1.1, open and with it closed, the difference between these readings giving the counting rate for β -particles only. Corrections were made for source decay, and in addition a small constant deduction was made from the observed counting rates to allow for scattering of β-particles into the detector from the spectrometer box. That scattering was, in fact, present was shewn by the persistence of a small and almost constant β-particle counting rate beyond the end-point of ThC up to the on-set of the X-line at 10,000 $H\rho$. The average value of this rate was used for the correction mentioned.

The experiment was repeated with the source rotated through 180° to correct for non-central source mounting.

The corrected β-particle counting rates were normalized (cf. Chapter 5), and a Fermi diagram, shewn in Figure 7.3(a), plotted for each set of observations. The extended tables of Fermi functions*,

---

* Issued in 1952 by the National Bureau of Standards.

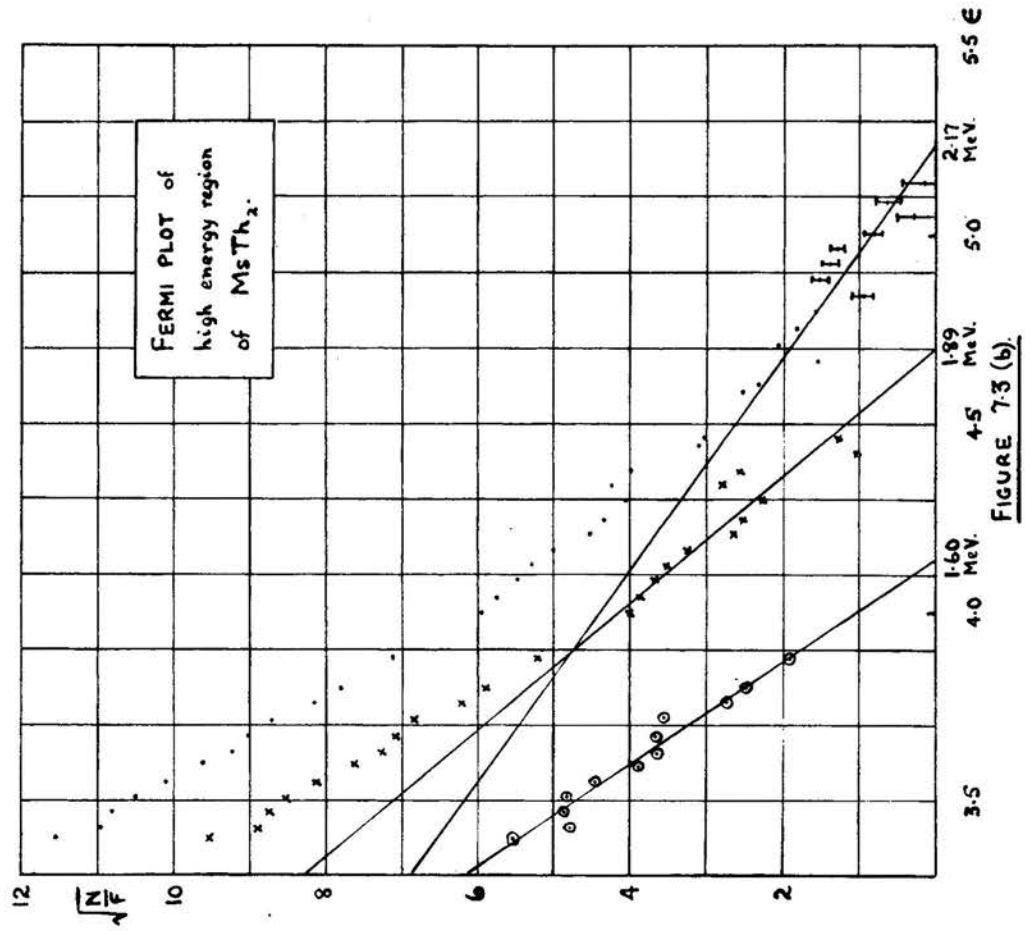

FIGURE 7·3 (b).

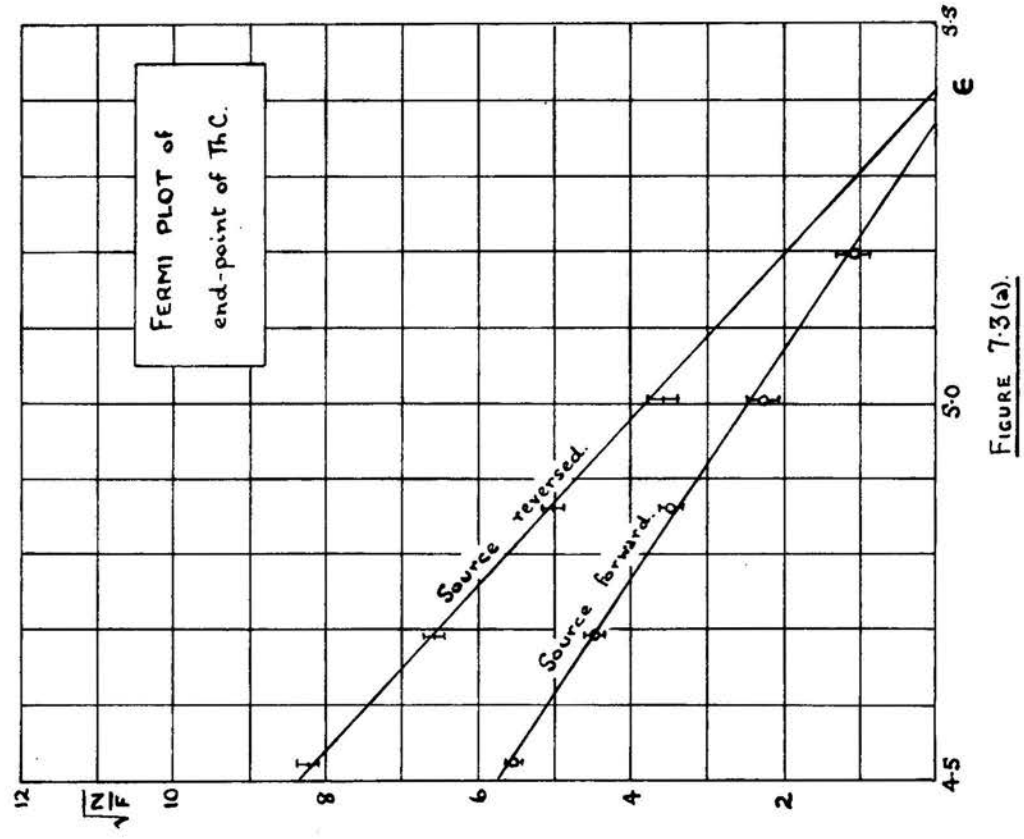

FIGURE 7·3 (a).

referred to by Feister[35], were used throughout. Straight lines were fitted to these diagrams by the method of least squares. The mean $H\rho$ value corresponding to the two end-points given by this analysis was compared with the $H\rho$ value for the end-point of ThC, corresponding to an energy of 2.256 MeV, which was obtained by Feather, Kyles and Pringle[2].

The estimate of the intensity of the magnetic field obtained from the fluxmeter deflection was then adjusted slightly to produce agreement between these $H\rho$ values.

With this field setting the spectrum of $MsTh_2$ was observed over the range of electron energies focused. Corrections for the background counting rate due to γ -rays and to photomultiplier noise, for source decay (assuming the half-value period to be 6.13 hours[36]), and for scattering of electrons beyond the end-point, were made as before.

The results, after normalization, were plotted on a Fermi diagram shewn in Figure 7.3(b). The curve obtained was analysed into the three straight lines shewn, which gave a final end-point at an energy of 2.17 MeV, with partial spectra possessing end-points at energies of 1.89 and 1.61 MeV.

The straight lines were again fitted by the method of least squares. By fitting straight lines,

it is implied that the spectra possess allowed shapes. The correction factors for forbidden spectra, given by Konopinski and Uhlenbeck[37], did not alter the linearity of the curves, over the range of energies involved, sufficiently to change the analysis significantly.

Due to the limited source strength available, and to the fairly short half-value period of $MsTh_2$, a second series of observations over this range of energies (extending upwards from ~1.2 MeV) could not be made with the source frame rotated through 180°, without a considerable reduction in the statistical accuracy of the observations.

To improve the accuracy of the value for the end-point of the spectrum, the counting rates over a smaller energy range, confined to the region above ~ 1.7 MeV, were therefore observed. A second series of observations was taken with the source frame reversed, to correct for possible errors due to non-central source mounting. The magnetic field was determined, as in the previous experiment, from a Fermi plot of observations on ThC which is shewn in Figure7.4(a). Figure 7.4(b) shews the Fermi diagram for $MsTh_2$, in which a single straight line has been fitted to the points obtained with the two source positions. An end-point at an energy of 2.18 MeV was given by this analysis. The existence of a partial spectrum with

an end-point at an energy of 1.88 MeV was also shewn.

With this field setting, observations of the spectrum below an energy of ~1.90 MeV were then made with a freshly prepared source. The Fermi diagram was drawn (Figure 7.4(c)) and, by assuming the end-point to be at an energy of 2.18 MeV, the final linear portion of the Fermi plot of the spectrum was inferred. Analysis of the Fermi diagram into linear components, shewed partial spectra with end-points at energies of 1.85 MeV and 1.70 MeV.

Finally a survey of the spectrum was made, at fairly widely spaced intervals, from an energy of ~1.90 MeV down to an energy of ~275 keV, all the observations being made with the one source. Below this energy, strong internal conversion lines are found. The observed points of the spectrum, after application of the corrections for background counting rates and for source decay, were normalized, and are shewn in Figure 7.9. The shape of the spectrum suggests the existence of at least one other partial spectrum with an end-point at ~1.2 MeV.

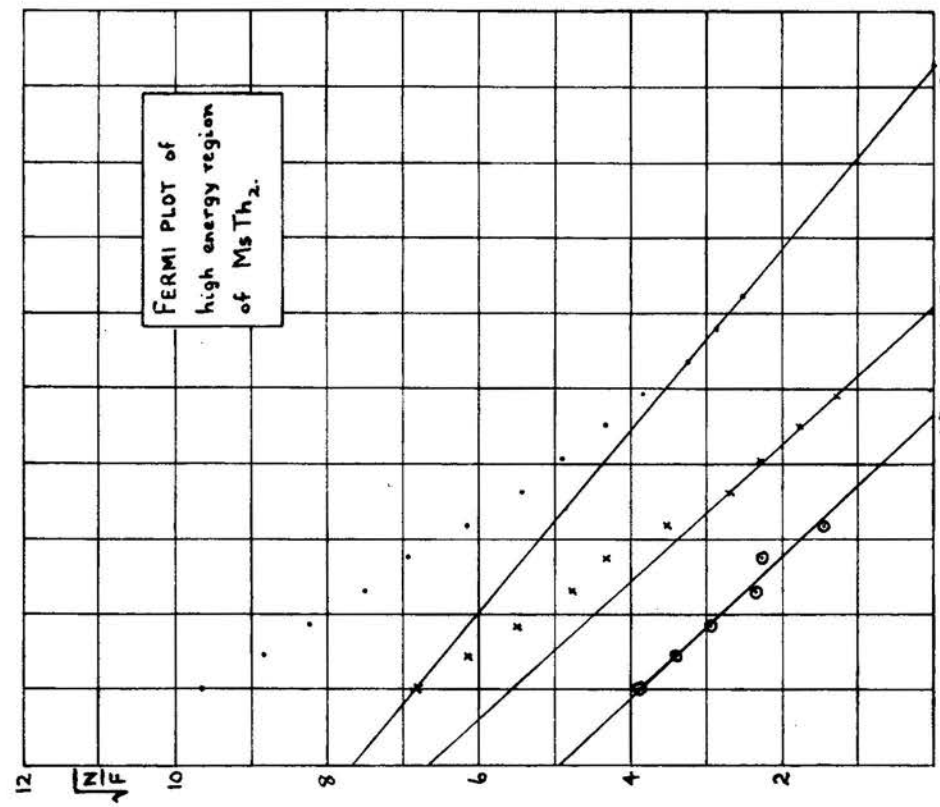

FIGURE 7·4(c).

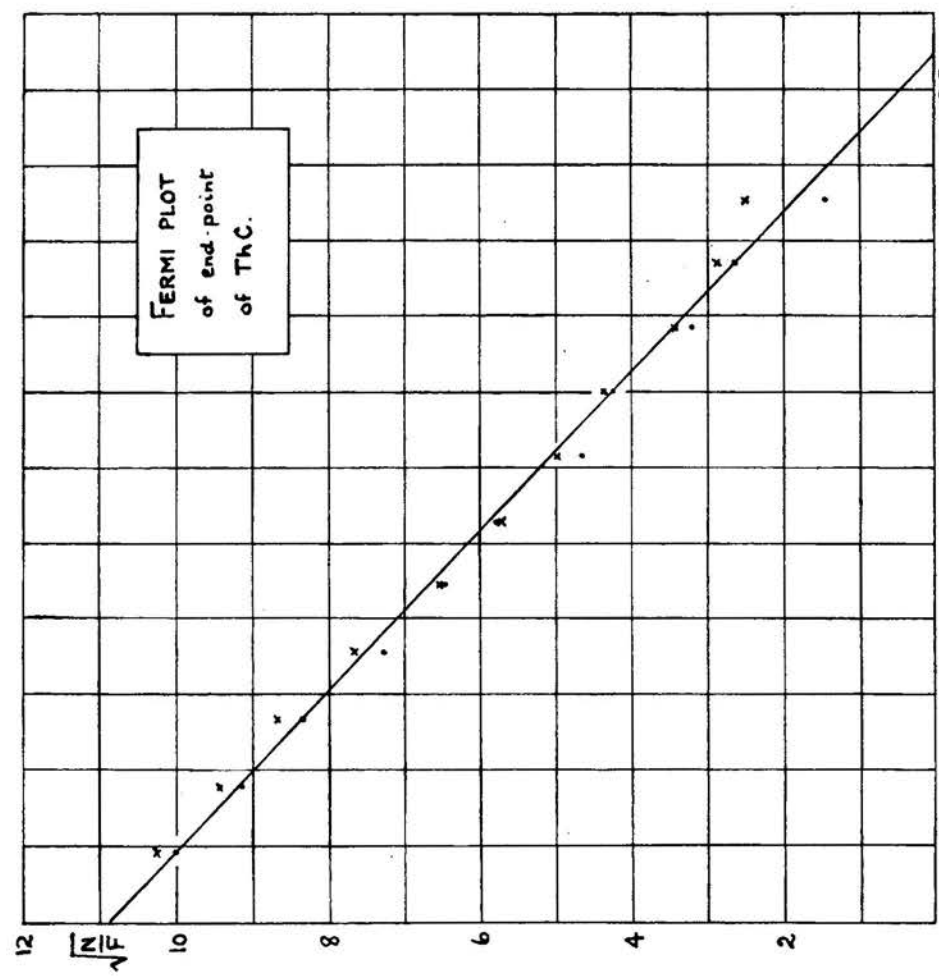

FIGURE 7·4(a).

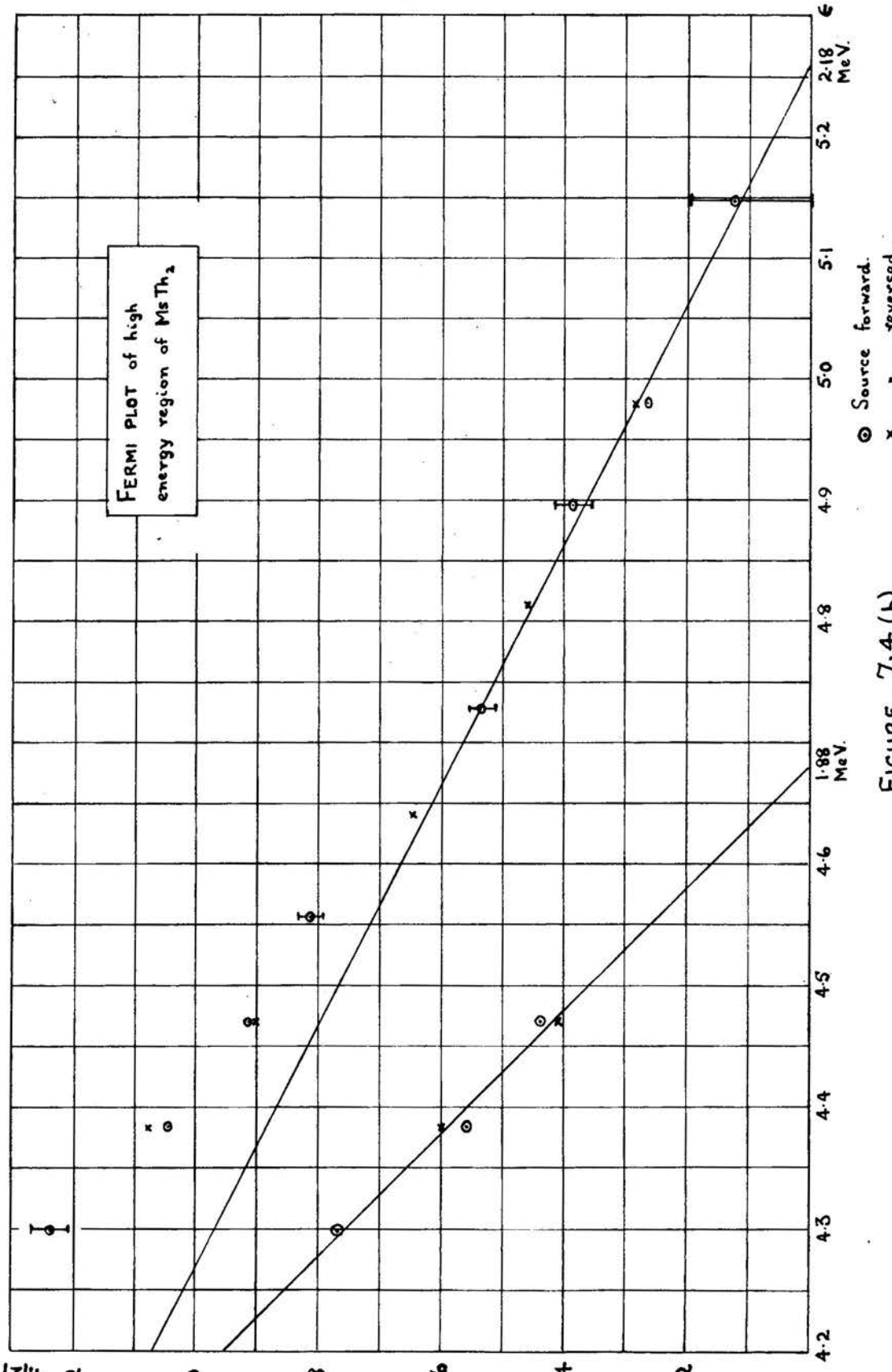
FERMI PLOT of high energy region of MsTh2
√N/F
12
10
8
6
4
2
4·2
4·3
4·4
4·5
4·6
1·88 MeV.
4·8
4·9
5·0
5·1
5·2
2·18 MeV.
E
⊙ Source forward.
× - reversed.

FIGURE 7.4 (b).

§3. Checks on the purity of the sources.

With the source strengths used in these and in later experiments, a single source of $MsTh_2$ could, in general, only be used for work on the spectrum during the day on which it was extracted, otherwise long counting periods would have been necessary to obtain the desired statistical counting accuracy. On frequent occasions, however, observations of the particular portion of the spectrum under investigation were repeated during the following morning, before replacement of the source, in order to check the decay of the source over periods of ~2 half-lives. In all cases the counting rates agreed with those calculated, assuming a 6.13 hour half-life, to within ~2% providing a useful check on the purity of the sources extracted. Moreover, on no occasion was evidence found of the strong F line of ThB → C or of the strong, F, G and H lines of RaB → C.

§4. β-γ coincidence studies.

To investigate further the existence of partial β-particle spectra, and, in particular, to search for less energetic components than those already observed, coincidence techniques were applied.

One counter was set as close to the source as possible to count the γ-radiations directly from the source. The β-particles were screened from this counter with a shutter covering the source slit. By adjusting the voltage on the multiplier, only those γ-rays above a certain minimum energy, chosen from the calibration curve of Figure 3.4, were detected. The same anthracene crystal, of thickness ~5mm., previously used to obtain this calibration curve, was used with the γ-counter.

The second counter was used to scan the continuous β-ray spectrum, and for this purpose a source slit of 8mm. width was used, with a counter slit of width 5mm. The source, placed at an emission angle of 45°, was off-set from its central position towards the image by half its effective width. In this way the solid angle for β-particles subtended at the source by the slit of the β-particle detector was made comparatively large, (cf. §13.2 of Chapter 2). An anthracene crystal of thickness ~5mm. was used with the β-particle detector.

With the voltage of the γ-counter set to the highest usable value, making the counter sensitive to γ-rays of energies greater than ~ 50 keV, genuine coincidences were recorded with β-particles of energies up to 1.83 MeV only. Observations were simultaneously made at resolving times of 10^{-8} sec. and 10^{-7} sec. Although only those readings obtained with the shorter resolving time were analysed, the number of genuine coincidences obtained with the longer resolving time was not significantly different from that given with the shorter resolving time at any setting of the β-particle detector. At each β-particle detector setting an observation was made to give the γ-γ background coincidence counting rate, the shutter C (of Figure 1.1) being lowered. After making the necessary corrections to these observations for decay of the source, the genuine γ-γ coincidence rate was subtracted from the genuine counting rate observed with the shutter raised. The genuine β-γ coincidence counting rates, thus obtained, were normalized, using the factors appropriate to this geometry of the spectrometer, and were plotted, as shewn in Figure 7.5, on a Fermi diagram. The straight line, fitted by least squares, indicates an end-point at an energy of 1.83 MeV. Although the same value was found on repeating the experiment, no great reliance can be placed on the value for this end-

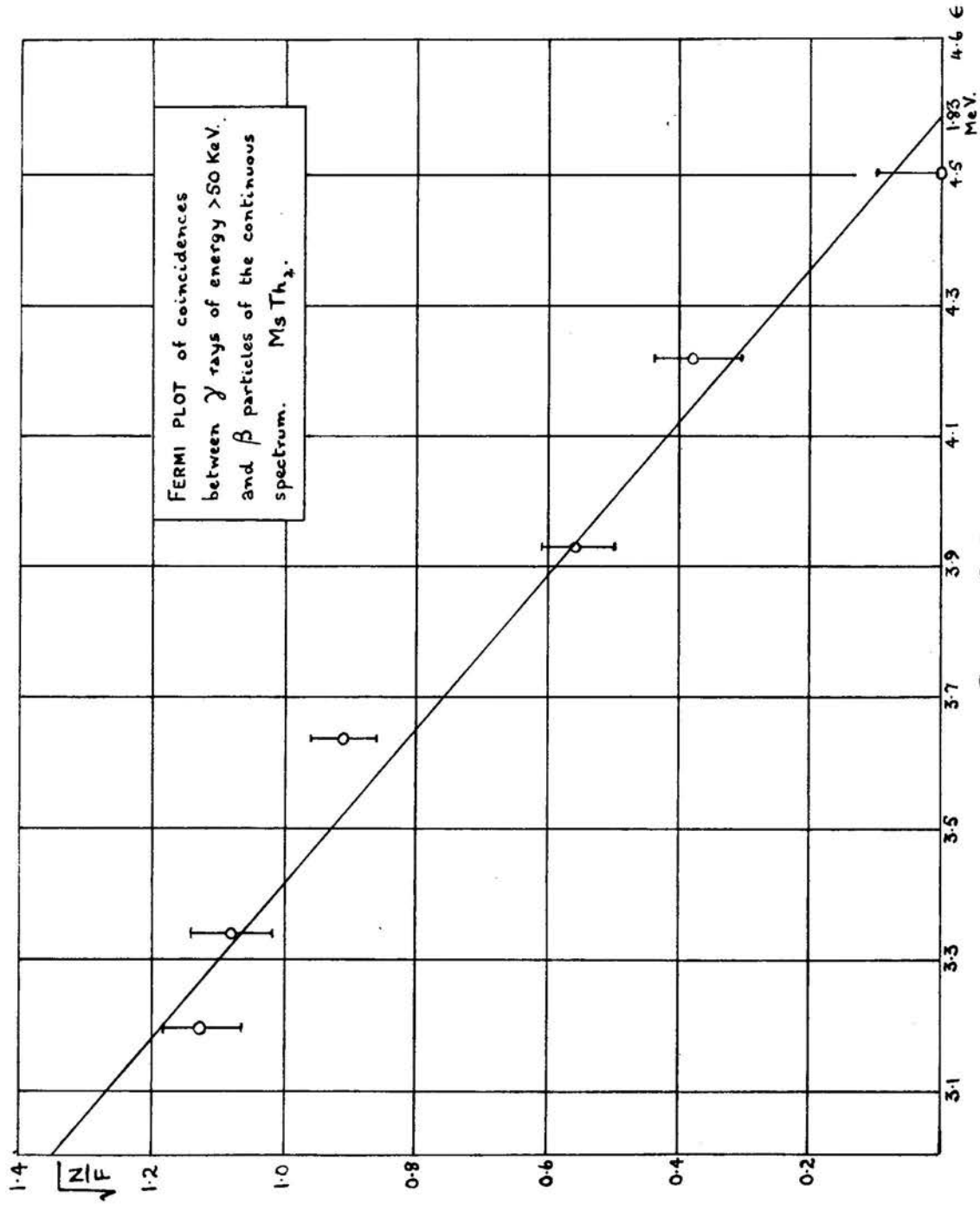
FERMI PLOT of coincidences between γ rays of energy >50 KeV. and β particles of the continuous spectrum. Ms Th2.
N/F
1·4
1·2
1·0
0·8
0·6
0·4
0·2
3·1
3·3
3·5
3·7
3·9
4·1
4·3
4·5
1·83 MeV.
4·6 ε

FIGURE 7·5

point since the statistical errors were large, due to the small number of β-particles counted, and to the relatively high γ-γ background coincidence rate. For these reasons it was not expected that the two partial spectra with end-points at energies of 1.85 and 1.70 MeV, suggested by the experiments with a single counter, would be resolved.

On lowering the voltage to make the γ-counter sensitive to radiations of energies greater than $\sim$900 keV, β-γ coincidences were recorded for β-particles of energies up to $\sim$1.1 MeV only. Due to the relatively large number of β-particles emitted in this energy region by the source, the statistical accuracy of the β-γ coincidence counts, after correcting for γ-γ coincidences (in the manner of the former experiment), was higher. A Fermi plot, shewn in Figure 7.6, was made, and on analysis into components of allowed shape, end-points of partial spectra were given at energies of 1.11, 0.64 and 0.45 MeV.

On an earlier occasion a similar experiment gave partial end-points at energies of 1.14 and 0.60 MeV. A partial spectrum with an end-point at 0.45 MeV was not resolved, but only four experimental observations were made in this energy region. The Fermi plots are shewn in Figure 7.7.

The relative intensities of these partial

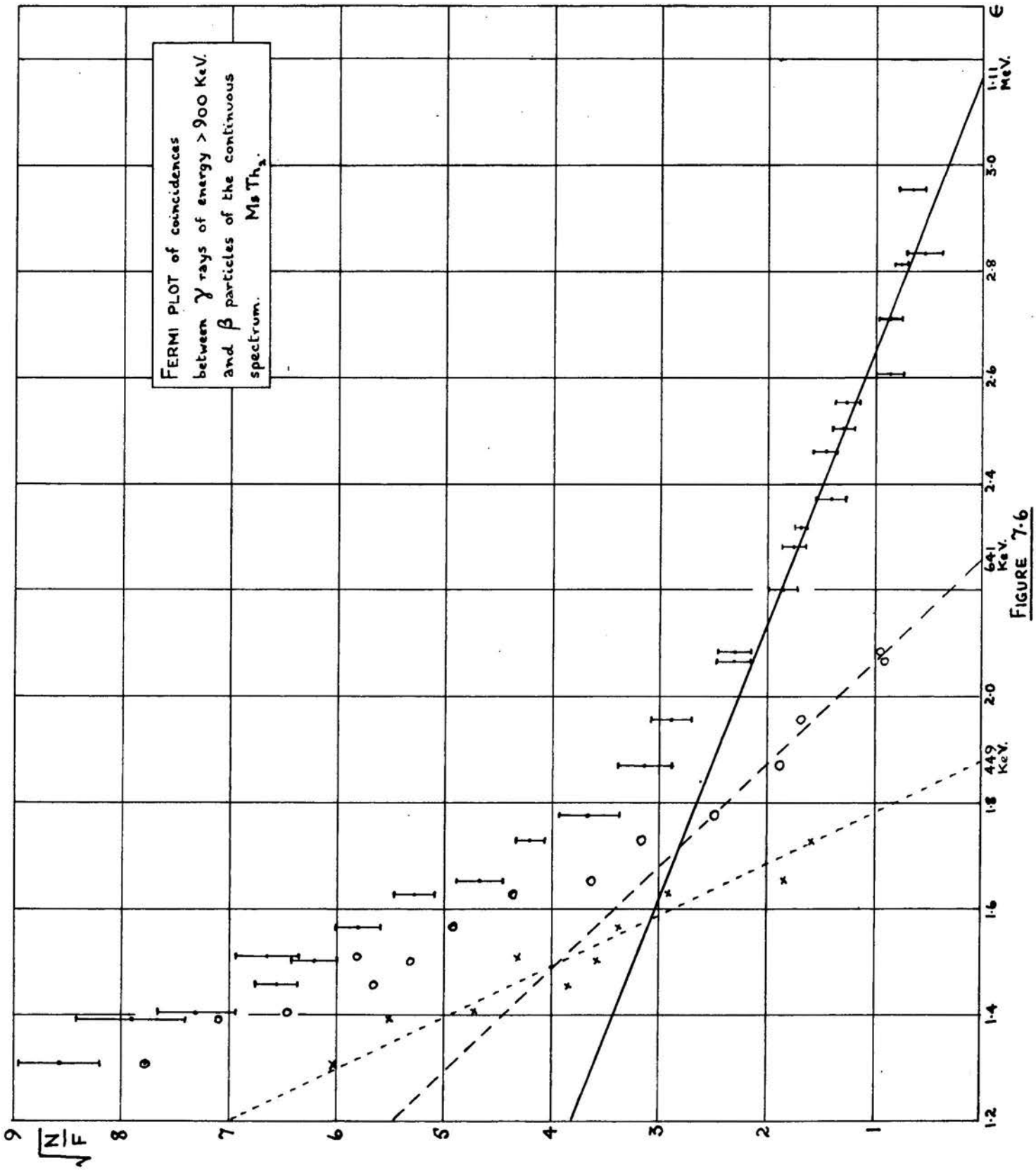
FERMI PLOT of coincidences between γ rays of energy > 900 KeV. and β particles of the continuous spectrum. MsTh2.
N/F
ε
1·11 MeV.
641 KeV.
449 KeV.
9
8
7
6
5
4
3
2
1
1·2
1·4
1·6
1·8
2·0
2·4
2·6
2·8
3·0

FIGURE 7·6

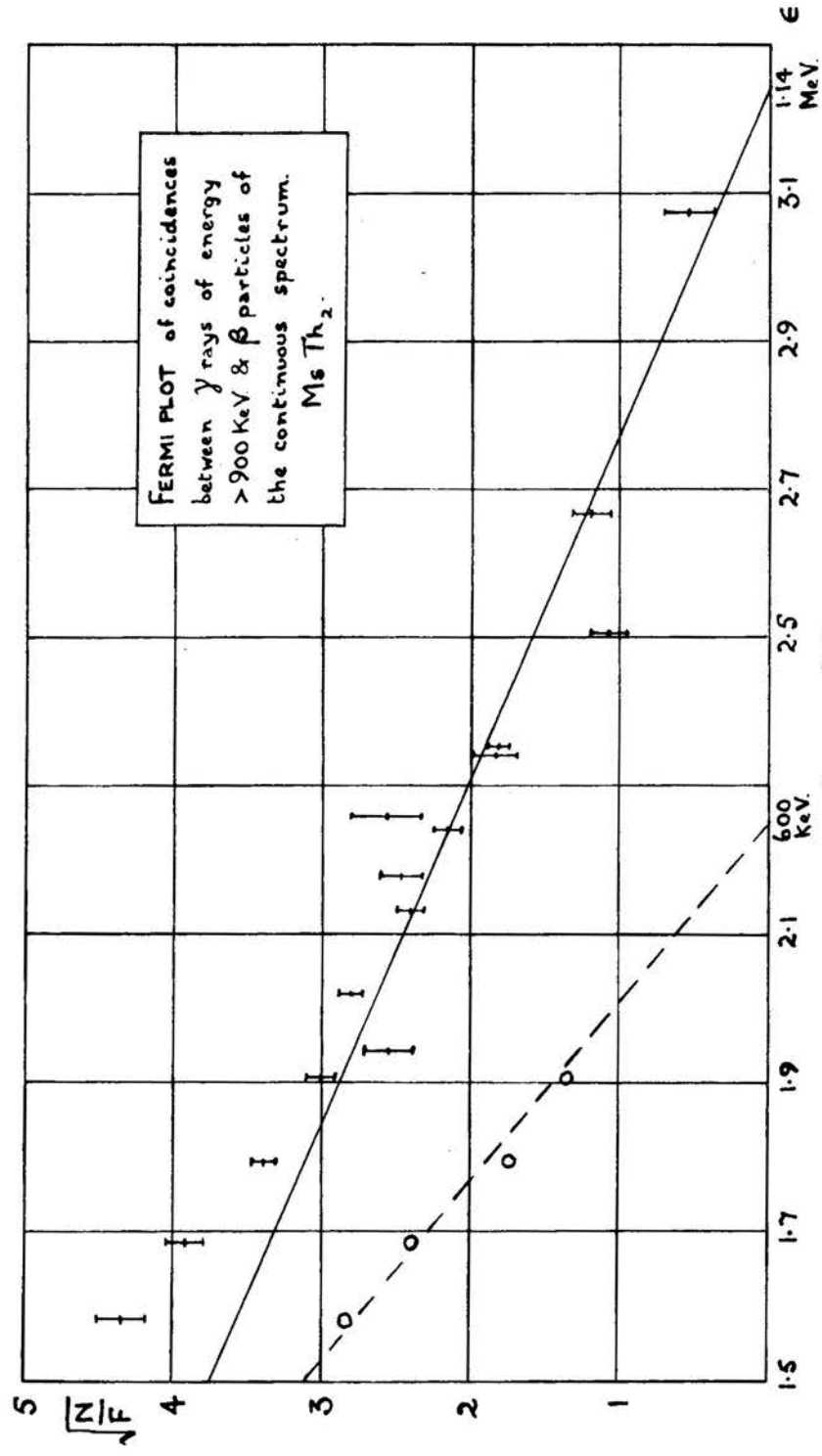
FERMI PLOT of coincidences between γ rays of energy >900 KeV & β particles of the continuous spectrum.
Ms Th2.
N/F
5
4
3
2
1
1·5
1·7
1·9
2·1
600 KeV.
2·5
2·7
2·9
3·1
1·14 MeV.
ε

FIGURE 7·7.

spectra cannot be deduced from the relative slopes of the Fermi lines, since it is unlikely that the β-particles of each partial spectrum will be in coincidence with the same γ-radiations of energy greater than $\sim$ 900 keV. That this conclusion is valid was shewn by reducing the voltage of the γ-counter still further, so that only radiations of energies exceeding ~1.1 MeV were counted. Coincidences between β-particles and these γ-rays now disappeared at a β-particle energy between 0.6 and 0.7 MeV. Statistical errors in this case were again large, due to the small γ-counting rate, and no great reliance can be placed on the end-point of 658 keV obtained from the Fermi plot shewn in Figure 7.8. An end-point at ~450 keV was not resolved from these observations. This may be due to the large statistical errors involved but could be accounted for by postulating that the level of the RdTh nucleus fed by the spectrum with an end-point at ~450 keV is not de-excited by a γ-ray of energy greater than 1.1 MeV.

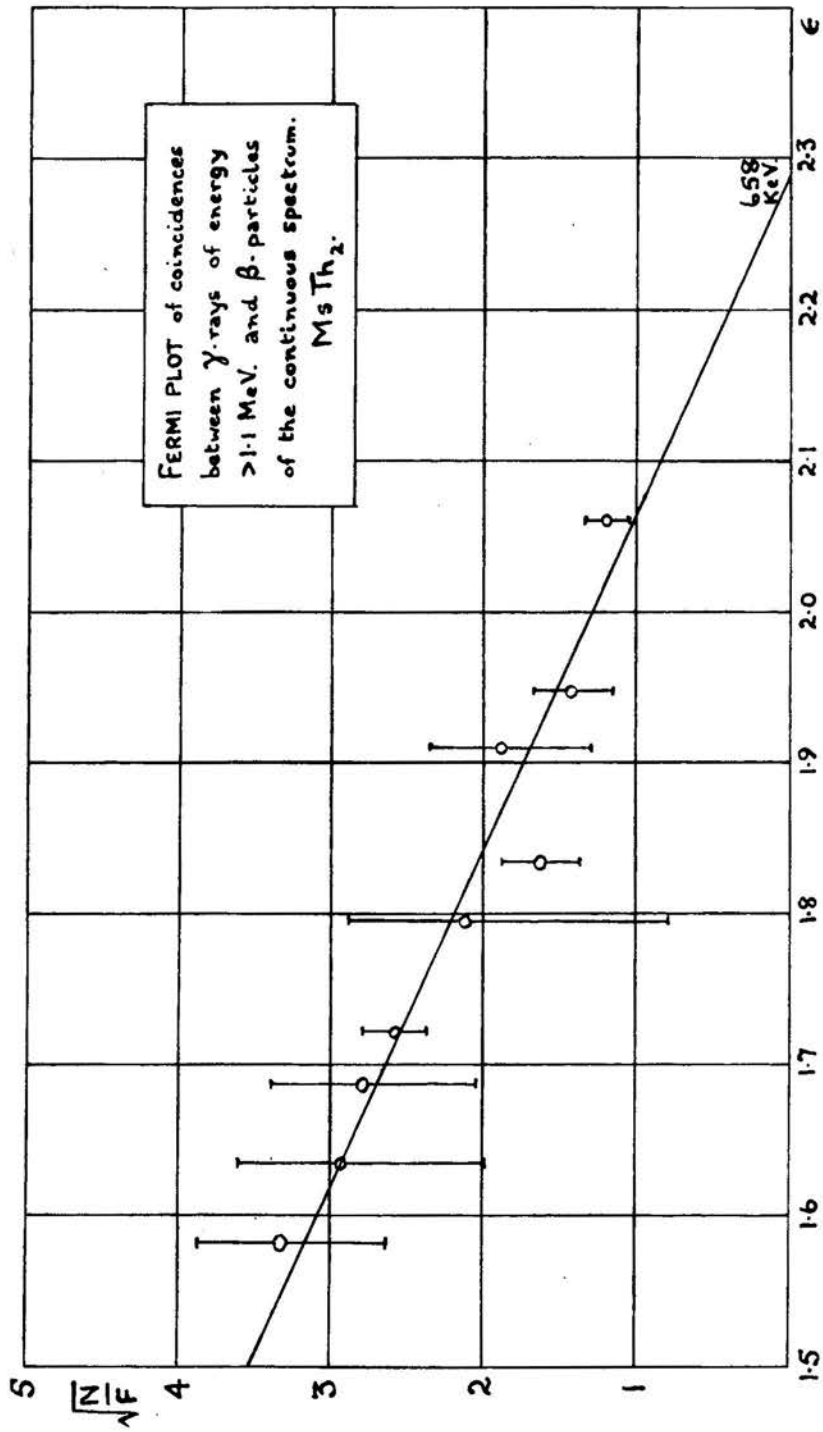
FERMI PLOT of coincidences between γ-rays of energy >1·1 MeV. and β-particles of the continuous spectrum.
Ms Th2.
658 KeV
N/√F
5
4
3
2
1
1·5
1·6
1·7
1·8
1·9
2·0
2·1
2·2
2·3
ε

FIGURE 7·8

§ 5. Further deductions from the β-γ coincidence experiments.

Apart from establishing end-points of component spectra, the β-γ coincidence experiments shew other features of the disintegration of $MsTh_2$ which are summarized below.

(i) No γ-rays, with a half-life of less than 10^{-7} sec. follow the partial spectrum with an end-point at 2.18 MeV.

(ii) The γ-rays which de-excite the states of the daughter nucleus ($^{228}_{90}$RdTh), fed by partial spectra with end-point energies of 1.85 and 1.70 MeV, are of energy not greater than~900 keV.

(iii) De-excitation of the state fed by the partial spectrum with an end-point at 1.11 MeV involves either one, or more γ-rays of energy between~0.9 and ~1.1 MeV, but does not involve γ-rays of energy exceeding ~1.1 MeV.

(iv) De-excitation of the states fed by the partial spectrum with an end-point at ~640 keV (and possibly the state fed by the partial spectrum with an end-point at ~450 keV) involves one or more γ-rays with energy exceeding ~1.1 MeV.

§6. The relative intensities of the partial spectra observed.

The relative intensities of the partial spectra with end-point energies at 2.18, 1.85 and 1.70 MeV were deduced from the relative slopes of the component lines of the Fermi plots of Figure 7.4(c), the spectra being assumed, for this purpose, to possess allowed forms. With a knowledge of an end-point and the slope of a line of the Fermi diagram, a value of the β-particle counting rate may be computed at any desired $H\rho$ value. In this way, these three momentum spectra were constructed and the ratio of the areas enclosed by each curve was then proportional to the relative intensities of the three modes of β-disintegration.

Since each partial spectrum, found by coincidence studies, may not be followed by the same γ-radiations, this method cannot be adopted to determine the relative intensities of the lower energy components, using Fermi plots such as those of Figure 7.6. The intensities of these less energetic partial spectra, relative to those already determined, were found by a detailed examination of the normalized momentum spectrum, observed with a single source, and illustrated in Figure 7.9.

The final portion of the sum of the component momentum spectra with end-points at 2.18, 1.85 and 1.70 MeV was fitted to the high energy tail of this observed

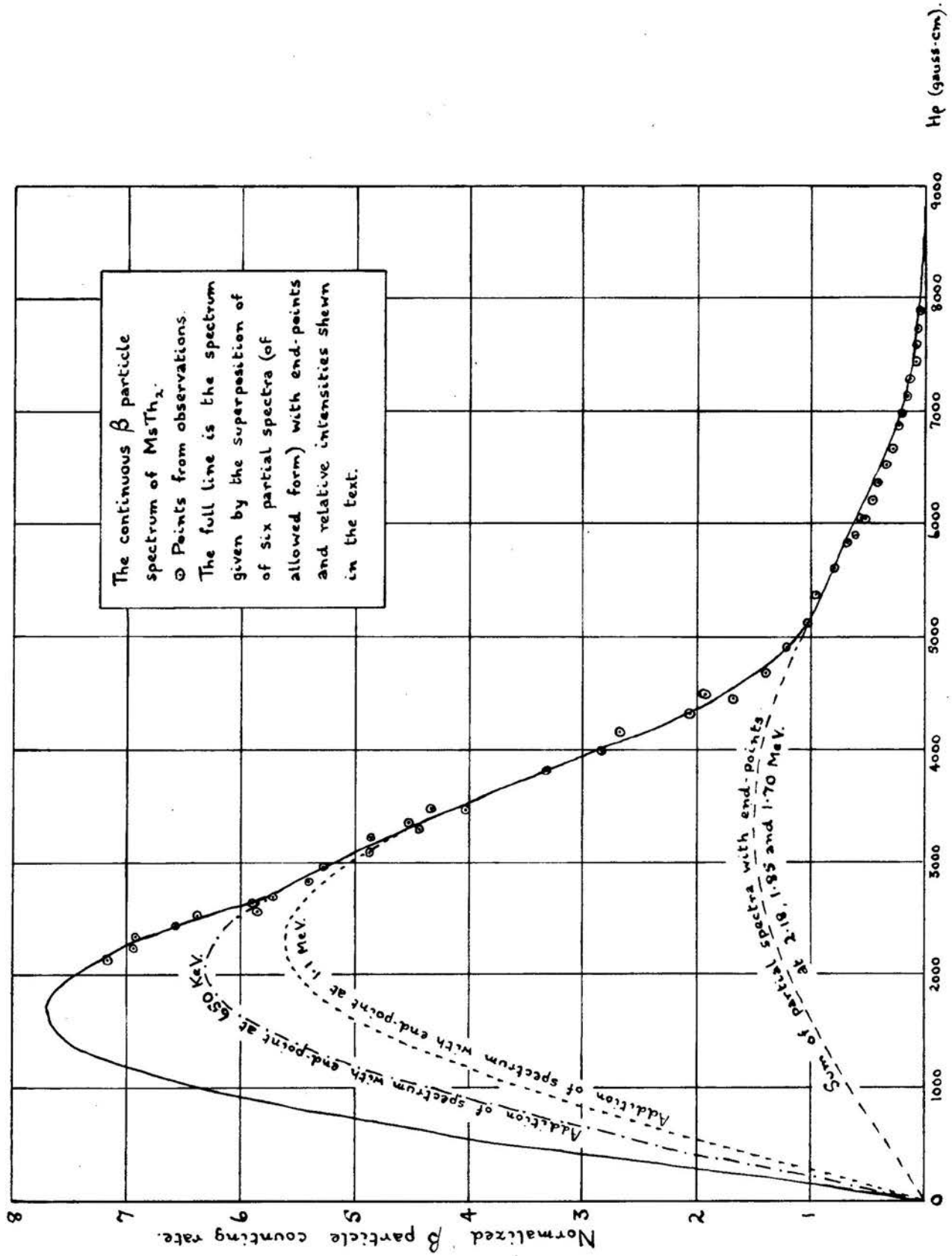
The continuous β particle spectrum of MsTh2.
⊙ Points from observations.
The full line is the superposition of six partial spectra (of allowed form) with end-points and relative intensities shewn in the text.
Addition of spectrum with end-point at 50 KeV.
Addition of spectrum with end-point at 1·1 MeV.
Sum of partial spectra with end-points at 2·19, 1·85 and 1·70 MeV.
Normalized β particle counting rate.
Hρ (gauss-cm).
0
1000
2000
3000
4000
5000
6000
7000
8000
9000
1
2
3
4
5
6
7
8

FIGURE 7.9

spectrum. The relative intensities of the three components already calculated were now modified by multiplication by the constant factor required to fit the calculated ordinates of the three component spectra to the observed spectrum.

Although accounting for all the high energy disintegrations the sum of these three components clearly only explained a small proportion of the disintegrations of energies up to ~1.2 MeV, and those disintegrations not yet included were found from the differences between the two curves.

A Fermi plot of these excess disintegrations was constructed (Figure 7.10)* and was found to possess a linear final portion with an end-point at 1.09 MeV, shewing good agreement with the partial end-point of 1.11 MeV from β-γ coincidence studies.

Assuming an allowed shape for this component, the partial momentum spectrum was constructed using the slope of the Fermi diagram, and its area gave the intensity of this component relative to the intensities of the partial spectra already found.

The remaining excess β-particle counts observed, after deducting those of this partial spectrum,

---

* The Fermi plot was based on the information obtained by drawing a smooth curve through the observed points. Elsewhere the observed points themselves were used.

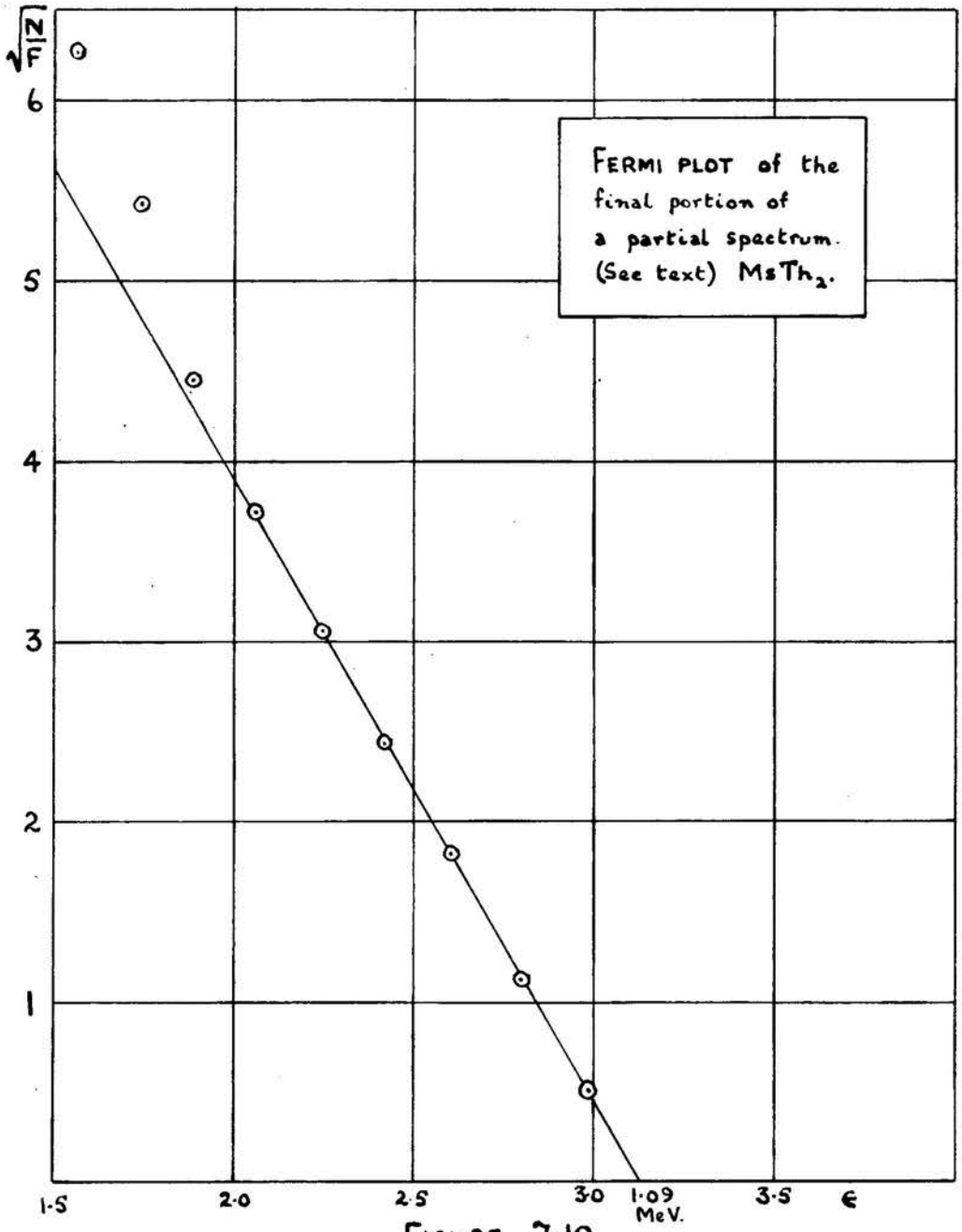

FIGURE 7·10

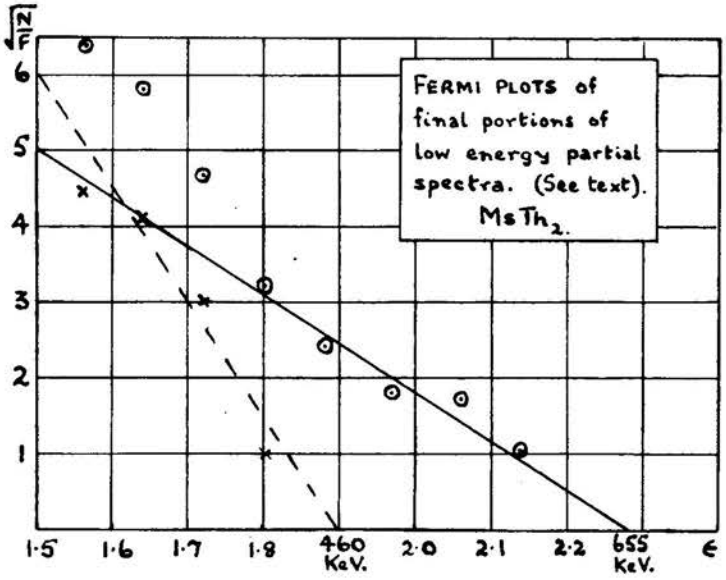

FIGURE 7·11.

was again found, and used to construct a further Fermi diagram (Figure 7.11). This again shewed linearity in its final portion, with an end-point at an energy of 655 keV (cf. 641, 600 and 658 keV of the β-γ coincidence studies). The intensity of this component was given by finding the area enclosed by the calculated spectrum, again assuming it to possess an allowed form.

It was found that the remaining β-particle counts of the observed spectrum could be accounted for by a sixth component (shewn in Figure 7.11) with an end-point in the region of 460 keV (cf. ~450 keV of a β-γ coincidence experiment).

The line, of Figure 7.9, shews the disintegration spectrum produced by the sum of these six component spectra, possessing relative intensities calculated in this way whereas the points marked are those found experimentally.

A summary of these intensities is given in Table 7.2, together with the decay constants of each component, calculated by assuming the lifetime of $MsTh_2$ to be 6.13 hours.

TABLE 7.2.

End-point of partial spectrum. (MeV.) (1)	Relative intensity. (%) (2)	Decay constant, λ. (sec^{-1}). (3)
2.18	10	3.14×10^{-6}
1.85	9	2.83×10^{-6}
1.70	7	2.20×10^{-6}
1.11	53	16.65×10^{-6}
0.64	8	2.51×10^{-6}
0.45	13	4.08×10^{-6}

§7. Coincidences between γ-radiations and internal conversion electrons.

Only the more intense electron lines may be studied in experiments of this type, without excessively long counting periods, owing to the presence of a considerable background of coincidences between the electrons of the continuous spectrum and the γ-rays.

For the β-particle counter, a source slit of 7 mm. width was used, with a counter slit of 1.5 mm. width. Sources of 2 mm. width were set centrally beneath the source slit at an emission angle of 45°. In this way, an adequately large solid angle for collection of electrons was obtained, without undue loss in resolution (cf. §13.3 of Chapter 2). The closely spaced lines were, in several instances, only partially separated but, fortunately, in most cases the overlapping lines were assigned to the conversion of the same γ-ray in different shells.

The γ-counter was set as close to the source as possible, and the voltage applied to the multiplier was selected to make the counter sensitive only to rays above a certain energy, chosen from the calibration curve of Figure 3.4. The more intense lines superimposed on the continuous spectrum were scanned with the β-particle counter and coincidences were recorded at resolving times of both 10^{-8} sec. and 10^{-7} sec. After correcting for accidental coincidences, the genuine

coincidence rate was divided by the corresponding γ-count for the observation. In this way correction for source decay was made, and furthermore an indication was given of the relative importance, in producing coincidences, of the additional energy range of γ-rays included when the multiplier voltage was progressively increased.

In all, three multiplier voltage settings were used, to select γ-rays of energies greater than ~900 keV, ~400 keV and ~50 keV.

The results of these experiments are shewn in Figure 7.12, in which the normalized shape of the spectrum observed with the β-particle counter is given together with the corresponding plots of the β-γ coincidence rates (taken at a resolving time of 10^{-8} sec.), per γ count recorded. The less exact results of observations with the 10^{-7} sec. resolving time are not shewn, as they only served to confirm the results presented.

To discuss the features shewn by this figure, the assignment of the conversion lines involved, to radiations of various energies, summarized in Table 8.1 below, is anticipated. Notable features are then:-

(1) The γ-ray of energy 57 keV which is converted in the L_{II} and L_{III} shells to give the unresolved lines at 660 and 690 gauss-cm., and in the M and N shells to

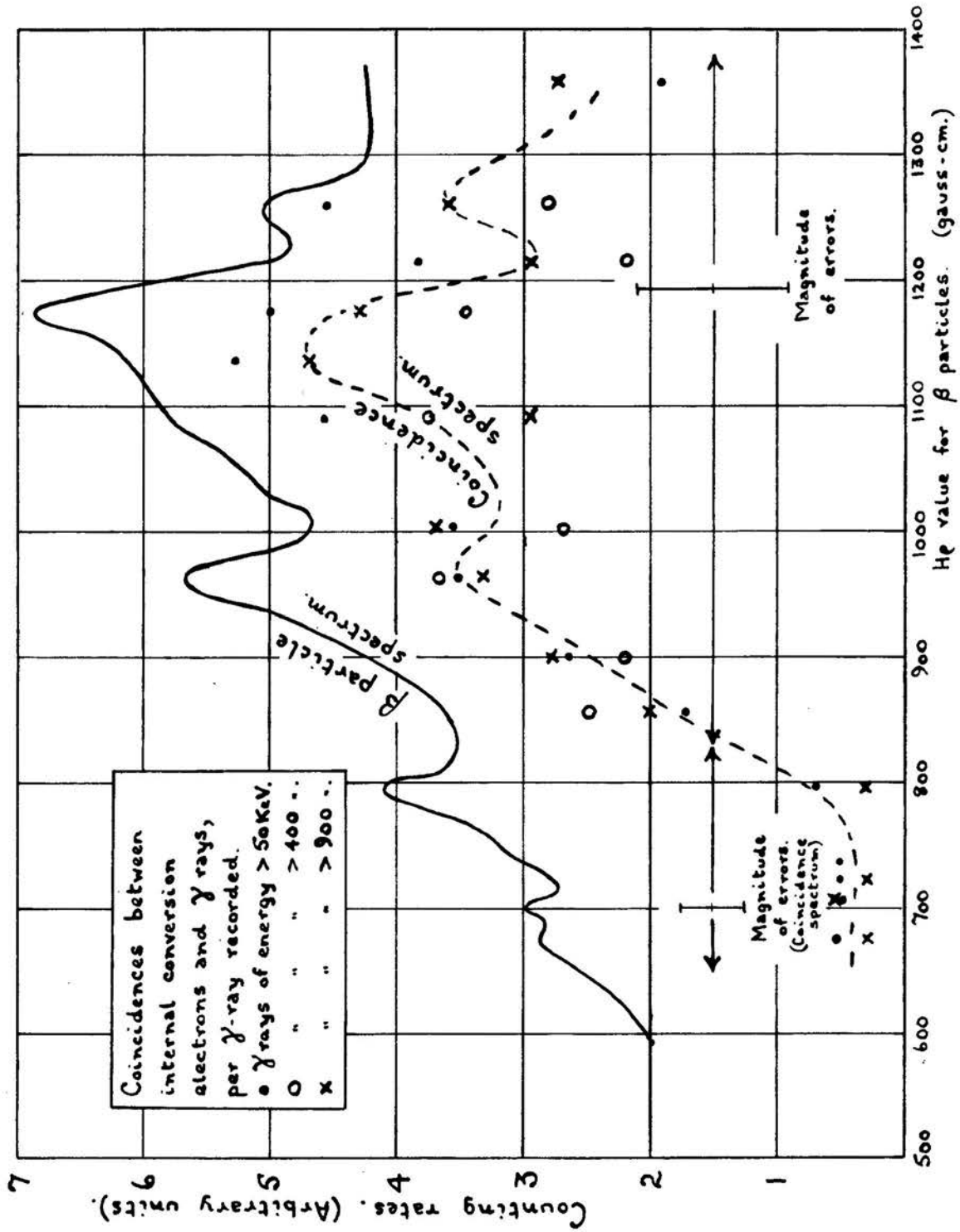
Coincidences between internal conversion electrons and γ rays, per γ-ray recorded.
• γ rays of energy > 50 KeV.
o " " " > 400 " "
x " " " > 900 " "
β Particle spectrum.
Coincidence spectrum.
Magnitude of errors.
Magnitude of errors. (Coincidence spectrum)
Counting rates. (Arbitrary units).
Hρ value for β particles. (gauss-cm.)
500
600
700
800
900
1000
1100
1200
1300
1400
1
2
3
4
5
6
7

FIGURE 7·12.

the unresolved lines at 790 and 815 gauss-cm. shews no coincidences with any other γ-ray, when the resolving time is 10^{-8} sec. A similar negative result was given with the longer resolving time of 10^{-7} sec. It therefore appears that the 57 keV γ-radiation may have a lifetime considerably in excess of 10^{-7} sec.

(2) The K-shell conversion electrons of a 184 keV γ-ray give a line at 948 $H\rho$, which overlaps the $L_{,}$ and $L_{,,}$ conversion electron lines of a 98 keV γ-ray. A considerable coincidence counting rate is obtained for all ranges of γ-radiation energies recorded by the counter, shewing that one, or both of these γ-rays is in coincidence with most of the other γ-radiations.

(3) Observations on the unresolved lines at 1166 and 1185 $H\rho$, which are attributed to the $L_{,,,}$ and the $L_{,,,}$ conversions of the 127 keV γ-ray, shew that this radiation is also in coincidence with most of the other γ-rays. The line at 1247 $H\rho$ is attributed to the M-shell conversion of this γ-ray.

§8. Coincidences between internal conversion electrons of different lines.

Again, only the stronger lines may be studied in these experiments without impracticably long counting periods due to the small solid angle for collection of electrons of the semicircular focusing spectrometer, and to the presence of a considerable background of coincidences between electrons of the continuous spectrum and γ-rays. Moreover, having set one β-particle counter on a particular conversion line, the second counter may be adjusted to receive electrons of internal conversion lines of a limited energy range only. Fortunately, in the case of $MsTh_2$, coincidence studies could be made with the double spectrometer between electrons of all the strong lines of the spectrum, since suitable conversion lines exist which are sufficiently closely spaced.

The source, evaporated on to a rectangle of aluminium foil of length 1 cm. and width 2 mm., and of thickness 0.2 mg./cm.^{2}, which was supported on a collodion film, was set at an emission angle of 45°. The source slits of width 7 mm. were cut so that the source was effectively displaced towards the image by half its effective width from the plane containing the centre lines of the source slits. The counter slit was of width 1.5 cm. Thin polycrystalline layers of anthracene (of ~20 mg./cm.^{2}) were used to reduce the background counting rate due to γ-rays.

With one counter set to receive the $L_{II,III}$ shell conversion electrons of the 127 keV γ-radiation (at an $H\rho$ value of ~1175 gauss-cm.), the second counter was moved to receive electrons over the range of energies from 700 to 1200 gauss-cm. Genuine coincidence counting rates were deduced from the observations at resolving times of both 10^{-8} and 10^{-7} sec. The curve of Figure 7.13 shews the variation in the counting rate obtained by moving a single counter through this region of the spectrum. The γ-ray and noise background counting rates have not been deducted from the counting rate shewn in this case, and represent approximately one half of the counting rate at ~700 $H\rho$ and one third of the counting rate at ~1200 $H\rho$. The peak at ~800 $H\rho$ is attributed to the M and N shell conversion electrons of the 57 keV γ-radiation, that at~950 $H\rho$ to the K shell conversion electrons of the 184 keV γ-radiation, and that at ~1175 gauss-cm. to the $L_{II,III}$ shell conversion electrons of the 127 keV γ-radiation. The points marked below this curve represent the genuine coincidence counting rates observed.

It is clear that the coincidence rate shews no tendency to follow the peaks of the single channel curve belonging to the 57 and 184 keV γ-radiations.

An estimate will now be made ofthe coincidence rate which might be expected between the electrons of the $L_{II,III}$ shell conversions of the 127 keV γ-radiation

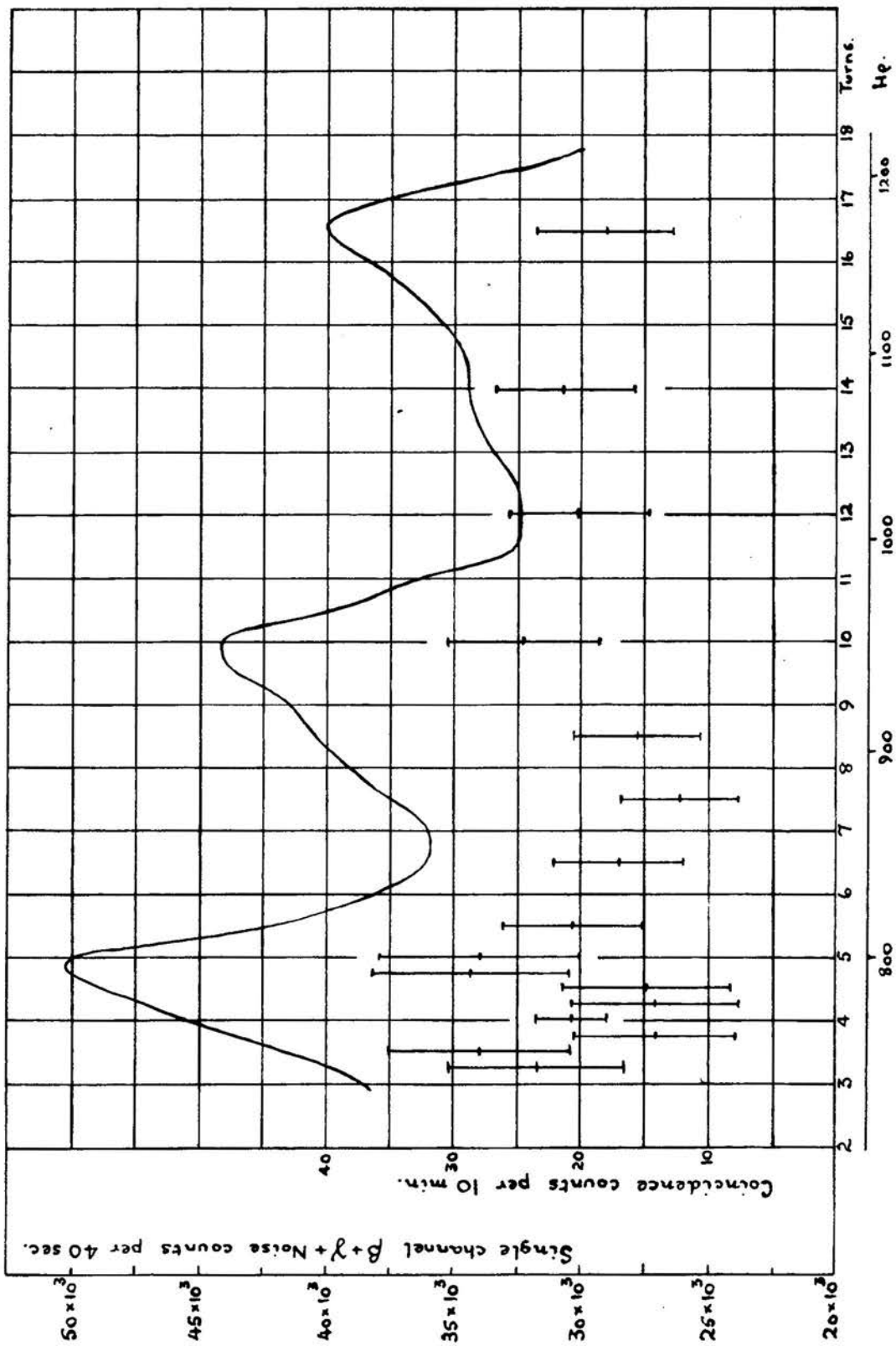

FIGURE 7.13 See text.

and the M and N conversion electrons of the 57 keV radiation, if these two γ-rays are presumed to be in cascade and if neither possesses a lifetime greater than 10^{-8} sec. Use is made of equation 2.58 of Chapter 2, § 13.1, which shews that the genuine counting rate G is expressed by

$$G = N f_1 c_1 \epsilon_1 p_2 c_2 \epsilon_2$$

The symbols are explained in §13.1 of Chapter 2.

The counting rate at the peak of the conversion lines due to the 57 keV γ-radiation, after deduction of the background counting rate caused by β-particles of the continuous spectrum, and by γ-radiations, is

$$C_2 = N f_2 c_2 \epsilon_2$$

The genuine coincidence rate, G, then becomes

$$G = C_2 \frac{p_2}{f_2} f_1 c_1 \epsilon_1$$

in which the suffix 1 refers to the conversion electrons of the 127 keV γ-radiation.

To estimate f_2 (which represents the fraction of the disintegrations of the source in which the 57 keV transition occurs ~~γ-radiation is emitted~~) an assumption has to be made regarding the particular type of γ-radiation emitted. Anticipating the discussion of Chapter 8 and in particular the classification of the γ-rays summarized in Table 8.3, f_2 will be taken as 0.6.

The term $f_1 c_1$ represents the intensity of the particular internal conversion line on which the counter is set, per disintegration of the source. For the $L_{II,III}$

shell conversions of the 127 keV γ-ray this will be shewn in Table 8.1 to be 0.056.

The 57 keV ~~γ-radiation is emitted~~ transition occurs in a fraction p_2 of the occasions in which the 127 keV ~~γ-radiation is emitted~~ transition takes place. Neglecting any possible delay in the emission of the 57 keV radiation, p_2 is taken as ~ 1.

ϵ_1 represents the solid angle for collection of the electrons of the conversion line due to the 127 keV γ-radiation and is estimated as not less than $\frac{1}{1000}$ of 4π .

Taking C_2 as 12,500 counts per 40 seconds, the number of coincidences to be expected in a counting period of 10 min., if the two γ-rays are in cascade, and if neither has a lifetime of greater than 10^{-8} sec., becomes not less than 17.5. It would have been possible to observe such a genuine coincidence rate, had it been present.

Turning now to the possibility of coincidences between the conversion lines of the 127 and 184 keV radiations (which have been shewn in the experiments described in § 7 to possess lifetimes of less than 10^{-8} sec.) a similar argument shews that ~ 140 coincidences per 10 min. might be expected were the γ-radiations emitted in cascade.

Using the suffix 1 to refer to the 127 keV radiation, and 2 to refer now to the 184 keV γ-radiation,

the following values have been adopted in this estimation:-

C_2 = 10,000 counts/40 sec.

p_2 = 1

f_2 = 0.072

$f_1 c_1$ = 0.056

ϵ_1 = 0.001

Clearly if the quantum emission of the 184 keV γ-radiation is higher than ~1.2%, then this coincidence rate will be smaller, but, even so, it seems likely that genuine coincidences would have been observed, were they present.

It was therefore concluded that the 127 and 184 keV γ-rays were not in cascade, and that the new results involving the 57 keV γ-radiation did not violate the previous conclusion that the lifetime for emission of this γ-ray exceeds 10^{-7} sec.

§9. γ-γ coincidence studies.

Both detectors were placed as close to the source as possible and were screened from β-particles by closing both the source slits with shutters. Anthracene crystals of thickness ~0.5 cm. were used.

With the voltage on one multiplier set so that only γ-rays of energies above ~900 keV were detected, γ-γ coincidences were observed with various voltages applied to the second counter. Table 7.3 summarizes the results of these experiments.

TABLE 7.3

Energy of γ-rays detected by counter #2 (keV). (1)	Total number of genuine coincidences. (2).	Genuine coincidences per γ-ray detected by counter #1. (3).
> 400	75 ± 16	6.2 ± 1.3
> 500	157 ± 27	7.6 ± 1.3
> 650	86 ± 21	3.9 ± 1.0
> 750	35 ± 12	2.7 ± 0.9
> 900	14 ± 12	1.0 ± 0.9

Further experiments shewed that no coincidences were recorded between γ-rays of energy greater than 1 MeV, and the 400-500 keV γ-rays.

It is therefore concluded that:-

(i) No γ-rays of energies greater than 900 keV are in coincidence.

(ii) Coincidences exist between γ-radiations of energies between 900 and 1000 keV and γ-radiations of energies between 400 and 500 keV, but no coincidences exist between γ-rays of energies greater than 1 MeV

and the 400-500 keV γ-rays.

The method was of insufficient resolving power to analyse further coincidences between γ-rays of energy $\sim$900 keV and γ-rays of energy less than $\sim$400 keV.

§10. The estimation of the error in the estimate of the number of genuine coincidences.

The number of coincidence counts, T, recorded includes a certain number of accidental coincidences, A, arising from the finite resolving time of the coincidence set, τ. From a knowledge of τ, this number of accidental coincidences may be estimated using the formula

$$A = \frac{2N_1N_2\tau}{P} \qquad (7.1)$$

in which N_1 and N_2 refer to the total number of counts recorded in the channels feeding the coincidence mixer, in a period, P.

It is assumed that the number of accidental and genuine coincidences, and the total number of coincidences, a, g and t, are distributed normally* with expected values of $\bar{a}$, $\bar{g}$ and $\bar{t}$ respectively and with standard deviations of $\sqrt{\bar{a}}$, $\sqrt{\bar{g}}$ and $\sqrt{\bar{t}}$.

All that is observed is T, a sample reading of t, and the resolving time τ, which may be determined very accurately with long counting periods (cf. § 8 of Chapter 3). Let σ_τ be the standard deviation in this observed τ. Since T is the only estimate of $\bar{t}$, it follows that the best estimate of $\bar{g}$ is

$$G = T - A, \qquad (7.2)$$

---

* Strictly they will form Poissonian distributions but, with the number of coincidences usually recorded, these will closely approximate to normal distributions.

where A is the best estimate of $\bar{a}$ and is calculated from equation 7.1.

The estimate of number of accidental coincidences, A, will possess a standard deviation of σ_A given by

$$\sigma_A = \frac{2N_1N_2\sigma_\tau}{P} \qquad (7.3)$$

The standard deviation of G, σ_G, will then be given by

$$\sigma_G^2 = T + \sigma_A^2 \qquad (7.4)$$

where $\sqrt{T}$ is the standard deviation in T, since the distribution in a is independent of the distribution in t.

In practice, σ_A^2 is negligibly small, and the standard deviation in the estimate of the number of genuine coincidences becomes $\sqrt{T}$.

It is frequently stated that the standard deviation in G is $\sqrt{T+A}$, but if there are no genuine coincidences in the recorded total, then T should be normally distributed about A with standard deviation of $\sqrt{A}$, and not of $\sqrt{2A}$ as would follow from the expression $\sqrt{T+A}$.

§11. An Attempt to measure the half-life of the state emitting the 57 keV γ-radiation.

Let the pulses from a β-particle counter be fed to a scaler, the input circuit of which is capable of making the instrument insensitive to further input pulses for a known "paralysis" time, σ, immediately following the leading edge of an input pulse. Let:-

B be the background count of the β-particle detector per second,

N be the number of disintegrations of the source, per second,

f be the fraction of these disintegrations which are followed by the emission of a delayed conversion electron,

ϵ_1 be the nett efficiency of the detector for disintegration electrons, and

ϵ_2 be the nett efficiency of the detector for delayed conversion electrons.

For the hypothetical case in which the paralysis time of the scaler and the counter "dead" time are supposed to be zero, the counting rate will be

$$C_0 = B + N\epsilon_1 + Nf\epsilon_2 \qquad (7.5)$$

The counting rates due to conversion electrons, other than those mentioned, and to the quantum emission of γ-rays may be regarded as adding to the background counting rate.

Let it now be supposed, for simplicity, that the internal conversion electrons, which follow the

disintegrations of the source, are delayed by a constant time interval t.

When σ is less than t (but is greater than the counter "dead" time) the observed counting rate will be C_1, given by

$$\frac{1}{C_1} = \frac{1}{C_0} + \sigma \qquad (7.6)$$

Although the pulses from the detector do not form a sequence which is strictly random, due to the "pairing" of events, it has been shewn by Feather[38] that the same correction for counting losses, due to the introduction of a finite paralysis time, is equally applicable here as it is to the case of a truly random sequence of events.

The plot of $\frac{1}{C_1}$ against σ will give a straight line (at 45° to the co-ordinate axes, if the scales chosen for the axes are equal). The line, when extrapolated, will cut the $\frac{1}{C}$ axis at $\frac{1}{C_0}$.

If σ is now adjusted to exceed t, then, in addition to counting losses due to the finite paralysis time of the circuit, further losses will be incurred, since those delayed internal conversion electrons, for which a disintegration electron has been detected, will no longer be recorded. The number of particles detected if counting losses due to the finite paralysis time are, for the moment, neglected, will then be C_2, given by

$$C_2 = C_0 - N f \epsilon_1 \epsilon_2 \qquad (7.7)$$

Taking into account these losses, the recorded counting rate will become C_3, given by

$$\frac{1}{C_3} = \frac{1}{C_2} + \sigma \qquad (7.8)$$

Thus, when $\sigma > t$, a second straight line is given on plotting $\frac{1}{C_3}$ against σ, which, on extrapolation, intercepts the $\frac{1}{C}$ axis at $\frac{1}{C_2}$. This line will be parallel to the line given when $\sigma < t$, but will be displaced upwards from it as shewn in Figure 7.14. The ratio of the intercepts with the $\frac{1}{C}$ axis for the two lines will be

$$\frac{C_0}{C_2} = \frac{C_0}{C_0 - N f \epsilon_1 \epsilon_2} \qquad (7.9)$$

When $\sigma = t$, a sudden transition from one line to the other will occur, as shewn in Figure 7.14. In real cases, the interval t is not constant, but varies exponentially with a decay constant corresponding to the half-value period for the delayed emission. This produces a gradual change from one line to the other, rather than the abrupt change shewn.

It is clear, therefore, that by observing the counting rates for various paralysis times, it may be possible, in certain circumstances, to detect the existence of the emission of those delayed conversion electrons which follow disintegration β-particles.

For the method to succeed, the loss in counts due to the "pairing" of events should not be small when compared with the loss produced by the finite paralysis

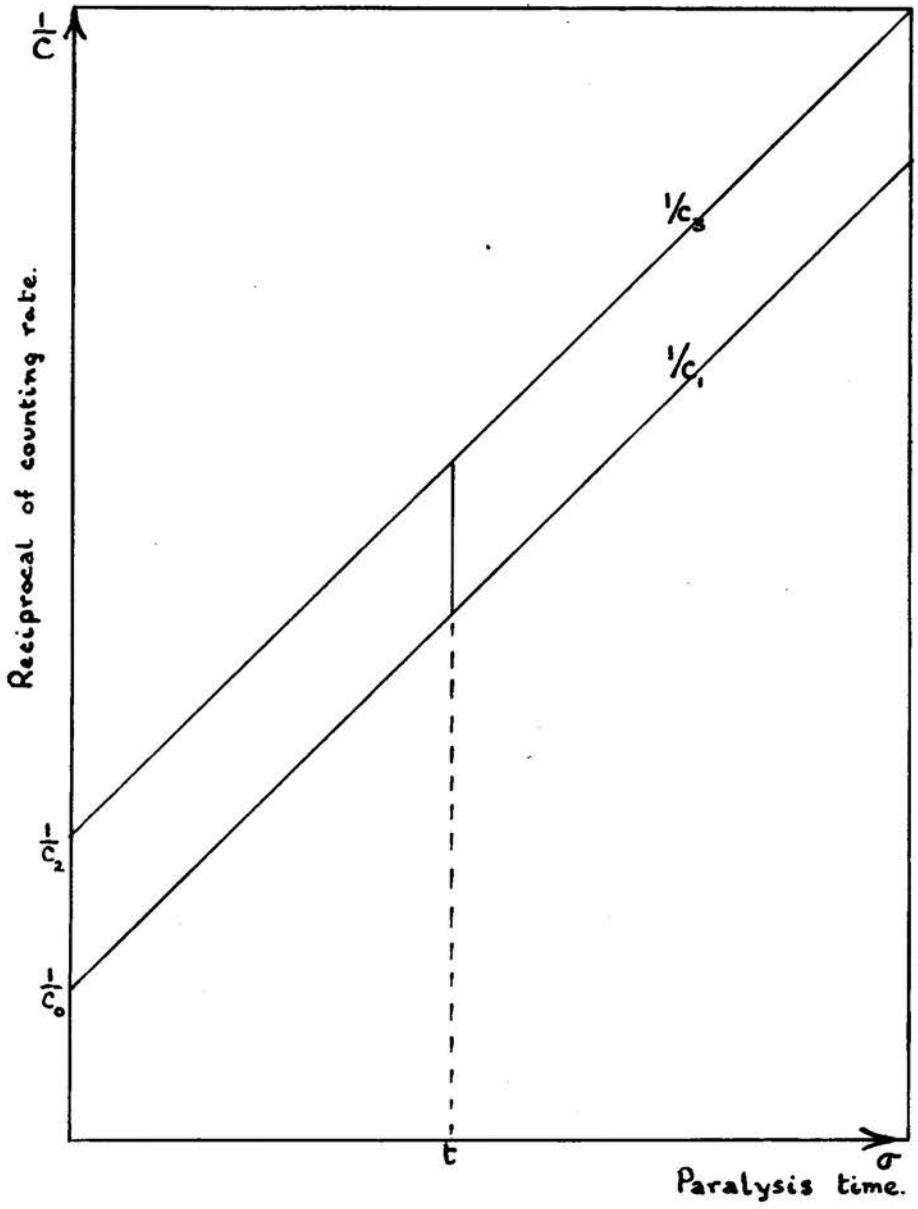

FIGURE 7·14 See text.

time of the electronic circuits. The ratio of these losses is easily shewn to be

$$\frac{N f \epsilon_1 \epsilon_2 \left[1 + \sigma(B + N\epsilon_1 + N f \epsilon_1)\right]}{\sigma(B + N\epsilon_1 + N f \epsilon_1)^2}$$

If ϵ_1 is effectively equal to ϵ_2, the ratio becomes

$$\frac{f\left[\frac{1}{N} + \sigma\epsilon\left(1 + f + \frac{B}{N\epsilon}\right)\right]}{\left(1 + f + \frac{B}{N\epsilon}\right)^2}$$

This is increased by reducing N and by increasing ϵ. B should be as small as possible, especially when N is made small.

The technique outlined above was applied to study the disintegration of $MsTh_2$. Coincidence experiments had shewn that the 57 keV γ-radiation, which gives rise to the emission of a conversion electron in some 60% of the disintegrations, had a lifetime in excess of 10^{-7} sec.

A very weak source of $MsTh_2$ was evaporated on to the cathode of a Geiger counter. In this way a 50% geometry was obtained, making ϵ_1 and $\epsilon_2 \sim \frac{1}{2}$. The principal features of the counter used are shewn in Figure 7.15. Counters of this typepossessed plateaux, some 350v in length, starting at ~900 volts with slopes of 0.05% per volt. The output of the counter was taken via a probe unit (type 1014) to two scalers (type 1009A) connected in parallel. Simultaneous observations, using two distinct paralysis times were thus possible.

The various settings of the paralysis time of

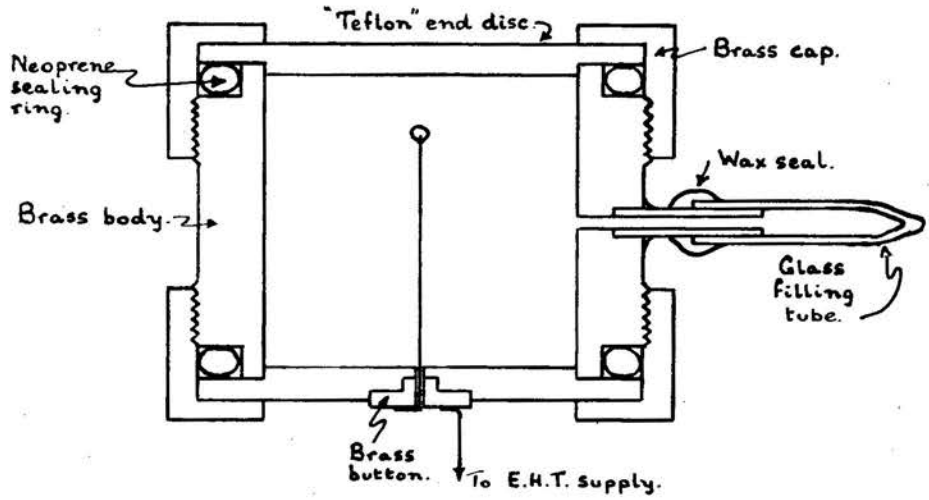

FIGURE 7-15. The Geiger counter.

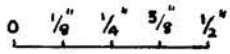

the input circuit of these scalers were measured in the following way. A double pulse generator (type 1013C) was used to supply pulses to the probe unit the "dead" time of which was set at a nominal 200 μsec. The output pulses from the probe unit were taken to each scaler in turn. On increasing the spacing of the pulses from the double pulse generator, a pulse separation was found for which the scaler ceased to shew single pulses, but counted double pulses only. Thiscondition was clearly indicated by the "number one" neon of the scaler either staying permanently on, or being permanently extinguished.

At the same time the output of the double pulse generator was fed to a timing circuit*. The first pulse emitted by the pulse generator was used to operate an electronic switch, which connected the output pulses from a 50 kc/s crystal controlled oscillator to a scaler (Airmec type 704)of very small input paralysis time. The second pulse from the generator disconnected the circuit. Thus a burst of pulses was counted by this scaler during the paralysis time of the scaler (type 1009A) under test. Observation of the total number of pulses recorded in about one hundred of such bursts

---

* The writer is indebted to Mr.A. McDonald, of Edinburgh University, for the use of this equipment.

allowed an accurate determination of the "paralysis" time of the scaler. Each setting of the paralysis time, (longer than that of the probe unit paralysis time) was measured in this way for both scalers. An attempt to measure the paralysis time of the probe unit (by setting that of the scaler to ~2 μsec.) shewed that it was dependent on the shape of the input pulse. For this reason, only paralysis times of the scaler input circuits longer than that of the probe unit were used in the experiments with a Geiger counter. The counting rates with a paralysis time of 502 μ sec. were compared, in turn, with those with paralysis times of 1.009, 5.230 and 10.285 m sec. Table 7.4 summarizes the results.

TABLE 7.4.

Paralysis time, σ_1. (m.sec.) (1)	Counts per 300 sec. C_1' (2).	Paralysis time, σ_2. (m.sec.) (3).	Counts per 300 sec. C_2'. (4).	$\frac{300}{C_1'} = \frac{300}{C_2'} - (\sigma_2 - \sigma_1)$ (m.sec.) (5).	C_1'' (6)	$C_1' - C_1''$ (7)
0.502	27015	1.009	25773	11.133	26947	+68
0.502	27535	5.230	19221	10.879	27576	-41
0.502	27600	10.285	14516	10.884	27563	+37
0.502	26107	1.009	25055	11.467	26162	-55
0.502	26784	5.230	18873	11.168	26862	-78
0.502	26977	10.285	14326	11.157	26889	+88

C" represents the number of counts which would be expected with a paralysis time of 0.502 m sec., estimated from the number of counts observed with various longer

paralysis times. This estimate assumes no losses due to "pairing" of events. The differences between C" and C' , the actual counts observed with a paralysis time of 0.502 m. sec., are small and distributed about zero, indicating that no substantial loss of counts due to "pairing" of events occurs between paralysis times of 0.5 and 10 m. sec. The order of magnitude of the loss expected, if "pairing" losses were to occur for paralysis times in this range, is given by the expression $300\,N f \epsilon_1 \epsilon_2$ in which $\epsilon_1 = \epsilon_2 = f \simeq \frac{1}{2}$, and $N \simeq 125$ counts/sec. The expected losses due to pairing are then ~ 4500 counts per 300 sec. Only a small fraction of these losses would be observed if the lifetime of the delayed emission were considerably in excess of 10 m. sec.

It therefore seems clear that the half-life of the state emitting the 57 keV γ -ray is either considerably greater than 10 m. sec. or lies between 10^{-7} sec. and 500 μsec.

To test whether much shorter paralysis times would shew pairing of events, the experiment was repeated using a scintillation counter with anthracene as the phosphor. The crystal was placed on the end-window of the multiplier (EMI type 5045) and a weak source of $MsTh_2$ was placed on the crystal. The multiplier voltage

was set to ~2300 volts to ensure that low energy β-particles would be detected with high efficiency. It was assumed that this voltage was sufficient since, with the much less efficient light collection of the optical system used with the spectrometer, particles of this energy were detected at this voltage, but with reduced efficiency.

Observations of the counting rates at input paralysis times of 2, 100, 200 and 502 μsec., with further checks at 1.009, 5.230 and 10.285 m. sec. were made, and the reciprocal of the counting rate was plotted against the dead time. The experimental points for low values of σ, shewn in Figure 7.16, shews no tendency to fall below the line drawn at 45° to the axes.

It is possible that the life-time of the state emitting the 57 keV γ-ray lies between 10^{-7} sec. and 2 μsec. but, especially in the light of the observations of Lecoin, Perey and Teillac,[6] using a cloud chamber, it seems more likely that the half-value period exceeds 10 m sec.

The method described might possibly be extended to investigate whether the lifetime of the delayed emission exceeds 10 m sec. but, unless extremely small counting rates were employed, the paralysis time losses would become very large compared with those due to pairing of events. The background counting rate of the

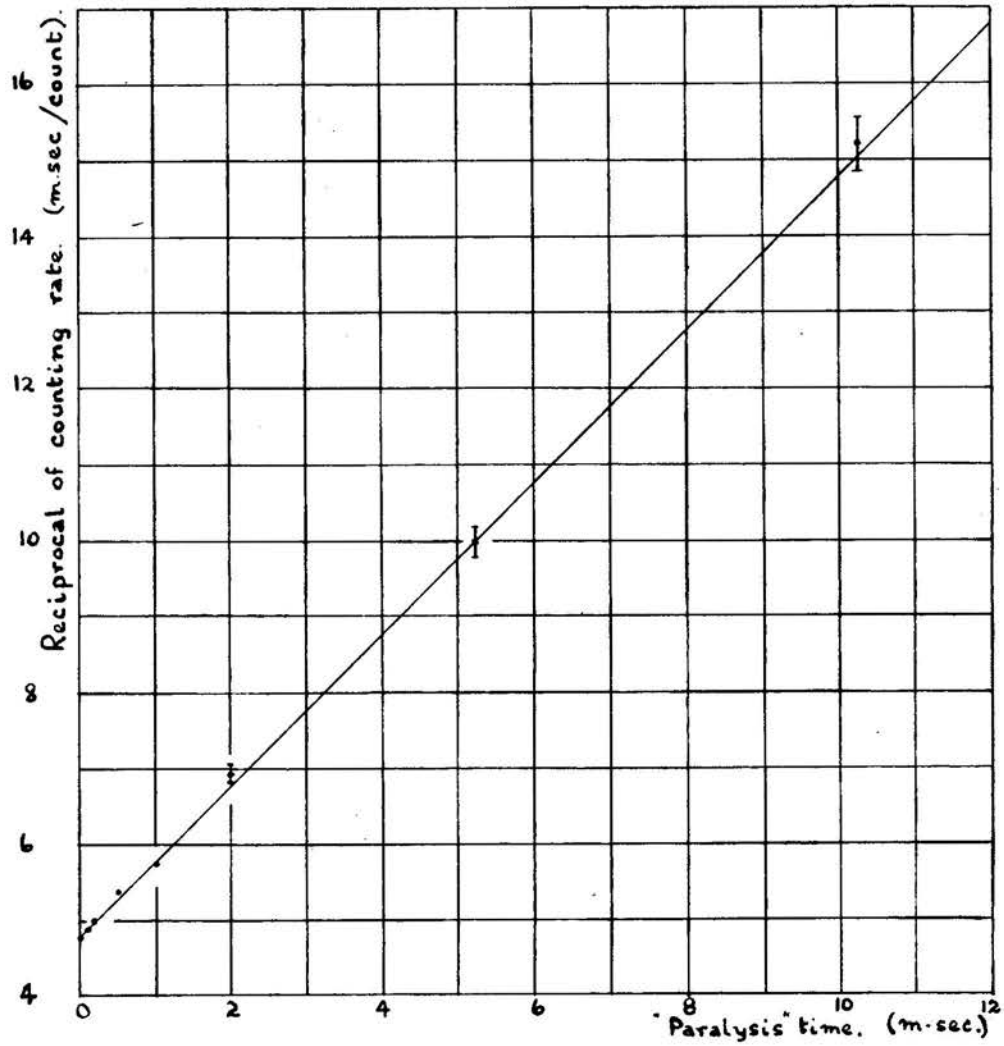

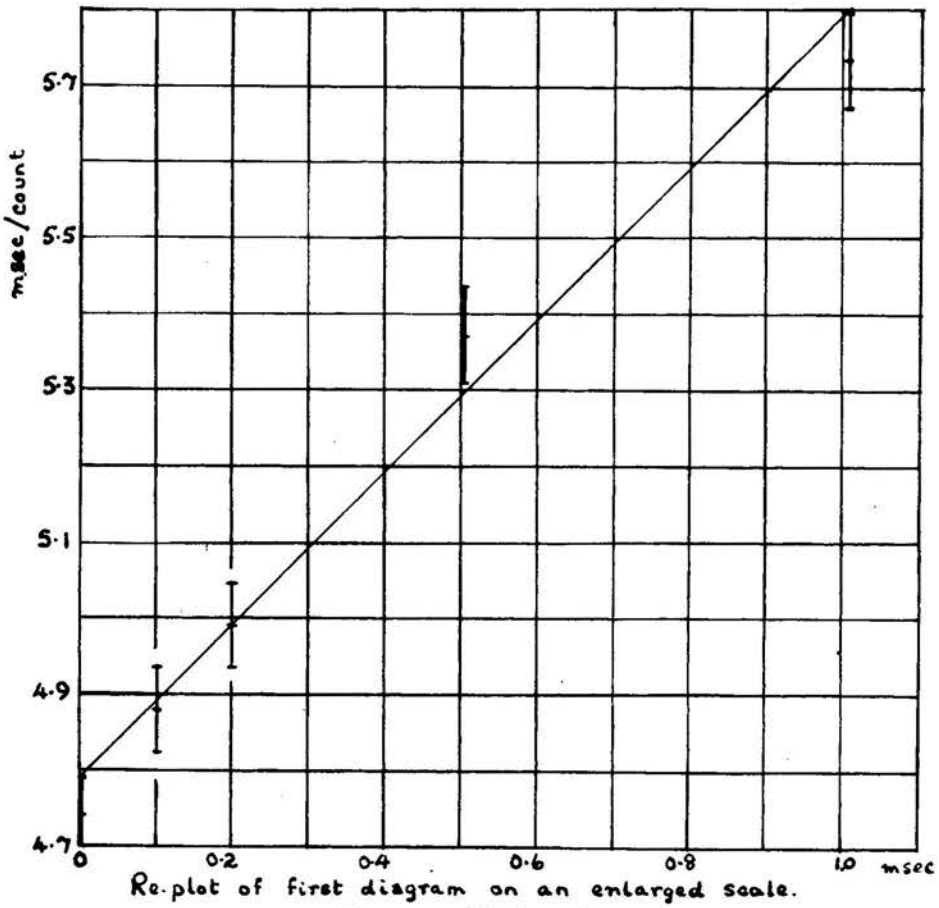

Re-plot of first diagram on an enlarged scale.

FIGURE 7·16 See text.

counter would eventually set a limit to the smallest source strength which could be used.

CHAPTER 8.

Discussion of the experimental results.

§ 1. The γ-rays suggested by analysis of the conversion lines.

A summary of the analysis of the conversion electron lines is shewn in Table 8.1, and the mean γ-ray energies obtained are listed in column 7. In this analysis, the electron extraction energies of Cauchois[39] were used, which, for Z = 90, are as follows:-

K	shell;	109.63 keV
L_I	"	20.46 "
L_{II}	"	19.69 "
L_{III}	"	16.30 "
M_I	"	5.18 "
M_{II}	"	4.82 "
M_{III}		4.04 "
M_{IV}	"	3.49 "
M_V	"	3.33 "
N_I	"	1.32 "
N_{II}	"	1.16 "

In some cases, where the interpretation of a line is not unique, both values of the deduced γ-ray energy have been included. All but nine of the conversion electron lines, observed either by Black, or in this investigation, have been assigned

to γ -rays. Of the remaining lines, which are all of weak intensity, that occurring at an $H\rho$ of 901 gauss-cm. is interpreted as an Auger line; γ -radiations associated with the remaining lines have not been identified.

The intensities of the lines listed in column 4 of the table were derived, whenever possible, from the recent observations by Brodie, using the lens spectrometer referred to in §1 of Chapter 7. For those cases in which lines were not resolved by this instrument, the total intensity of the unresolved group of lines was divided in the ratio of the corresponding line intensities observed photographically by Black. Certain weak lines at low energies, together with all the more energetic lines, were not observed with the lens spectrometer, and the intensity measurements derived from the observations of Black were used in these cases. These intensities should be regarded as indications of order of magnitude only.

TABLE 8.1

Line. (1)	Hρ value. (gauss-cm). (2).	Energy. (keV). (3).	Intensity per 100 disintegrations. (4).	Conversion shell. (5).	γ-ray energy. (keV). (6).	Mean γ-ray energy. (keV.) (7).
1	652	36.34	Weak	L_I	56.80	
2	659	36.91	23.8	L_{II}	56.60	56.75
3	690	40.33	20.2	L_{III}	56.63	
7	789	52.16	8.9	M_{II}	56.98	
8	815	55.41	7.1	N_I	56.73	
9	836	58.19	-	L_{II}	77.88	78.05
10	872	61.91	0.1	L_{III}	78.21	
14	977	77.98	3.3	L_{II}	97.67	97.77
15	1000	81.49	-	L_{III}	97.79	
16 *	1072	92.66	-	M_I	97.84	
16 *	1072	92.66	-	L_{II}	112.4	
17	1099	97.04	-	L_{III}	113.3	113.0
18 †	1166	108.1	-	M_I	113.3	
18 †	1166	108.1	3.3	L_{II}	127.8	
19	1185	111.3	2.3	L_{III}	127.6	
21 §	1247	122.2	-	M_I	127.4	127.5
22	1267	125.8	0.56	N_I	127.1	
12	929	71.03	-	K	180.6	179.0
26	1435	157.0	-	L_I	177.5	
13	948	73.76	4.7	K	183.4	
27	1475	164.9	1.0	L_I	185.4	184.2
28	1545	178.7	0.3	M_I	183.9	
21 §	1247	122.2	-	K	231.8	232.2
30	1721	212.0	-	L_I	232.5	
31	1771	225.9	0.75	K	335.5	336.0
33	2168	315.9	0.19	L_I	336.4	
32	2102	300.5	0.56	K	410.1	410.1
34	2305	348.6	0.75	K	458.2	
35	2663	437.0	0.38	L_I	457.5	457.6
36	2722	451.9	0.19	M_I	457.1	
37	4013	796.4	0.56	K	905.9	907.1
39	4345	888.6	0.19	L_I	908.3	
38	4237	858.5	0.28	K	968.1	964.5
41	4530	940.4	0.19	L_I	960.9	
40	4475	925.1	-	K	1035	1035
42	4689	985.1	-	K	1095	1095
43	6406	1477	0.09	K	1587	1587
44	6588	1530	0.09	K	1640	1640

§2. Classification of the observed partial spectra.

From the relative intensities of the six partial spectra observed, the half-value period, t, for each mode of β-decay was calculated, assuming the lifetime of $MsTh_2$ to be 6.13 hours. The value of $\log_{10} f$ for the maximum energy of each component spectrum was read from the appropriate member of the set of curves given by Feenberg and Trigg[40], and the value of $\log_{10} ft$ was calculated for each partial spectrum. These $\log_{10} ft$ values were then used to identify each mode of β-disintegration in accordance with the grouping suggested by Nordheim[41]. A summary of the predictions of this method is given in columns 7 and 8 of Table 8.2.

TABLE 8.2

Maximum energy of β-spectrum (MeV.) (1).	ε (mc^2) (2).	Relative intensity. (%). (3).	$\log_{10} t$ (4).	$\log_{10} f$ (5).	$\log_{10} ft$ (6).	Spin change and parity change. (7).	Degree of forbiddenness. (8).
2.18	5.26	10.1	5.34	3.55	8.9	2(Yes)	1st
1.85	4.62	9.6	5.36	3.30	8.7		
1.70	4.32	6.7	5.52	3.12	8.6		
1.11	3.17	53.0	4.62	2.44	7.1	Either 1 (no) or 0 or 1 (Yes)	Either Allowed (l-forbidden) or 1st
.641	2.26	7.6	5.47	1.70	7.2		
.448	1.88	13.0	5.23	1.15	6.4		

§ 3. A possible level scheme for RdTh.

In suggesting a possible level scheme for the daughter RdTh nucleus, it is assumed that the six partial β-ray spectra of the disintegration of $MsTh_2$ de-excite directly a single energy state of $MsTh_2$. The possibility of β-disintegration from more than one energy state of $MsTh_2$ will be examined in § 6.

Six energy states for the RdTh nucleus are thus established, and possible spins and parities for these states, referred to the spin and parity of the state of $MsTh_2$ de-excited by β-activity, are indicated by the conclusions summarized in column 7 of Table 8.2.

To fit the transitions responsible for the observed γ-radiations into the energy level scheme for the RdTh nucleus, in a manner which did not violate the experimental results outlined in Chapter 7, four energy levels, in addition to the six levels indicated by the end-points of the partial β-ray spectra, appeared to be required. Figure 8.1 illustrates the tentative level scheme proposed. Clearly the problem is one of considerable complexity, and alternative solutions may be equally valid.

Possible spins and parities were chosen for these four additional levels, and the spins and parities of the remaining six levels of RdTh (together with the spin and parity of the state of $MsTh_2$ involved directly in the β-transitions) were tentatively identified by ensuring that the probability of

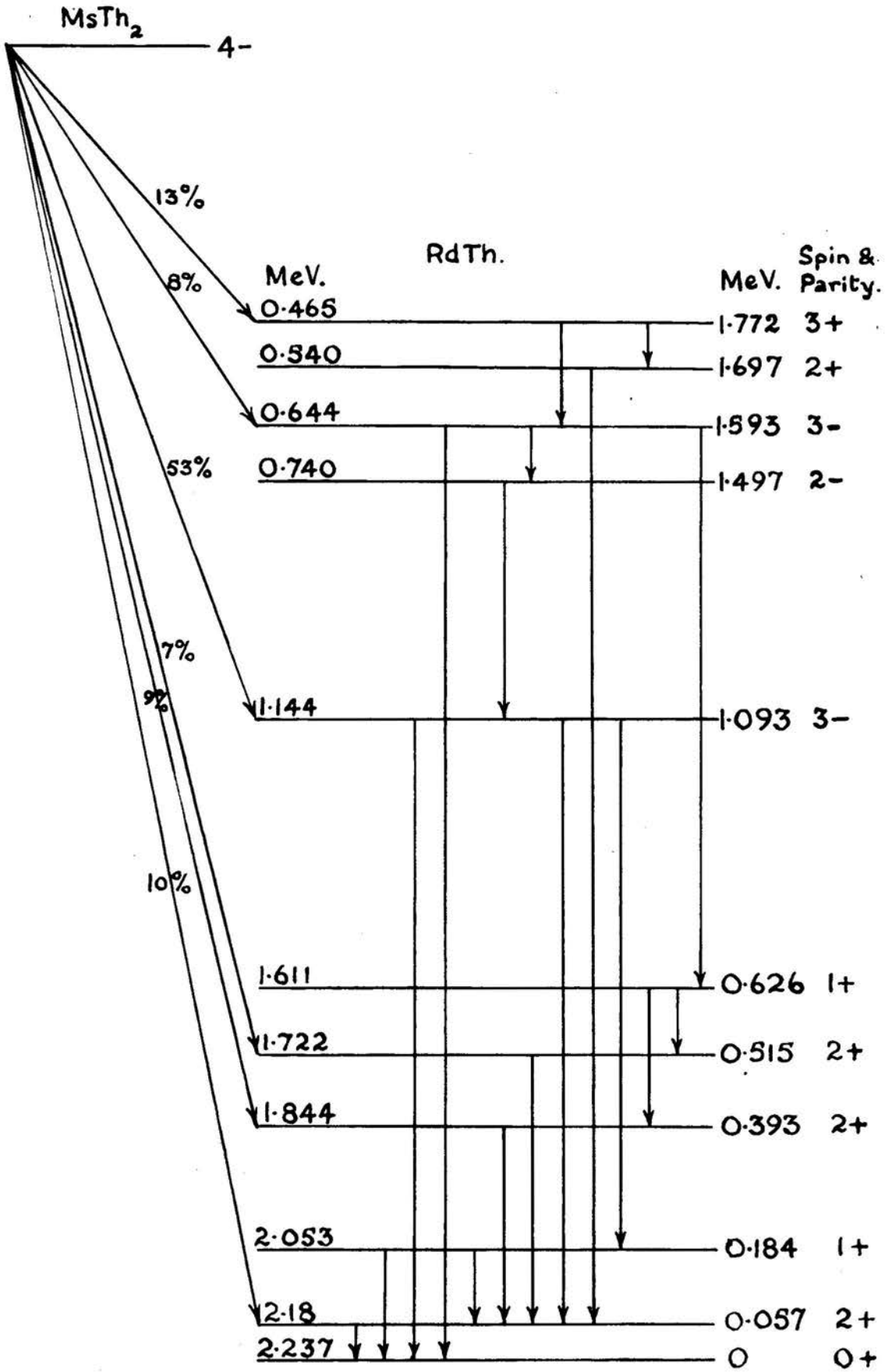

FIGURE 8·1. Suggested decay scheme.

each γ-transition possessed a feasible value. Such transition probabilities were calculated from the conversion line intensities shewn in Table 8.1, in conjunction with the K-conversion coefficients of Rose, Goertzel and Perry[42]. Columns 5, 6 and 7 of Table 8.3 summarize these deductions. For those transitions involving a mixture of types of radiation, the transition probability obtained by assuming the radiation to be entirely of one or of the other type is shewn. It has been assumed that the ground state of the even-even radiothorium nucleus ($^{228}_{90}$RdTh) possesses zero spin and even parity. The deductions made are corroborated to some extent in certain cases by the observed ratios of the K:L conversion coefficients and by the observed ratios of the L sub-shell conversion coefficients. These cases will be discussed later, together with the early work of Thibaud[43], using the method of the "excited" photoelectron spectrum, which adds further support to the identification of the types of γ-radiations made.

TABLE 8.3.

Line. (1)	Intensity per 100 disintegrations. (2)	Conversion shell. (3)	Mean γ-ray energy. (keV.) (4).	Type of radiation. (5).	K-conversion coefficient, (after Rose et al.) (6).	Total transition probability. (7).
1	Weak	L_I	56.75	E2	-	60%
2	23.8	L_{II}				
3	20.2	L_{III}				
7	8.9	M_{II}				
8	7.1	N_I				
9	-	L_{II}	78.05	E2+M1	-	-
10	0.1	L_{III}				
14	3.3	L_{II}	97.77	E2+M1	-	-
15	-	L_{III}				
16*	-	M_I				
16*	-	L_{II}	113.0	E2+M1	-	-
17	-	L_{III}				
18†	-	M_I				
18†	3.3	L_{II}	127.5	E2+M1	0.6 (E2)	~6% (See text).
19	2.3	L_{III}				
21§	-	M_I				
22	0.56	N_I				
12	-	K	179.0	E2+M1	-	-
26	-	L_I				
13	4.7	K	184.2	M1	4.0	7.2%
27	1.0	L_I				
28	0.3	M_I				
21§	-	K	232.2	E2+M1	-	-
30	-	L_I				
31	0.75	K	336.0	E2+M1	0.8 (M1) 0.06 (E2)	1.9% (M1) 13.4% (E2)
33	0.19	L_I				
32	0.56	K	410.1	E2+M1	0.49 (M1) .044 (E2)	1.7% (M1) 13.3% (E2)
34	0.75	K	457.6	E2+M1	0.36 (M1) .035 (E2)	3.4% (M1) 22.8% (E2)
35	0.38	L_I				
36	0.19	M_I				
37	0.56	K	907.1	E3+M2	0.10 (M2) .023 (E3)	6.4% (M2) 25.1% (E3)
39	0.19	L_I				
38	0.28	K	964.5	E3+M2	.086 (M2) .021 (E3)	3.7% (M2) 13.8% (E3)
41	0.19	L_I				
40	-	K	1035	E1	-	-
42	-	K	1095	E3	-	-
43	0.09	K	1587	E3	.0075	12%
44	0.09	K	1640	E2+M1	.014 (M1) .0036 (E2)	6.5% (M1) 25.1% (E2)

A summary of the number of transitions which excite each state, together with the number of de-exciting transitions, per 100 disintegrations of $MsTh_2$, is given in Table 8.4.

TABLE 8.4

Excitation energy of state. (keV.) (1)	Number of transitions exciting this state, (per 100 disintegrations). (2)	Number of transitions de-exciting this state, (per 100 disintegrations). (5)
0	79% + 1095 keV (E3)γ	100%
57	MIN. 28% + 1035 keV (E1)γ MAX. 77% + 1035 keV (E1)γ	60%
184	MIN. 6.4% MAX. 25%	13%
393	9% + 232 keV (E2+M1)γ	MIN. 1.9% MAX. 13%
515	7% + 113 keV (E2+M1)γ	MIN. 3.4% MAX. 23%
626	MIN. 3.7% MAX. 14%	113 keV (E2+M1)γ + 232 keV (E2+M1)γ
1093	MIN. 55% MAX. 66%	MIN. 6.4% + 1035 keV (E1)γ + 1095 keV (E3)γ MAX. 25% + 1035 keV (E1)γ + 1095 keV (E3)γ
1497	98 keV (E2+M1)γ	MIN. 1.7% MAX. 13%
1593	8% + 179 keV (E2+M1)γ	MIN. 16% + 98 keV (E2+M1)γ MAX. 26% + 98 keV (E2+M1)γ
1697	78 keV (E2+M1)γ	MIN. 6.5% MAX. 25%
1772	13%	78 keV (E2+M1)γ + 179 keV (E2+M1)γ

Any further information regarding the intensities of the conversion lines, or any new and more accurate theoretical values for the L-shell conversion coefficients, may well lead to a revision of the scheme suggested.

§ 4. Further remarks on the individual γ -radiations.

(i) The 57, 127 and 184 keV radiations.

The predominant conversions of the 57 keV radiation occur in the L_{II} and L_{III} sub-shells, with a relatively small L_I conversion. The "relativistic, but unscreened" L sub-shell conversion coefficients of Gellman, Griffith and Stanley[44] suggest that the transition is not electric or magnetic dipole. The ~~γ -ray is emitted~~ transition occurs in ~60% of the disintegrations, which, together with its relatively long half-life, suggests that no other competing γ -ray de-excites the same energy state. It seems very probable therefore that this radiation comes from the first excited state of RdTh. The possibility of the transition occurring in the $MsTh_2$ nucleus cannot at first be ruled out, but the various values for the energy of each γ -ray, derived from the energies of the various conversion lines observed, are more widely scattered when the electron extraction energies appropriate to a nucleus with a charge number of 89, rather than 90, are used. Moreover, recent study of the α -particle activity of $^{231}_{91}U$ by Dunlavey and Seaborg[45] has shewn the existence of an excited state of RdTh at an energy of ~60 keV. It seems plausible to identify this level with that at 57 keV shewn in the suggested decay scheme.

To account for the relatively long lifetime

of the state emitting the 57 keV γ-radiation, it is suggested that the radiation is either electric or magnetic quadrupole, or of still higher order. The data presented in the review of isomeric transitions, by Goldhaber and Sunyar[46], were used in studying lifetimes of excited states.

Study of the 127 and 184 keV γ-radiations imposes further restrictions on the classification of the 57 keV transition. The relative intensities of the conversions of the 127 keV γ-ray in the L sub-shells suggest that this radiation is electric quadrupole. A K:L ratio of 1:40 has been observed by Brodie (private communication) and a comparison of the K threshold conversion coefficients of Spinrad and Keller[47] with the L sub-shell coefficients of Gellman et al. leads to the best agreement with observations, if this γ-ray is assumed to be predominantly electric quadrupole.

With regard to the 184 keV γ-radiation, the strong L_I conversion, with no L_{II} or L_{III} conversions found, together with the short half-life, suggest that the radiation is magnetic dipole, although the K:L ratio of 5:1 is rather low (cf. Goldhaber and Sunyar). Quantum emission of this energy was detected by Thibaud, but since no intensity is quoted for the photoelectron line excited in lead, it seems probable that the line was too weak to be measured. This agrees with the estimate of ~1% for

the quantum intensity, if this radiation is classified as magnetic dipole.

Assuming that the 184 keV γ-radiation is magnetic dipole, and that this radiation is a cross-over for the 127 and 57 keV γ-rays in cascade, the 57 keV transition must then be classed as electric quadrupole (if the 127 keV γ-ray transition gives a mixture of magnetic dipole and electric quadrupole radiations) or as magnetic octupole (if the 127 keV γ-radiation is mainly electric quadrupole). Although, in the former case, it is difficult to appreciate the reason for the 127 keV radiation's being predominantly electric quadrupole, in view of the theoretical predictions of Austern and Sachs[48], who claim that in such cases magnetic dipole radiation should predominate, it is thought it is more likely that the 57 keV radiation is electric quadrupole than magnetic octupole. The statistical evidence is strongly in favour of the first excited state of an even-even nucleus having a spin of 2 and even parity, and moreover the lifetime of magnetic octupole radiation of this energy would probably be sufficiently long to be detected by ordinary decay methods.

(ii) <u>The 336, 410, 458, 907 and 965 keV radiations.</u>

These radiations have all been observed by Thibaud[43] using the method of the "excited" photoelectron spectrum. The intensities of the photo-

electron lines, observed with a source of $MsTh_1$ in equilibrium with its decay products, are referred to the intensity of the strong line excited by the 582 keV M γ -ray of ThC" → Pb, which is given the arbitrary value of 100. In order to estimate, very roughly, the absolute quantum intensities of the γ-rays of the $MsTh_2$ → RdTh transition, use was made of the absolute measurement of the quantum intensity of the 582 keV energy γ -ray, observed by Martin and Richardson(49). The number of γ -rays of this energy emitted per 100 disintegrations of ThC" is quoted as 65, which, on allowing for the branching at ThC, gives a value of 22 γ -rays of energy 582 keV per 100 disintegrations of $MsTh_1$. By assuming that a photoelectron line, of intensity 100, corresponds to an absolute quantum intensity of 22%, the absolute quantum intensities of the γ -rays belonging to the RdTh nucleus were deduced. Column 4 of Table 8.5 summarizes the results of this comparison.

TABLE 8.5

Nucleus. (1)	γ-ray energy. (keV.) (2)	Relative intensity. (Thibaud). (3)	Absolute quantum intensity per 100 disintegrations of $MsTh_1$. (4)
Pb	582	100	22
RdTh	183	-	-
"	336	40	8.8
"	410	15	3.3
"	458	20	4.4
"	907	80	17.6
"	964	70	15.4

It is pointed out by Martin and Richardson that the area under a photoelectron line is not directly proportional to the quantum intensity of the γ-radiation which excites the line, corrections being required, dependent on the energy of the radiation, for such effects as radiator thickness etc. This will have the effect of lowering the estimate of the absolute quantum intensities of those γ-rays of energies less than 582 keV, and increasing the quantum intensities of the γ-rays more energetic than 582 keV. No account has, however, been taken of this effect, since no information on the thicknesses of the source and the radiators was given by Thibaud. The rough values obtained for the quantum intensities shew reasonably good agreement with the values obtained from the classification of the γ-ray transitions, summarized in Table 8.3.

§ 5. Further remarks on the suggested level scheme for RdTh.

An argument may now be developed to shew that the 2.18 MeV β-particle transition does not feed the ground state of the RdTh nucleus. The argument depends entirely on the suggestion that the γ-ray transition of 336 keV energy occurs between the levels fed by the partial spectra with end-points at energies of 1.85 and 2.18 MeV. These modes of β-decay are clearly forbidden to the same degree (vide Table 8.2), and should therefore excite states of RdTh of identical spins and parities. If one of these states is the ground state of RdTh, then both states will have zero spins and even parities (since RdTh is an even-even nucleus). In this case quantum emission for a transition between the two states will be prohibited by selection rules, and since Thibaud has detected such emission, then either the 336 keV γ-radiation is incorrectly placed in the level scheme suggested, or the 2.18 MeV β-transition feeds an excited state of RdTh of non-zero spin.

The probabilities of β-particle disintegrations feeding the four additional energy states, introduced to account for the observed γ-rays, may be calculated, using values for $\log ft$, shewn in column 5 of Table 8.6, derived from the classification of Nordheim[41]. The values for $\log f$, obtained from the data of Feenberg and Trigg[40], are shewn in

column 6. Column 8 then shews the relative intensities of these modes of β-disintegration, which, in most cases, are clearly many times too small to be detectable.

TABLE 8.6.

Maximum energy of β-disintegration. (Mev.) (1).	ϵ (mc^2) (2)	Change in spin and parity. (3).	Degree of forbiddenness. (4).	Estimated $\log_{10} ft$. (5).	$\log_{10} f$. (6).	t (secs). (7).	Intensity per 100 disintegrations. (8).
.540	2.070	2(Yes)	1st	8.5	1.3	1.6×10^{7}	0.14
.740	2.450	2(No)	2nd	13.5	1.8	5×10^{11}	0.4×10^{-5}
1.611	4.151	3(Yes)	3rd	~14	3.05	8×10^{10}	0.3×10^{-4}
2.053	5.020	3(Yes)	3rd	~14	3.5	3×10^{10}	0.7×10^{-4}
2.237	5.378	4(Yes)	3rd	~17	3.6	2.5×10^{15}	10^{-7}

The decay scheme proposed suggests the possibility of several γ-radiations not yet observed, and examination of the spectrum with an instrument of very high resolution would almost certainly reveal lines at present undetected or unresolved.

§6. The energy states of $MsTh_2$.

It has been assumed that the six component β-particle spectra of the disintegration of $MsTh_2$ de-excite directly a single energy state of that nucleus. The possibility of β-disintegration from more than one energy state of $MsTh_2$ will now be examined, and the implications discussed.

Little is known of the β-disintegration of $MsTh_1$, but there is evidence that the end-point occurs at an energy of ~18 keV[6], and that only low energy γ-radiations follow the β-transition. The levels of the $MsTh_2$ therefore appear to be closely spaced, and in consequence the excitation energies for the states of the RdTh nucleus will be little affected, even if β-decay from more than one energy state of $MsTh_2$ occurs. The suggested level scheme for RdTh will, however, require considerable revision, especially with regard to the spin values and to the parities assigned to the various energy states, if one or more modes of the observed β-decay de-excite directly a further energy state of $MsTh_2$, possessing a spin or parity different from that identified.

Let such a mode of β-decay be postulated, and, to be precise, let the decay scheme for $MsTh_2$ be illustrated by Figure 8.2, in which β-decay from an excited state accounts for (100 - p)% of the

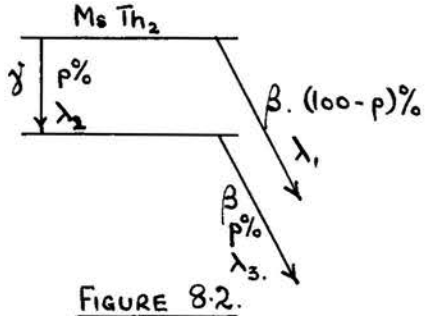

FIGURE 8·2.

disintegrations of $MsTh_2$, and the remaining p% involve a γ-ray transition before decaying by β-emission from a lower energy state. Let the decay constants for the transitions shewn in the figure be λ_1, λ_2 and λ_3

Rather lengthy but elementary analysis shews that the β-particle activity, due to the decay of $MsTh_2$, at a time t after the removal of all daughter activities from the parent $MsTh_1$ is given by A_t where

$$A_t = N\left[1 - \frac{\lambda_1^2 - \lambda_2\lambda_3}{\lambda_1^2 + \lambda_2^2 - \lambda_2\lambda_3} e^{-\frac{\lambda_1^2 + \lambda_2^2}{\lambda_1 + \lambda_2}t} - \frac{\lambda_2^2}{\lambda_1^2 + \lambda_2^2 - \lambda_2\lambda_3} e^{-\frac{\lambda_2\lambda_3}{\lambda_1 + \lambda_2}t}\right]$$

In this expression N represents the number of disintegrations of $MsTh_1$ which occur per second, which is presumed to be sensibly constant.

The growth of the number of β-disintegrations which de-excite both energy states of $MsTh_2$ gives rise to the first exponential term of this expression, whereas the second exponential term concerns the growth of activity arising from the lower energy state only.

The following three cases arise in which the presence of branching may be difficult to detect by ordinary decay methods.

(1) $\lambda_1^2 + \lambda_2^2 \gg \lambda_2 \lambda_3$

(2) $\lambda_1^2 + \lambda_2^2 \ll \lambda_2 \lambda_3$

(3) $\lambda_1^2 = \lambda_2 \lambda_3$

In the first case, the first exponential term of the expression for the activity will rapidly become small compared with the second term, whereas in the second case, the second exponential term quickly assumes negligible proportions compared with the first term. If either of these cases exist , then the initial growth of $MsTh_2$ in freshly separated $MsTh_1$ will shew departure from linearity. Lecoin, Perey and Riou[7], who commenced observations 9 minutes after the chemical isolation of $MsTh_1$, found the growth of activity due to $MsTh_2$, to proceed linearly with time. Such branching therefore appears to be unlikely, but cannot be entirely ruled out until the time spent in the chemical isolation of $MsTh_1$ is made very small.

Insofar as the decay of isolated $MsTh_2$ is concerned, which applies to all the experiments of these new observations, the activity due to β-decay from the higher energy state would have died out before observations were commenced, which was usually ~ 3 hours after the initial separation of the parent body, $MsTh_1$, if the decay constants satisfy the first case postulated.

If the decay constants conform to the second case, then the decay of activity from the lower energy state of $MsTh_2$ would be in transient equilibrium with the γ-activity, for λ_1 and λ_2 will be small compared with λ_3. If the fraction p is large, then it may be assumed that the main component of the β-activity (which accounts for ~50% of the total disintegrations) would de-excite directly this lower energy state of $MsTh_2$. The transition would possess the smallest life-time if it were of the "allowed" form, and an estimate of the half-life, based on assuming a value for $\log_{10} ft$ of 5, is ~7 minutes. Additional competitive modes of β-decay from this lower state of $MsTh_2$ would further reduce the life-time of the state for β-emission and the growth curves of Lecoin et al. may fail to shew the existence of such branching. Reduction of the value assumed for p implies that λ_2 becomes smaller, when compared with λ_1, and the term $\frac{\lambda_2 \lambda_3}{\lambda_1 + \lambda_2}$ of the exponent in the expression for the growth of activity becomes smaller. This in turn implies that the contribution of activity due to this exponential term takes longer to die out making possible branching more easily detectable by the study of the initial growth of activity.

For the third case mentioned, which seems rather improbable, it may be possible to detect departure from a half-value period of 6.13 hours in the growth

of activity in $MsTh_1$, by using absorbers of various thicknesses between the source and the detector. An experiment of this type performed by Lecoin et al.[7] has failed to shew such an effect. Moreover, it seems probable that in such a case the decay of the continuous β-particle spectrum of $MsTh_2$ may proceed at different rates according to the momentum interval selected. Checks were made at many different energies, and the decay was always found to proceed with a half-value period of 6.13 hours.

It is therefore concluded that, whilst it cannot definitely be claimed that β-γ branching in the $MsTh_2$ nucleus does not exist, there is no evidence for the existence of such a decay process to any appreciable extent.

Turning now to the β-decay of $MsTh_1$, the low value for the end-point limits the spin change which can occur in the transition. Tentatively accepting the value of 18 keV for the end-point of the β-spectrum, a $\log_{10} ft$ value of ~5 is obtained, indicating that the transition is allowed, with a spin change of unity and no parity change. Presuming then that the even-even $MsTh_1$ nucleus decays by β-emission from a state of zero spin and even parity, the state of $MsTh_2$ excited by β-decay of the parent body possesses a spin

value of 1 and even parity. Now the state of the $MsTh_2$ nucleus de-excited by β-emission has been tentatively identified as one possessing a spin of 4 and odd parity. It therefore seems probable that intense γ-activity follows the β-decay of $MsTh_1$. If a single γ-ray were involved in the transition from the 1+ state to the 4- state of $MsTh_2$, then the type of γ-radiation would be electric octupole. No energetic γ-rays have been observed to follow the β-decay of $MsTh_1$, and such a high order of multipolarity therefore implies that the single γ-transition postulated would possess a relatively long half-life. This, in turn, implies that β-decay from the 1+ state of $MsTh_2$ may be a serious competitor to such a γ-transition, which has been shewn to be unlikely. It therefore seems evident that a series of lower energy cascade γ-ray transitions occurs, each transition being of much shorter lifetime than that of electric octupole radiation.

ACKNOWLEDGEMENTS.

The writer wishes to acknowledge the valuable assistance received from many quarters during these experiments.

In particular, thanks are due to Professor N. Feather, F.R.S., for extending the facilities of his laboratory and for much stimulating discussion, and to Mr. J. Kyles, M.A., for his valuable guidance and active participation in all phases of the work. Throughout 1951, Dr. W.J. Henderson, on leave from the National Research Council of Canada, actively assisted in the early experiments with the scintillation counters, and later in the daily work of source preparation which led to the preliminary results of this investigation. This valuable assistance was greatly appreciated.

Thanks are also due to Dr. N. Miller for much helpful advice in source preparation, to Mr. W.D. Brodie, B.Sc. for communicating some of his results, at present unpublished, and to Mr. Headridge and the technical staff of the Natural Philosophy Department for valuable assistance in the construction of apparatus.

List of References.

1. Feather, 1940, Proc. Camb. Phil. Soc. II, 36, 224.

2. Feather, Kyles and Pringle, 1948, Proc. Phys. Soc., Lond. 61, 466.

3. Bothe and Maier-Leibnitz, 1937, Z. Phys., 104, 604.

4. Black, 1924, Proc. Roy. Soc. A, 106, 632.

5. Yovanovitch and d'Espine, 1927, J. Phys. Radium, 8, 276.

6. Lecoin, Perey and Teillac, 1949, J. Phys. Radium, 10, 33.

7. Lecoin, Perey and Riou, 1949, J. Phys. Radium, 10, 390.

8. Lecoin, 1935, C.R. Acad. Sci., Paris, 200, 1931.

9. Lecoin, 1938, J. Phys. Radium, 9, 81.

10. Libby and Lee, 1939, Phys. Rev., 55, 245.

11. Feather, 1930, Phys. Rev. 35, 1559.

12. Feather, 1938, Proc. Camb. Phil. Soc. I, 34, 115.

13. Curie, Radioactivité, 1935, 294, Hermann & Co., Paris.

14. Li, 1937, Proc. Camb. Phil. Soc. I, 33, 164.

15. Lawson and Tyler, 1940, Rev. Sci. Instrum., 11, 6.

16. Saha, 1945, Indian J. Phys., 19, 97.

17. Wells, 1951, J. Brit. Instn. Radio Engrs., 11, 491.

18. Ginzton, Hewlett, Jasberg and Noe, 1948. Proc. Inst. Radio Engrs. 36, 956.

19. Elliot, Liebson, Myers and Ravilious, 1950, Rev. Sci. Instrum., 21, 631.

20. Kelley and Goodrich, 1950, Phys. Rev., 77, 138.

21. Bridgman, 1925, Proc. Amer. Acad. Arts. Sci., 60, 305.

22. Leininger, 1952, Rev. Sci. Instrum., 23, 127.

23. Curling and Newton, 1950, Nature, Lond., 166, 339.

24. Cockroft, Ellis and Kershaw, 1932, Proc. Roy. Soc. A, 135, 628.

25. Ellis, 1932, Proc. Roy. Soc. A, 138, 318.

26. Martin and Richardson, 1948, Proc. Roy. Soc. A, 195, 287.

27. Haissinsky, 1933, C.R.Acad. Sci., Paris, 196, 1778,

28. McLane and Peterson, M.D.D.C. 1742.

29. Peterson, M.D.D.C. 1709.

30. Butt, 1949, Proc. Phys. Soc., B, 62, 551.

31. Butt, 1950, Proc. Phys. Soc. B, 63, 986.

32. Ellis and Skinner, 1924, Proc. Roy. Soc. A, 105, 165.

33. Ellis, 1934, Proc. Roy. Soc. A, 143, 350.

34. Campbell, Henderson and Kyles, 1952, Phil. Mag. 43, 126.

35. Feister, 1950, Phys. Rev. 78, 375.

36. Hahn and Erbacher, 1926, Phys. Z, 27, 531.

37. Konopinski and Uhlenbeck, 1941, Phys. Rev. 60, 308.

38. Feather, 1943, Proc. Camb. Phil. Soc. II, 39, 84.

39. Cauchois, 1952, J. Phys. Radium, 13, 113.

40. Feenberg and Trigg, 1950, Rev. Mod. Phys., 22, 399.

41. Nordheim, 1951, Rev. Mod. Phys., 23, 322.

42. Rose, Goertzel and Perry, 1951, ORNL 1023.

43. Thibaud, 1926, Ann. Phys., Paris, 5, 73.

44. Gellmann, Griffith and Stanley, 1952, Phys. Rev. 85, 944.

45. Dunlavey and Seaborg, 1952, Phys. Rev. 87, 165.

46. Goldhaber and Sunyar, 1951, Phys. Rev. 83, 906.

47. Spinrad and Keller, 1951, Phys. Rev., 84, 1056.

48. Austern and Sachs, 1951, Phys. Rev., 81, 710.

49. Martin and Richardson, 1950, Proc. Phys. Soc. Lond., A., 63, 223.